Metabolic-response assessment of metastatic murine breast cancer in 2D and 3D cultures using intrinsic NADH as a natural biomarker

A Thesis
SUBMITTED TO THE FACULTY OF THE
UNIVERSITY OF MINNESOTA
BY

Anh Cong

IN PARTIAL FULFILLMENT OF THE REQUIREMENTS
FOR THE DEGREE OF
MASTER OF SCIENCE

Thesis Advisor: Dr. Ahmed A. Heikal
Co-Advisor: Dr. Jon M. Holy

August 2019

Acknowledgements

I would like to begin by acknowledging the tremendous knowledge, help, and support that I have been fortunate enough to receive from both my advisor, Dr. Ahmed Heikal and my co-advisor, Dr. Jon Holy throughout my time in this program. Dr. Heikal, thank you so much for your unending kindness and patience, for they keep me encouraged and motivated especially when things are tough and stressful. Dr. Holy, thank you for your time and patience while training me on cell culture, as well as a great sense of humor that makes working on something so new so much less overwhelming. The constant enthusiasm, intellectual curiosity, and dedication from both of you have been and always will be very inspiring to me.

I would like to also express my sincere gratitude to my thesis committee members, Dr. Erin Sheets and Dr. Jacob Wainman, for their continuing support along the way. Dr. Sheets, your expertise, strength, and work ethics are truly admirable. Thank you for always dedicating your time and supporting all of us! Dr. Wainman, thank you for your generous welcome since my day one of graduate school and your helpful guidance during my time here.

My progress presented here would certainly not be possible without the mentorship and friendship of former and current graduate students, Hong Bok Lee, Rafaela Pimenta, and Robert Miller. Hong Bok and Robby, thank you and congratulations on your well-deserved achievements. To Rafaela, I appreciate so much your kind, unhesitant help and support, and I wish you the best of luck with the rest of your Doctorate program.

To everybody from the Heikal/Sheets group, thank you for always providing me with your support and constructive feedback. I wish you the best with your future academic and research advancement. I hope that you enjoy and savor your time in our group.

I am also very grateful for the generous support and funding from the Chemistry and Biochemistry Department, as well as the Swenson College of Science and Engineering. Thank you to all departmental faculty members, office staff, and building staff for your readily available help and guidance.

To all of my friends and fellow graduate students, thank you for being a part of the process, for sharing all the good and tough times. Congratulations on your achievements and I wish you the best of luck with your future endeavors!

Dedications

This thesis is dedicated to my family for their love, support, and encouragement from the other side of the world.

To my past self, for I cannot be here without your struggles.

Abstract

The majority of *in vitro* studies of living cells are routinely conducted in a two-dimensional (2D) monolayer culture towards pathophysiological investigation, drug screenings, and cancer diagnostics. There is strong evidence, however, that suggests cellular behavior and metabolism in 2D cell culture is too simplistic of a model as compared with those *in vivo* tumor cells. In this project, we hypothesize that cancer cell metabolism and metabolic responses to external stimuli (e.g. drug treatments) are distinctly different in three-dimensional (3D), tumor-like model as compared with that of the conventional 2D monolayer culture. To test this hypothesis, we employed two-photon (2P) fluorescence lifetime imaging microscopy (2P-FLIM) and time-resolved 2P-fluorescence anisotropy of the reduced nicotinamide adenine dinucleotide (NADH) in metastatic murine breast cancer cells 4T1. In addition, we investigated the cellular metabolic response of 4T1 cells in 2D monolayer and 3D collagen matrix cultures to drug treatment using two novel metabolic drugs, namely MD1 and TPPBr. Both 2P-FLIM and complementary time-resolved anisotropy approaches reveal significant differences between metabolic activities of 4T1 cells in 2D and 3D cultures. Our results suggest that these 4T1 cells in 3D culture adapt an oxidative shift but glycolysis dominances the metabolic state of 2D cells. In addition, 4T1 cells in 3D culture appear to adapt more quickly and exhibit enhanced metabolic activities in response to drug treatment. In contrast, 4T1 cells in 2D monolayer culture exhibit a mute response and are less sensitive to drug treatments. While the tumor-like 3D collagen matrix model may not be an exact replica of *in vivo* tumors, these studies represent a critical step towards the development of a fundamental understanding of cellular behaviors and metabolism in the more complex in vivo models. These studies would also help advance our understanding of how the cancer cell heterogeneity and microenvironmental conditions impact metabolism and metabolic plasticity in tumor growth and metastatic progression.

Table of Contents

List of Tables

List of Figures

List of Abbreviations

MCTs	Monocarboxylate transporters
TCA	Tricarboxylic acid cycle
2D	Two-dimensional
3D	Three-dimensional
ECM	Extracellular matrix
ATP	Adenosine triphosphate
LDH	Lactate dehydrogenase
mMDH	Mitochondrial malatedehydrogenase
NADH	Reduced nicotinamide dinucleotide
NAD^+	Oxidized nicotinamide dinucleotide
NADPH	Reduced nicotinamide adenine dinucleotide phosphate
FMN	Flavin mononucleotide
ETC	Electron transport chain
OXPHOS	Oxidative phosphorylation
ATCC	American Type Culture Collection
DMEM	Dulbecco's modified Eagle's medium
EDTA	Ethylenediaminetetraacetic acid
PBS	Phosphate-buffered saline
HBSS	Hank's balanced salt solution
2P-FLIM	Two-photon fluorescence lifetime imaging microscopy
2P-Anisotropy	Two-photon time-resolved fluorescence anisotropy
UV	Ultraviolet
IR	Infrared
MCP	Microchannel plate
NA	Numerical aperture
G-Factor	Geometric factor

List of Symbols

α_i	Amplitude fraction of the i^{th} species
τ_i	Fluorescence lifetime of the i^{th} species
$<\tau>$	Average fluorescence lifetime of all species
χ^2	Chi-squared
q_i	Fluorescence signal contributed by the i^{th} species
β_i	Initial anisotropy of the i^{th} species
ϕ_i	Rotational time of the i^{th} species
r_0	Total initial anisotropy
$I_\perp$	Perpendicular intensity
$I_\parallel$	Parallel intensity
G	G-factor
r(t)	Time-resolved anisotropy
F	Fraction of free NADH
B	Fraction of enzyme-bound NADH
K_{eq}	Equilibrium constant
ΔG'	Change in Gibbs free energy
t/T	Time
R	Gas constant

Chapter I: Introduction

1.1 An overview on breast cancer

Over the past two decades, breast cancer is still the most commonly diagnosed cancer, and the second contributor to cancer deaths in women (1, 2). Due to the complexity and highly dynamic nature of cancer cells, however, many things remain unknown about cellular behaviors and interactions within a tumor. The level of heterogeneity of tumor cells in particular makes it challenging to study them as a whole (3-5). Cancer cells are also constantly changing, where their behaviors and characteristics are easily influenced by factors in their varying microenvironments, which further complicates the problem (6-9). This shows a need for more extensive studies to increase our understanding of tumor behaviors, especially in relation to local environmental factors. From this knowledge, further work can be done to improve current researches, diagnoses, treatments, and potentially produce more effective therapies to treat breast cancer.

1.2 Cancer metabolism

Cancer cells are known to be dynamic and heterogeneous species, with a high level of adaptation that aids their survival and growth within the body. One of the most important characteristics is metabolic plasticity, which significantly increases their ability to adapt (6, 8, 9). By shifting their main cellular metabolic pathways towards either a glycolytic or oxidative direction, cancer cells can efficiently generate biomolecules possessing high energy potential that can help them proliferate and potentially metastasize. First studied by Warburg group nearly a century ago, cells within a tumor tend to express a strong glycolytic shift, signaled by a large increase in glucose uptake and lactate production (10). This trait is due to a period of hypoxia during their initial rapid growth. Unable to perform oxidative processes due to the low oxygen level in their local environments and mitochondrial-malfunctioning, the tumor cells have to rely strictly on glycolysis as the preferred energy metabolic pathway. This characteristic, however, remains even when the oxygen

concentration rises back up later on. The phenomenon is generally referred to as the *Warburg effect*, or simply aerobic glycolysis.

Recently, it has been reported that aerobic glycolysis might not be an exclusive trait to cancer cells. Human skin keloid fibroblasts, during and even long after wound healing, appear to also express this glycolytic shift according to a study by Vincent et al. (11). Induced pluripotent stem cells can selectively use glycolysis and fatty acid metabolism to generate usable energy in the form of ATP during their early steps in cellular reprogramming (12). In a co-culture set-up, a quite contrasting trend to the known *Warburg effect* was observed (13), where a symbiotic relationship between cancer cells and associated fibroblasts was suggested, and the fibroblasts rely heavily on aerobic glycolysis. The byproducts of this pathway – lactate and pyruvate, are transferred out of fibroblast cells by monocarboxylate transporters (MCTs) (14, 15). They are then imported into neighboring cancer cells, which use these readily made molecules to drive their mitochondrial tricarboxylic acid cycle (TCA) and promote oxidative phosphorylation, generating a large number of ATPs. Due to the opposite behaviors of cancer cells in this scenario, it is thus named the *reverse Warburg effect*.

Energy metabolism is a critical factor in the growth and survival of living cells, and therefore, makes an ideal target for cancer therapies. With the growing knowledge of cancer cell metabolism, more therapeutic agents that target these major metabolic pathways or unique metabolic dysfunctions in cancer cells are being produced. The focus of this project which will be discussed below in further details, is cellular metabolism in relevance to the *Warburg* and *reverse Warburg effect* – glycolysis and mitochondrial oxidative phosphorylation.

1.3 Microenvironmental influence on cancer metabolism

An important goal in cancer therapy is to identify key differences between cancer and non-cancer cells that can be targeted. Cancer cell metabolism thus has gained great interest as a potential cancer therapeutic target. The topic is still quite complex, due to a number of characteristics that make it difficult to study tumor as a whole. These include the intra- and

inter-tumor cell heterogeneity, tumor cell-tumor cell and tumor cell-stromal/immune cell interactions, as well as tumor cell-extracellular matrix interactions. Both intra-tumor cell heterogeneity (variation within a tumor) and inter-tumor cell heterogeneity (variation from patient-to-patient) are characteristics that have been well established and studied on (3, 5, 9, 16-18). While the *Warburg effect* identifies a unique and potentially targetable trait in cancer cell metabolism, the *reverse Warburg effect* yet demonstrates that the picture is not as simple due to interactions between cancer cells and their neighboring stromal fibroblasts. Tumor microenvironmental impacts on cancer cells have also been shown to play a significant role in cellular reprogramming and tumor progression (19-22). Within their surrounding environment, cells are provided with both mechanical and biochemical signaling that can promote specific growth direction, such as towards an invasive phenotype (19, 23). In addition, the extracellular matrix is structurally diverse and actively adapting to local cellular behaviors (19). With such physiological relevance, the interplay between the extracellular matrix and tumor cellular metabolism unfortunately has not been explored in depth. The attention has been shifted more towards extensive studies that aim to improve our understanding of this relationship to expand and hopefully complete the overall picture of tumor physiology.

With such a high level of adaptation, it is not surprising that cancer cell behaviors can vary significantly depending on the characteristics of their surrounding environment. This is especially important in tumor models or cancer drugs testing *in vitro*, where an *in vivo* like environment and accurate cellular responses are desired. As a result of our growing knowledge in the importance of culture environment, instead of the conventional two-dimensional (2D) monolayer, studies using different types of three-dimensional (3D) collagen matrix as a tumor model have been proposed and implemented. This approach bases on the fact that solid tumors *in vivo* grow in 3D clusters that are embedded within their extracellular matrix (ECM) instead of a flat monolayer. Collagen (type I) is the most abundant ECM protein in the stroma, especially relevant in the context of breast cancer, thus is the ideal building block for biomimetic breast tumor models (24). Some of the collagen 3D model systems include multicellular tumor spheroids (25, 26), collagen droplets (27), and density varying collagen gels (20, 28, 29). Interactions between series of different tumor cell lines as well as tumor differentiation due to the influence of a three-

dimensional (3D) collagen matrix have been studied (30, 31). Furthermore, collagen matrix is found to be able to impact cancer migration (20), cellular remodeling in tumor angiogenesis (21), fibroblastic behaviors (28), as well as genetic expression, metabolites, and cytokines released from cells as compared to the traditional 2D model (24). To explore environmental impact on cancer cell metabolism, we are interested in studying the differences in metabolic activities in live breast cancer cells when cultured in a 3D collagen matrix compared to the conventional 2D monolayer.

1.4 NADH is an important coenzyme to cellular energy metabolism

The main energy metabolic pathways in living cells include a mix of glycolysis and oxidative phosphorylation (Figure 1.1). Glycolysis is a cytosolic 10 step process that breaks down a molecule of glucose into two molecules of pyruvate. As a result, a net of two adenosine triphosphate (ATP) molecules – the cellular energy currency, are produced. These molecules containing high energy phosphate can be transferred out to be used by other metabolic processes that require an energy input. Under anaerobic condition, pyruvates are then further broken down and converted into lactate by lactate dehydrogenase (LDH) (32, 33). The accumulation of lactate is most often associated to muscle cells during intense exercise that are subjected to hypoxia. Lactate has also been reported as a marker for aerobic glycolysis in cancer cells and to predict malignant tumor progression (10, 34, 35). An important coenzyme in glycolysis is the reduced cofactor nicotinamide adenine dinucleotide (NADH). This coenzyme and its oxidized counterpart (NAD^+) act as high energy electron carriers that directly participate in the cellular redox cycles by helping with a number of important metabolic processes. To fulfill this role, the free population of NADH that is generated from glycolysis is transported to other cellular pathways where it is needed, such as lactate fermentation and mitochondrial oxidative oxidation (32, 33).

For cells that are exposed to a normal level of oxygen, glycolysis is not the preferred metabolic direction due to the lower number of ATPs it generates (only 2 molecules). Instead, the main energy generating pathways are in the mitochondria – the powerhouse of the cell. Pyruvate from glycolysis once imported into the mitochondria, is converted into acetyl CoA and used to generate intermediates for further biomolecular syntheses (some

include six molecules of NADH) via the citric acid (TCA) cycle (32). Meanwhile, free NADH from the cytosol is also transported into the mitochondria by the malate-aspartate shuttle and combined with the newly produced NADH pool from the TCA cycle. Here, they bind and donate electrons to flavin mononucleotide (FMN) of complex I in the electron transport chain (ETC). This electron transfer process couples with a proton pump that transports proton across the inner mitochondrial membrane. The proton gradient that is built up by the ETC enzyme complexes together form a membrane potential, which drives ATP synthesis by ATP synthase. This process overall is referred to as oxidative phosphorylation (OXPHOS), which makes about 19 times more ATP than glycolysis (33).

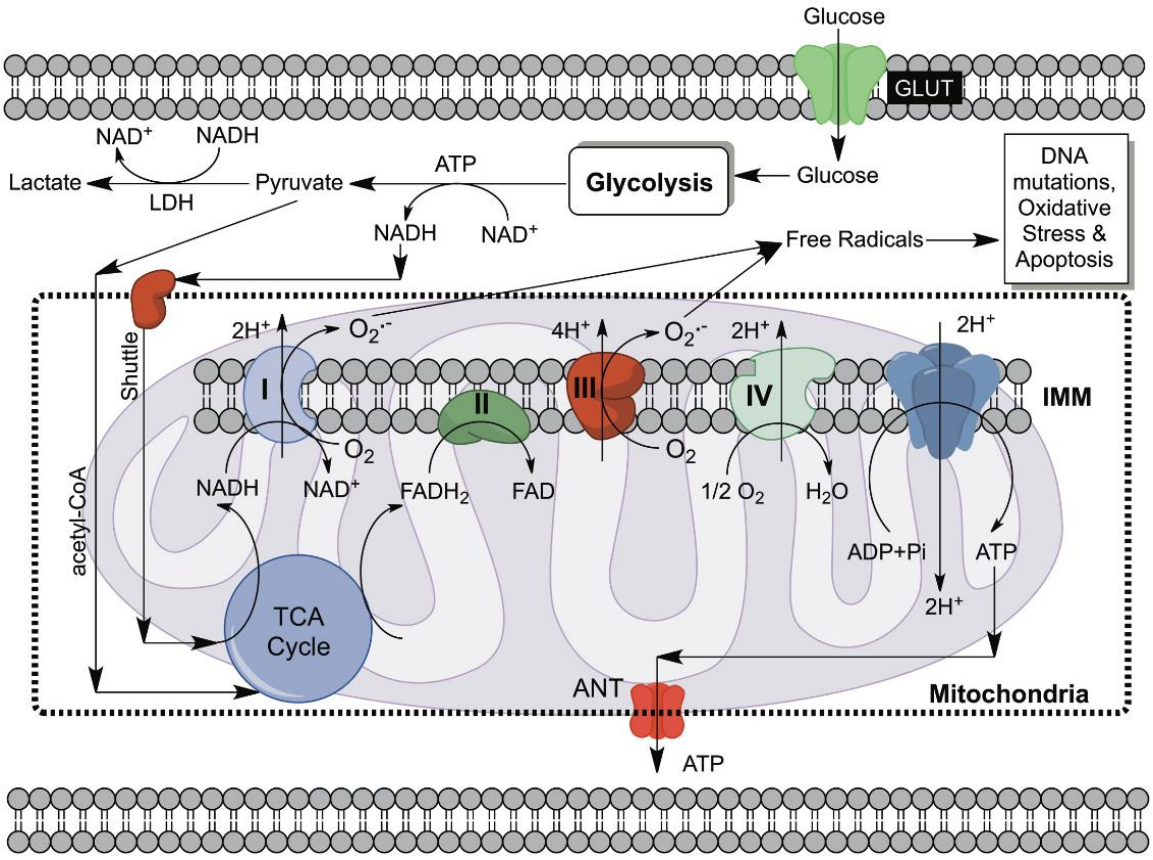

Figure 1.1: Diagram of the main cellular metabolic pathways and the central role of NADH within these pathways.

Due to the significantly higher ATP generating efficiency, it makes sense that ATP synthesis through oxidative pathways is generally preferred. However, it is interesting to note that some cancer cells, according to the *Warburg effect*, can thrive on a pathway that is seemingly less efficient like aerobic glycolysis. The reasons behind this are contributed to the fact that glycolysis rate is extremely fast in comparison to OXPHOS and is even more accelerated in cancer cells (32). They also adapt with an efficient lactate transport mechanism that helps keep up with the accumulated lactate population (15). In additional, by not going through mitochondrial OXPHOS, these cells can advantageously avoid the generation of harmful reactive oxygen species (ROS) through oxidative pathways, which is known to initiate cellular apoptosis (32, 33, 36). Nevertheless, to accurately assess cellular metabolic activities, it is important to be able to monitor the redox balance that is directly related to these pathways. This emphasizes the beneficial role of redox coenzymes like NADH and NAD^+ in diagnosing cellular physiological state (33, 37).

1.5 NADH as a biomarker to monitor cellular metabolic activities

The pioneering work of Britton Chance and colleagues (38-41) successfully laid a foundation and initiated a surge in interest for the use of intracellular biomarkers to study cellular metabolism and physiology. The central involvement of NADH and its oxidized counterpart in cellular metabolic pathways, together with its fluorescent properties make it an ideal intrinsic biomarker to monitor cellular redox state (33, 37). NADH molecule is made up from two nucleotides that are connected by a flexible pyrophosphate linker (Figure 1.5). The fluorescence properties of the molecule is attributed to the reduced nicotinamide ring (33, 42). When oxidized, however, this structure is no longer fluorescent, giving us the ability to detect only signal from NADH. Maximum absorbance of NADH occurs at around 340 nm wavelength, and its fluorescence emission peaks near 460 nm, with signals mostly localized in the cellular mitochondria (33, 36, 37, 41). Other fluorescence properties and spectrum cross section of this intracellular fluorophore have been characterized extensively over the years (37, 43-46). To avoid photochemical induced damages made to biological system along with significant scattering, the use of multiphoton excitation is often applied to intracellular NADH studies (33, 36). While using a longer excitation wavelength (700-730 nm), NADH still exhibits similar emission

spectrum when excited with two-photon compared with single photon (33). The advantages of two-photon excitation as well as pulsed laser will be further elaborated in chapter 3 of this thesis.

Fluorescent characteristics of NADH also differ between free and enzyme-bound form. In its free form, the bridge connecting the two nucleotides is flexible, leading to two possible folded and open conformations (42). These two conformations likely result in the biexponential decay of free NADH that is often observed (44). The folded form of the coenzyme also induces quenching effect between the nicotinamide and adenine moieties (42). Interestingly, NADH exhibits extreme differences in its fluorescence lifetime when bound to an enzyme due to the stretched conformation. With binding introduced from both solution and cellular studies, both the quantum yield and fluorescence lifetime of NADH increase by about 4 times (42, 44, 45). This property is helpful in differentiating between the two free and enzyme-bound populations, which can be exploited to monitor changes in cellular metabolic states (33).

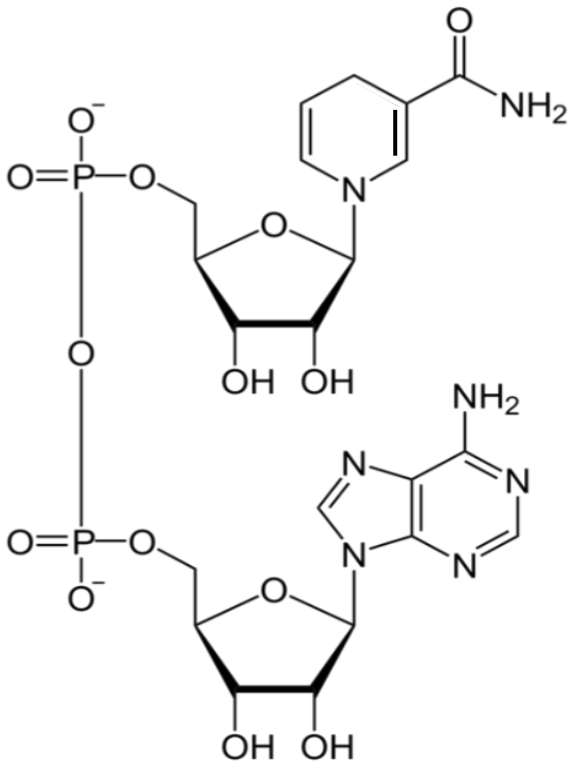

Figure 1.2: The structure of reduced nicotinamide dinucleotide (NADH).

In addition to NADH, reduced nicotinamide adenine dinucleotide phosphate (NADPH) is also a cofactor present within the cells, though not directly involved in energy metabolism through glycolysis and OXPHOS. Because its absorption and emission spectra are quite similar to that of NADH, it is difficult to distinguish one from another (44, 46). However, due to the fact that the intracellular NADH concentration is significantly greater than that of NADPH (by approximately 10 times), the major contribution to the intracellular signal is still from NADH (33, 36, 44). As a result, NADH and NADPH signals obtained from cells is generally referred to as NAD(P)H or simply NADH. From here on out, NADH will be used to indicate both species in this study.

1.6 Hypothesis and significance of research

1.6.1 Hypothesis 1: Metabolism of metastatic breast cancer in different culture types

As observed from routine culture of 4T1, cells grown in two-dimensional (2D) monolayer and three-dimensional (3D) collagen matrix consistently exhibit some interesting behaviors during their growth. On a stiff plastic surface, cells from 2D culture of 4T1 are not motile, with physical appearance resembling that of epithelial cells. Meanwhile, cells from 3D culture of 4T1 appear to possess a higher level of motility, as well as invasive characteristics. Because motility and invasion demand a higher energy input, we hypothesize that 4T1 cells from 3D culture will display a metabolic state with higher energy metabolic activities compared to that of 2D culture, where a higher portion of NADH population is enzyme bound as metabolic pathways are elevated. An enhanced association with the electron transport chain (ETC) and other molecular complexes is expected to also contribute in a higher average NADH fluorescence lifetime in 3D culture of 4T1 compared to that of 2D counterpart. Metabolic activities and differences between the two culture types can be observed and quantitatively compared from measurements of intracellular NADH fluorescence in live cells.

1.6.2 Hypothesis 2: Metabolic response to anticancer treatments

We hypothesize that not only metabolic activities, but cellular responses to treatment of anticancer drugs will be influenced by cell culture environments. As cells in 3D culture are more dynamic and energetic, we expect drug effects would be more dramatic in 3D culture compared to that of 2D monolayer. Because the 3D collagen matrix aims to be similar to an *in vivo* tumor, we also expect metastatic breast cancer cells grown in collagen to express metabolic responses that are in closer alignment with the working mechanisms of these drugs. Monolayer of 4T1 with different metabolic activities also has significantly less cell-cell interactions, which may potentially delay cellular responses to drug treatments, or influence these responses to be different from drug targets. Differences between drug responses from live cells grown in 2D and 3D tumor models are reflected in their metabolic activities and can be monitored using intrinsic NADH auto-fluorescence.

1.6.3 Significance of research

The findings attained from this research will further contribute to the knowledge that we have about cancer metabolism in relation to cellular micro-environment. This study uses different fluorescence techniques and intrinsic NADH fluorescence properties to quantitatively study cellular metabolic states in real time in a non-invasive manner. Using our imaging technique, not only cellular heterogeneity can be observed, but local changes in cellular behaviors or extracellular matrix can be investigated.

The outcome of this project will hopefully add to our knowledge regarding micro-environmental influences on cellular metabolism. Our results can also contribute evidence for the advantages in using 3D models and promote efforts for more effective drug screenings within the *in vitro* platforms.

1.7 Outline of project

Based on the knowledge of cellular behaviors in tumors that can be influenced by local environments, 3D collagen matrix has been implemented as a biomimetic model of tumor instead of the conventional 2D monolayer. To investigate in details how metabolic activities are impacted by these microenvironments, a combination of two-photon lifetime imaging (2P-FLIM) and time-resolved anisotropy of NADH will be used to assess the real time metabolic state of metastatic cancer cells in 2D and 3D, with and without the effect of metabolic drugs. The connections between environmental properties and cellular metabolic activities of metastatic cancer will be further explored towards in-depth understanding of cellular metabolism in tumor-like environments.

Chapter II: Cell culture and instrumentation

2.1 Cell culture and treatments

2.1.1 Cell culture protocol

Metastatic murine breast cancer cell line (4T1) was obtained from the American Type Culture Collection (ATCC). Culture medium was made from Dulbecco's Modified Eagle's Medium (DMEM) with added 4.5 g/L glucose, sodium pyruvate, and 6 mM GlutaMAX that was supplemented with 8% Fetal Clone III and 4% newborn calf serum. Cells were cultured in Corning plastic culture dishes (35 mm x 10 mm) and incubated in a 37°C environment with 5% CO_2. Once the desired confluency was reached (70-80%), cells were passaged into new culture dishes or Mat-Tek glass bottom petri dishes (35 mm x 10 mm) for imaging. Old DMEM media was removed from these dishes and 0.75 mL of Trynsin-EDTA solution was added for 5-7 minutes while incubated at 37°C and 5% CO_2. Cells were checked before and after being trypsinized using an inverted Olympus microscope to confirm complete detachment. Culture media was added (1 mL) to trypsinized cells and the mixture was transferred to a centrifuge tube to spin down at 1250 rpm for 3 minutes. Trypsin containing media was carefully removed from the tube without disturbance to the cell pellet, and a fresh 1 mL of culture media was used to resuspend the cells. Dilution of cell suspension to a 1:10 ratio was done with a Trypan Blue solution and 10 μL of the diluted suspension was transferred to a hemocytometer for cell counting. Based on the cell count, volumes of cell suspension were calculated for seeding concentrations of either 20,000 or 100,000 cells/mL for 2D and 3D cultures, respectively.

For two-dimensional (2D) culture, the volume of cell suspension was added directly into 2mL of fresh culture media in a glass bottom plate and mixed by swirling prior to incubation. For three-dimensional (3D) culture, a mixture of 10x PBS with 10 times volume of ice-cold rat tail type I collagen (Corning), and enough NaOH 1 M to reach pH 7.4 was prepared and mixed with cell suspension. The collagen mixture was quickly transferred into the well of a glass bottom plate and incubated for 20-30 minutes to induce collagen polymerization. About 10 minutes into incubation, the plate was flipped upside

down for the remaining time to guarantee even distribution of cells within the collagen matrix. Once the collagen layer was ready, 2 mL of fresh culture media was gently added on top and the dish was placed in the incubator at 37°C with 5% CO_2. Prior to 2P-FLIM and anisotropy experiments, DMEM media in each dish was replaced by 2mL of 1x HBSS with added 2% FBS.

2.1.2 Anticancer drug treatments

Two metabolic drugs used in this study were a generous gift from Dr. V. Mereddy (the Department of Chemistry and Biochemistry of the University of Minnesota Duluth). One drug, named MD1, was made from cyano-4-hydroxycinnamic acid (47). Its action mechanism involves inhibition of MCT1 and MCT4 of the lactate transport pathway to prevent lactate transportation between cancer cells (Fig 2.1a). The second drug is a triphenyl-phosphonium bromide derivative that is still in the process of patening, thus is referred to here as TPPBr (Fig 2.1b). This compound targets the inner mitochondrial membrane and damages the oxidative pathways here (48, 49).

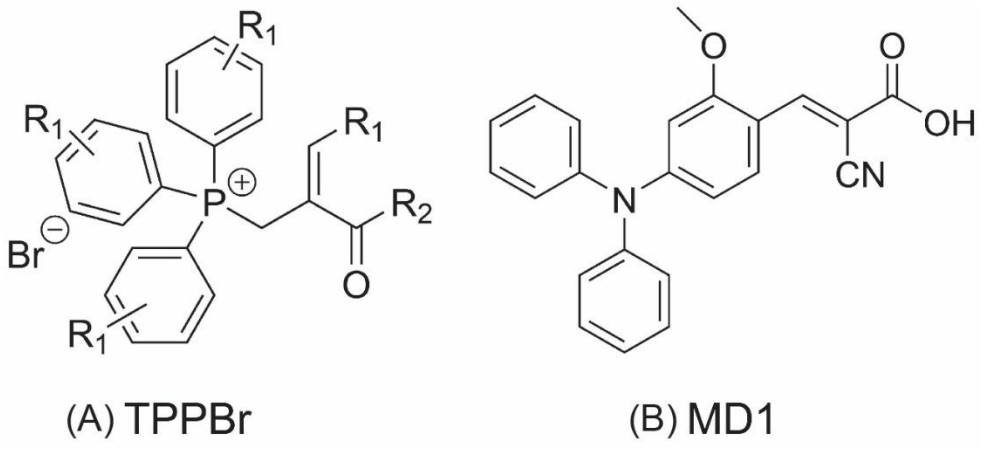

Figure 2.1: Chemical structures of (A) the OXPHOS inhibitor TPPBr and (B) MCT1 and MCT4 disruptor MD1.

Original stock concentrations provided for MD1 was 100 mM and 24 mM for TPPBr. Each drug was diluted with fresh DMEM culture media and further diluted into 2 mL of culture media in each dish. The target incubating concentration of MD1 and TPPBr in these dishes were 50 μM and 1.2 μM, respectively. Drug treatments were added approximately after 48 hours of initial incubation, and about 20 hours before experiments.

2.2 Instrumentation and analysis

2.2.1 Two-photon excitation of NADH

Traditionally, single-photon (1P) excitation of intracellular NADH requires the use of a 340 nm wavelength. However, high energy UV excitation is known to induce unwanted photo-bleaching, DNA damages to live cells, enhanced light scattering, and therefore reduced penetration depth in samples (33, 36, 42). In contrast, two-photon (2P) excitation

has been widely implemented in order to avoid these challenges while enhancing spatial resolution (36, 50). With this method, two photons with lower energy (longer wavelength ~700-730 nm) are absorbed simultaneously to bring the fluorophore to its first excited electronic state. Since this is a nonlinear process, the wavelength used for 2P excitation is around 730 nm, an infrared wavelength (42). Conveniently, the excited state fluorescence profile of NADH remains the same at 450 nm, which indicates the same excited electronic state (Fig. 2.2). In addition, the use of 2P excitation also provides an enhancement in penetration depth as well as improved spatial resolution, making it ideal for studies of biological cells or tissues (36, 42, 50).

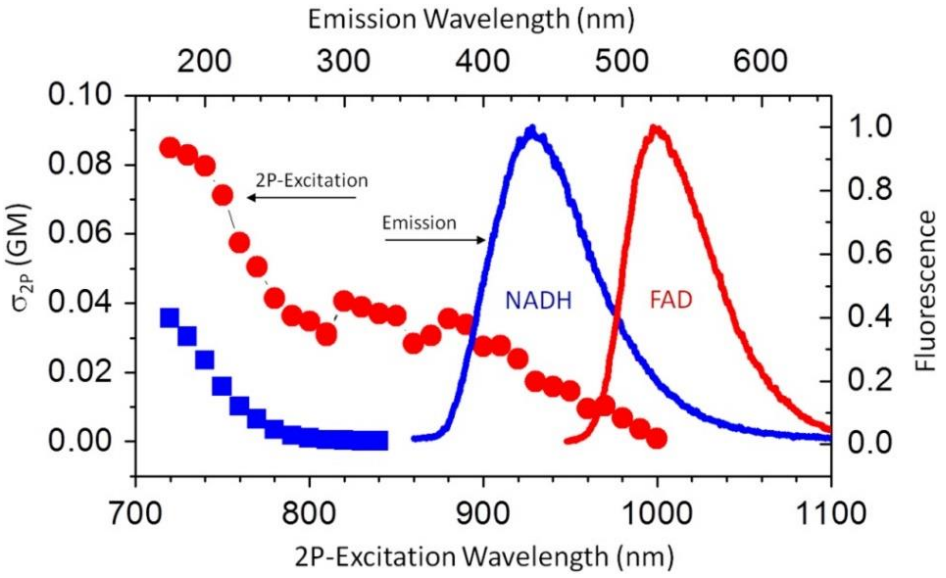

Figure 2.2: Two-photon excitation and emission of intracellular fluorophores NADH and FAD (46). The 2P-excitation for NADH is shown here as blue square symbols, and the resulting emission curve is also shown in blue. The red circle symbols and red curve describe the 2P-exciation and emission of FAD, respectively.

2.2.2 Two-photon (2P) fluorescence lifetime imaging microscopy (FLIM)

Conventional microscopy such as laser-scanning confocal microscopy is widely popular in the biological studies, where the fluorescence intensity per pixel is recorded. Fluorescence lifetime imaging microscopy (FLIM) is a more advanced technique, where fluorescence lifetime of fluorophores is recorded per pixel in addition to the 2P-fluorescence intensity. Its key advantage stems from the sensitivity of fluorescence lifetime of the fluorophore to its structural changes (ex. binding), environmental factors, and not to its concentration as in fluorescence intensity-based microscopy (33, 42). Using two-photon excitation in combination with FLIM, intracellular NADH can be quantified noninvasively, and the populations of free and enzyme bound fluorophore can be determined. Moreover, these measurements have high spatial resolution, giving us the ability to further associate NADH interactions to metabolic pathways at specific cellular compartments (33). Due to these advantages, 2P-FLIM of intrinsic NADH has been widely used to study metabolic pathways in different biological tissues both *in vitro* and *in vivo* (33, 36, 50).

The experimental set up of our laser system has been previously described elsewhere (45, 51-55). Briefly, a titanium sapphire laser system (Mira 900-F, Coherent) was pumped by a diode laser (Verdi-10 W, Coherent) to generate femto-second laser pulses at 730 nm (120 fs, 76 MHz). The generated laser pulses were directed toward a laser-scanning unit (FV300, Olympus) then to an inverted microscope (IX 81, Olympus) for FLIM measurements. The laser was steered through a 1.2 NA, 60x microscope objective (Olympus) with water immersion before exciting 2D or 3D cell cultures inside a Mat-Tek glass bottom dish sitting on top of the objective. Emission signal from the sample was filtered through a dichroic mirror then a set of two filters (HQ450/100M-2P and 690SP UV-3P, Chroma) for maximum NADH signal before being detected by a microchannel plate photomultiplier tube or MCP-PMT (R3809U, Hamamatsu). The out coming signal was amplified, routed, and collected by a SPC-830 module (Becker & Hickl). The fluorescence decay of NADH in each pixel was fitted with a biexponential decay using the SPCImage software (Becker & Hickl), and the resulting data was used to generate both fluorescence intensity and 2P-FLIM images with 256 x 256 pixels dimensions (256 time bins/pixel).

2.2.3 Analysis of 2P-FLIM measurements

2P-FLIM images were analyzed using the SPCImage software for NADH fluorescence decay. The background threshold as well as binning number were carefully selected for each image to ensure good signal-to-noise ratio and therefore reliable fluorescence lifetime analysis. The variation in threshold and binning number between different images was also kept at a minimal to maintain consistency among measurements of 2D and 3D cultures, before and after treatments. The fluorescence decay of NADH at each pixel was fitted using a biexponential decay fitting model described as follow (33, 42, 45):

$$F(t) = \alpha_1 e^{-t/\tau_1} + \alpha_2 e^{-t/\tau_2} \quad (1)$$

This biexponential decay represents a mixture of two distinct populations of NADH present within cells with distinct fluorescence lifetimes, which are attributed to free and enzyme-bound NADH. Here, the population fractions of these two species are represented by α_1 and α_2, for free and enzyme bound NADH, respectively, while the fluorescence lifetime for each species are reported as τ_1 (free NADH) and τ_2 (enzyme-bound NADH). These assignments of NADH species using their fluorescence lifetimes have been thoroughly characterized and applied in both solution and live cell studies (33, 44, 56, 57). 2P-FLIM images were first analyzed for the average lifetime of NADH (or $<\tau_f>$), which was calculated using the following equation (33, 42):

$$<\tau_f>=\frac{\alpha_1\tau_1+\alpha_2\tau_2}{\alpha_1+\alpha_2} \quad (2)$$

Due to the presence of only two main populations of NADH within the sample, the total of their population fractions ($\alpha_1 + \alpha_2$) sums up to 1. From the analyzed image, localized populations of free or enzyme bound NADH within cellular compartments were monitored and recorded. The average fluorescence lifetimes from every pixel were combined to generate a frequency-average lifetime histogram distribution for the image. In a similar manner, each image was analyzed for the remaining fitting parameters and their corresponding frequency histograms were also reported. Since each species contribute differently to the overall NADH fluorescence signal due to changes in their fluorescence quantum yield and population fractions, the signal fraction that was emitted by each NADH population was also calculated from the fitting parameters using the following equation:

$$q_i=\frac{\alpha_i\tau_i}{\alpha_1\tau_1+\alpha_2\tau_2} \quad (3)$$

where *i* stands for the individual species (1 for free NADH or 2 for enzyme bound NADH). With each image, a χ^2 value was obtained (0.9-1.1) to ensure a consistent goodness of the fit.

For each parameter that was extracted from a 2P-FLIM image, an average value and standard deviation were calculated using the ANOVA function of OriginPro 8.0. Comparisons of each parameter between 2D and 3D cultures, along with before and after drug treatments were also done using Student's *t*-tests provided in OriginPro 8.0. The details regarding these analyses are further described in Appendix I.

2.2.4 Two-photon time-resolved fluorescence anisotropy

Despite its many advantages, 2P-FLIM also has a few inherent shortcomings. As discussed in previous chapter, free NADH in solution exhibits two possible conformations (folded and stretched) that leads to a biexponential decay with two different lifetimes, one fast (~0.35 ns) and one slightly slower (~0.76 ns) (44). Even though binding is known to increase the average fluorescence lifetime of free NADH up to four folds, this enhancement is dependent on both the enzyme type and surrounding environment. Therefore, it is possible for the lifetime of bound components to overlap with the free form of this coenzyme, causing confusion regarding data interpretation. In addition, NADH auto-fluorescence is also known to be impacted by various factors in the local environment such as pH, viscosity, and crowding (33). Due to these reasons, it is necessary to seek for an alternative approach that can provide higher temporal resolution and sensitivity to changes in the hydrodynamic volume due to binding or association reactions.

Fluorescence anisotropy (Fig 2.3) is a powerful technique that is often used to study rotational dynamics of biomolecules. Rotational diffusion is sensitive to conformational changes and association reactions that cause changes in the molecular hydrodynamic volume. In time-resolved anisotropy measurements, the molecules are excited by polarized laser pulses at time zero. However, the fluorescence emission becomes depolarized soon after due to the rotational mobility that these molecules undergo (Fig 2.4). Fluorescence polarization from parallel ($I_{\parallel}(t)$) and perpendicular ($I_{\perp}(t)$) directions are detected simultaneously and used to calculate the corresponding time-resolved anisotropy.

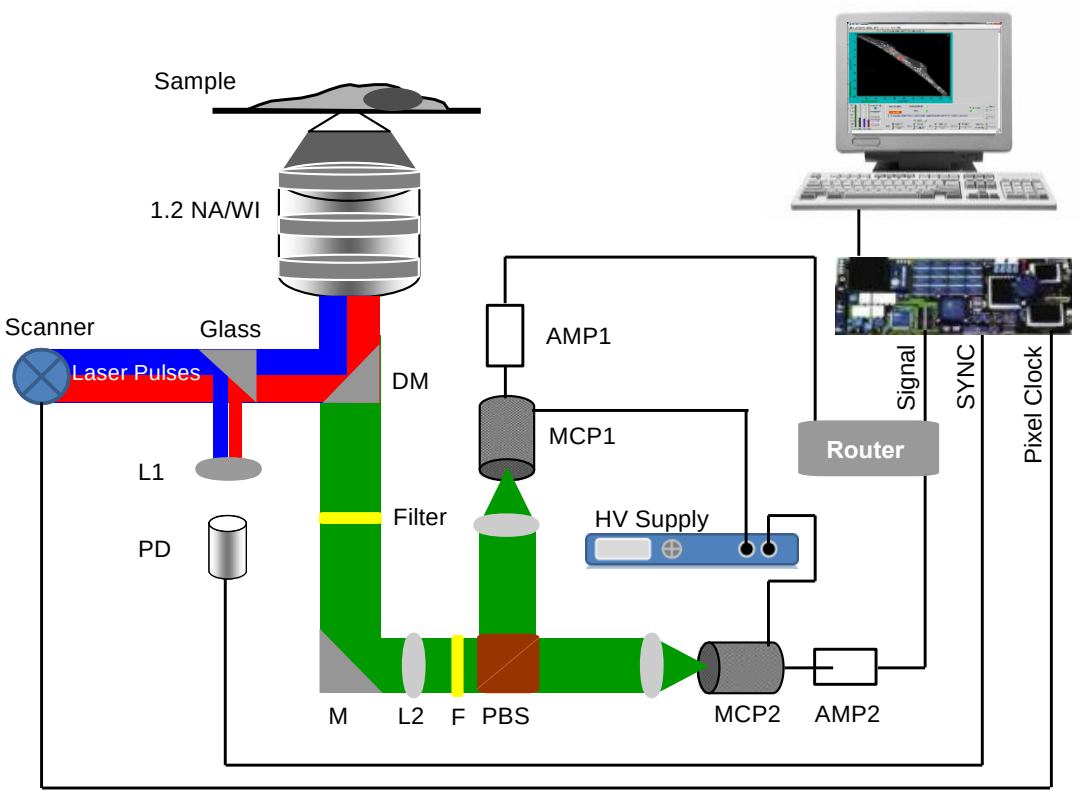

Figure 2.3: Sketch of the anisotropy laser system set up. From left to right, L1 represents lens number 1, and PD represents the photodiode that detects signal and triggers the sync cable to start data collection. Underneath the 1.2 NA objective, the dichroic mirror is described as DM, and the mirror (M) is used to steer signal towards lens number 2 (L2), then a filter (F). The polarizing beam splitter (PBS) split the signal to perpendicular and parallel channels, where they are collected by the microchannel plates (MCP1 & MCP2) and amplified (AMP1 & AMP2) before routed to the module.

This technique is applied to study molecular size, environmental viscosity, as well as crowding (42, 45, 52, 54). Free NADH (0.66 kDa) is considerably smaller compared to its enzyme-bound form (35 kDa for lactate dehydrogenase and 70 kDa for malate dehydrogenase) (44). With these substantial differences in the hydrodynamic volume, the rotational diffusion of bound NADH is significantly slower than that of free coenzyme (by 10-100 times) (33). Compared to the four-fold increase in the fluorescence lifetime, anisotropy is much more sensitive to binding reactions of fluorophores, thus is a better technique to differentiate between free and bound NADH as a biomarker of changes in cellular metabolism. However, it is worth noting that even though the temporal resolution

is greatly improved with anisotropy, the high spatial resolution as provided by 2P-FLIM is lost, since the anisotropy signal is averaged across the field of view (many cells). Therefore, this project utilizes a combination of 2P-FLIM and anisotropy measurements to best characterize the metabolic activities that are happening within cells.

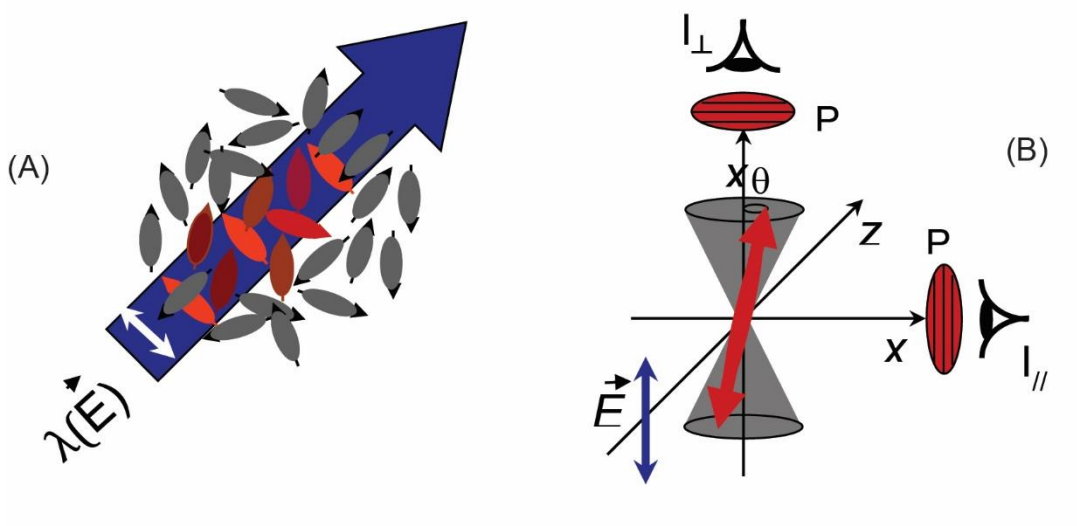

Figure 2.4: (A) Visual demonstration for selective excitation of randomly oriented fluorophores. (B) Rotation of excited fluorophore leads to depolarization, and intensity signals from which are divided into perpendicular ($I_{\perp}$) and parallel ($I_{\parallel}$) by a polarizing beam splitter.

The same laser system that was used to acquire 2P-FLIM measurements was also used for (2P) time-resolved fluorescence anisotropy, with a few minor modifications (Fig 2.3). For example, the repetition rate used in time-resolved anisotropy is reduced from 76 MHz (FLIM) to 4.22 MHz using a pulse picker (Coherent) in order to minimize photodamage while ensuring the same critical conditions for each excitation-detection cycle due to the longer rotational time. In addition, the 2P-epifluorescence of NADH is polarization analyzed to parallel and perpendicular polarization using a polarizing beam splitter prior to detection using two MCPs. The time-resolved fluorescence intensities from both channels (parallel and perpendicular) are extracted using the SPCImage software (Becker & Hickl), then combined and analyzed using the OriginPro 8.0 software (OriginLab) for time-resolved anisotropy.

2.2.5 Analysis of time-resolved fluorescence anisotropy

The time-resolved polarized fluorescence intensities of NADH were collected using parallel and perpendicular polarization. A small molecule with known rotational time (Coumarin) is routinely used as a control to calibrate the system for each day of experiment and to determine the geometrical parameter (or G-factor). Prior to analysis of intracellular NADH, the system's G-factor was determined from the control data, using a tail-matching approach (42), where:

$$G = \frac{I_{\parallel}}{I_{\perp}} \tag{4}$$

at the tail of the fluorescence decays. Because the signals of NADH were detected by two separate MCPs, the purpose of this control is to correct for any potential bias between them (42). This G-factor is used together with the measured fluorescence intensity from each channel to calculate the anisotropy of fluorophore over the field of view:

$$r(t) = \frac{I_{\parallel}(t) - G \cdot I_{\perp}(t)}{I_{\parallel}(t) + 2G \cdot I_{\perp}(t)} \tag{5}$$

For a mixture of multiple species of different sizes and population fractions, the overall anisotropy is multi-exponential, such that:

$$r(t) = \Sigma \beta_i e^{-t/\tau_i} \tag{6}$$

However, the substantial difference in both the fluorescence lifetime and sizes of enzyme bound NADH and free NADH often leads to a more complex form of anisotropy (associated anisotropy). Here, we have a mixture of two independently rotating fluorophores that produces a combination of rapid segmental motions together with slow

overall rotational diffusion. The resulting trend is an associated anisotropy decay, where the anisotropy curve decays rapidly to a minimum first (free NADH) then increases before another slower decay (enzyme-bound NADH). The enzyme-bound population is recognized by a combination of significantly slower rotational motion as well as a longer fluorescence lifetime compared to those of the free species (42). The overall anisotropy is attributed to the total anisotropy signals from each species together taken into account their fractional intensities such that (42):

$$r(t) = f_{free} \cdot r_1(t) + f_{bound} \cdot r_2(t) \tag{7}$$

where the anisotropy of each component (free or enzyme bound) is represented by r_1 and r_2, respectively.

The fractional intensity contributed by each species is shown by f_{free} and f_{bound} and calculated from their population fractions and lifetimes:

$$f_{free}(t) = \frac{\alpha_1 e^{-t/\tau_1}}{\alpha_1 e^{-t/\tau_1} + \alpha_2 e^{-t/\tau_2}}$$

$$f_{bound}(t) = \frac{\alpha_2 e^{-t/\tau_2}}{\alpha_1 e^{-t/\tau_1} + \alpha_2 e^{-t/\tau_2}} \tag{8}$$

The fitting equation that is used for associated anisotropy can be obtained by inserting equations 6 and 8 and to equation 7:

$$r(t) = \frac{\alpha_1 e^{-t/\tau_1} \cdot \beta_1 e^{-t/\varphi_1} + \alpha_2 e^{-t/\tau_2} \cdot \beta_2 e^{-t/\varphi_2}}{\alpha_1 e^{-t/\tau_1} + \alpha_2 e^{-t/\tau_2}} \tag{9}$$

Similar to 2P-FLIM statistical analysis, the anisotropy parameters are extracted from the fitting curve, and the average values together with standard deviations were calculated using the ANOVA function of OriginPro 8.0. Comparisons between culture types and before and after treatment were done using Student's *t*-tests also in OriginPro 8.0. Details regarding these analyses can be found at Appendix I.

Chapter III:

Metabolic differences of breast cancer cells in 2D and 3D cultures as monitored using 2P-FLIM

Disclaimer: Portions of this chapter were published‡ elsewhere and used here with permission.

‡A. Cong, R.M.L. Pimenta, H.-B. Lee, V. Mereddy, J. Holy, A.A. Heikal. 2019. Two-Photon Fluorescence Lifetime Imaging of Intrinsic NAD(P)H in Three-Dimensional Tumor Models. *Cytometry* (Part A), 95A, 80-92.

3.1 Rationale

Reduced nicotinamide dinucleotide (NADH) and its oxidized counterpart are coenzymes that are directly involved in cellular metabolic pathways like glycolysis and oxidative phosphorylation (32). The intracellular quantity of NADH together with its free and enzyme bound population ratio are indicative of the redox state within cells (33, 36, 44, 50). Here, we hypothesize that intracellular metabolic activities of breast cancer cells (4T1) in three-dimensional (3D) collagen matrix culture will be different from that in the traditional two-dimensional (2D) monolayer culture. In addition, the cellular responses to drug treatments are expected to vary depending on the type of culture in which these cells are grown. To test these hypotheses, we used two photon (2P)-fluorescence lifetime imaging microscopy (FLIM) as a real time, non-invasive, and quantitative approach to measure the intracellular populations of free and enzyme-bound NADH in 2D and 3D cultures as an intrinsic biomarker of cellular metabolic activities. In addition, similar measurements were carried out as a function of two newly developed cancer drugs, namely MD1 (47) and TPPBr (49). In these measurements, NADH was excited using 730-nm laser pulses (76 MHz, 120 fs) and its autofluorescence was detected using 450/100 nm filters (Chapter 2). Statistical analyses using ANOVA and Student's *t*-test were used to examine the significance of any observed difference among the fitting parameters of FLIM images as a function of the type of culture and drug treatment (Chapter 2 and Appendix I).

3.2 Results and discussion

3.2.1 Enhanced average fluorescence lifetime of NADH in untreated 3D cultures

To examine whether the type of cancer cell culture affect the metabolic activity, we conducted 2P-FLIM on 4T1 cells in 3D collagen matrix culture as a compared with the traditional 2D monolayer culture as a control without drug treatments.

Figure 3.1 shows the 2P-fluorescence intensity (Figure 3.1b and f) and 2P-FLIM images (Figure 3.1c and g) of intracellular NADH of 4T1 cancer cells in 2D and 3D cultures. In addition, the DIC images (Figure 3.1 a and e) provide the morphological context of the corresponding NADH autofluorescence. The Figure also shows the corresponding histogram of each FLIM images, which show the frequency at which a given NADH fluorescence lifetime is observed in the field of view.

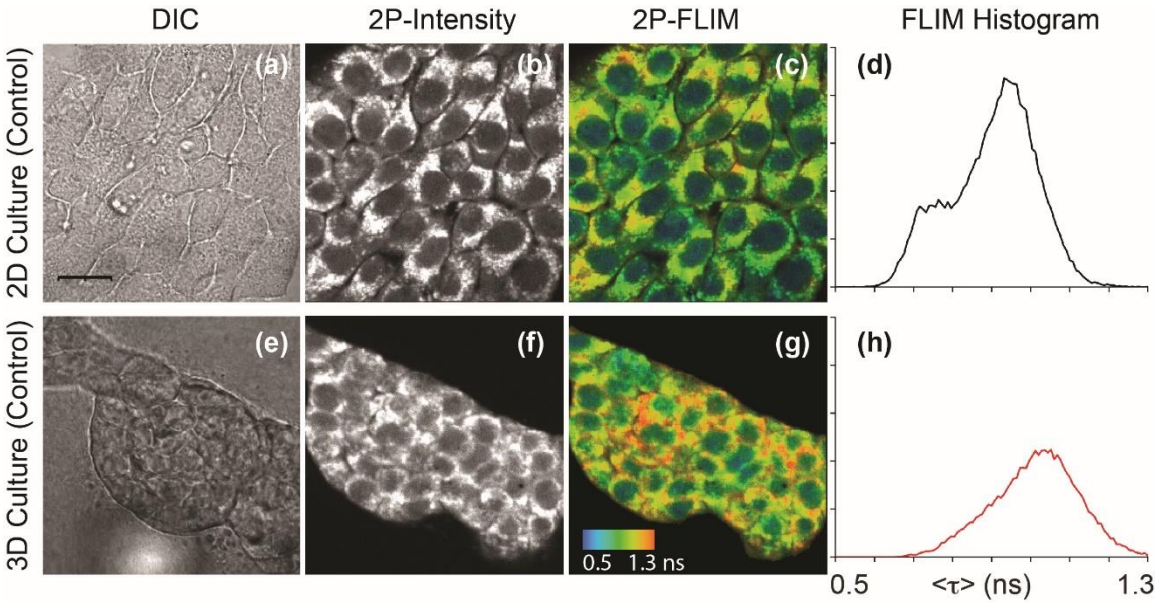

Figure 3.1: 2P-FLIM analysis of average NADH fluorescence lifetime in untreated cultures of 4T1 in 2D (top panels) and 3D (bottom panels). In the order from left to right, DIC images (a, e), 2P-Intensity (b, f), 2P-FLIM (c, g), and lifetime-frequency histograms (d, h) are obtained from cells at room temperature. The threshold for 2P-FLIM images are set based on the background signal, each image with binning number of 4. Black scale bar on DIC images represents 20 μm. The color code range for 2P-FLIM images is set between 0.5-1.3 ns, and y-axis range for the frequency histograms is 0-25,000.

Figure 3.1 shows that cancer cells that are grown directly on glass surface forms a 2D monolayer, where colonies are flat and spread outward across the field of view. In comparison, cells grown within the 3D collagen matrix forms multicellular acinar ducts and branches that are more resembling of *in vivo* breast tissues. These branches and colonies are often a few cells thick to about half-dozen cells thick (multilayer) and contracting the collagen matrix around them as they grow. These characteristics are consistent with those previously observed in other studies that use collagen matrix as a 3D breast cancer model (23, 24, 58). Using 2P excitation, the 2P-fluorescence intensity of NADH were recorded (Figure 3.1b and 3.1f) over the same field of view in the DICS images in order to provide a morphological context. Concentrations of NADH were found to reside mostly in the cellular cytosol (bright regions) with a low amount in the nucleus (dark circular regions).

The corresponding 2P-FLIM images (Figure 3.1c and 3.1g) were also recorded and first analyzed using the average fluorescence lifetime $<\tau>$ of intrinsic NADH per pixel. It is worth noting that the 2P-intensity and 2P-FLIM of cellular NADH are related where the integrated fluorescence decay per pixel in the FLIM image is basically the same as the 2P-intensity of the same pixel in the 2P-intensity image. In addition, the autofluorescence decay of NADH per pixel is best described as a biexponential decay (see Chapter 2, equation 1). The fluorescence lifetime in each pixel is color coded by a lifetime range from 0.5-1.3 ns. From each image, a frequency histogram is produced over the same lifetime range (Fig 3.1d and 3.1h). The short fluorescence lifetime is assigned to free NADH (blue-green shade), which can be seen in the nucleus (round regions with relatively weak signal) as well as throughout the cytosol. This is plausible in regard to previous characterization studies that reported the majority of cellular NADH fluorescence signal coming from the mitochondria (33). The autofluorescence of the enzyme bound population of NADH (orange-red shade), however, exhibits longer lifetime and resides predominantly within the cytosol, where glycolysis and oxidative phosphorylation (mitochondria) take place. Regional analysis showed that the average fluorescence lifetime of NADH is consistently shorter in the nucleus than in the cytosol.

The lifetime-frequency histogram (Fig 3.1d) of the 2P-FLIM image of NADH in 2D culture exhibits a dominant peak around 0.95 ns with a shoulder at 0.75 ns, assigned to enzyme-bound and free NADH populations, respectively. Interestingly, the lifetime histogram of the 2P-FLIM of NADH in 3D culture (Fig 3.1f) reveals one peak around 1.5 ns, which is longer than that in 2D culture. The observed longer lifetime in 3D culture is attributed to a larger population of enzyme-bound NADH as well as enhanced fluorescence quantum yield due to the environmental restriction of 4T1 cells in the collagen matrix.

We further investigated this observed trend to distinguish between the environmental effects on the population fractions (α_i) and the fluorescence lifetime (τ_i), which is related the fluorescence quantum yield of cellular NADH. Towards that goal, we plotted the distribution of each fitting parameter in representative 2P-FLIM of NADH in 2D and 3D cultures as shown in Figure 3.2. These fitting parameters include the fractional amplitude of free NADH (α_1) and enzyme-bound NADH (α_2) as well as lifetime of free NADH (τ_1) and enzyme-bound NADH (τ_2). Visible differences can be seen in the side-by-side analysis of the 2P-FLIM images (2D and 3D) and their corresponding overlay histograms (the column to the right). At the end of each analysis, a χ^2 distribution ($\chi^2 = 1.1 \pm 0.1$) was obtained to confirm the quality of the fit (Fig 3.2, bottom panels). For visual comparison, Figure 3.2 also shows the average fluorescence lifetime of NADH in 2D and 3D per pixel (as in Figure 3.1). It is worth mentioning that the number of cells in the field of view in 2D and 3D cultures may vary as shown in the 2P-FLIM images and the corresponding frequency histograms.

We observed a minor enhancement of the fluorescence lifetime (τ_1) (Figure 3.2f) with a slightly reduced population (Figure 3.2l) of the free NADH in 3D culture as compared with 2D. This suggest minor changes in the environmental restriction surrounding the free NADH along changes in the metabolic activities in the 3D collagen matrix. In addition, the fluorescence lifetime (τ_2) of the enzyme-bound NADH in 3D culture is larger than that in 2D as shown in Figure 3.2i. In addition, the population fraction of the enzyme-bound NADH is also larger in 3D than that in 2D culture (Figure 3.2o). The χ^2-histogram (Figure 3.2r) indicate good fitting quality per pixel in each FLIM images of cellular NADH.

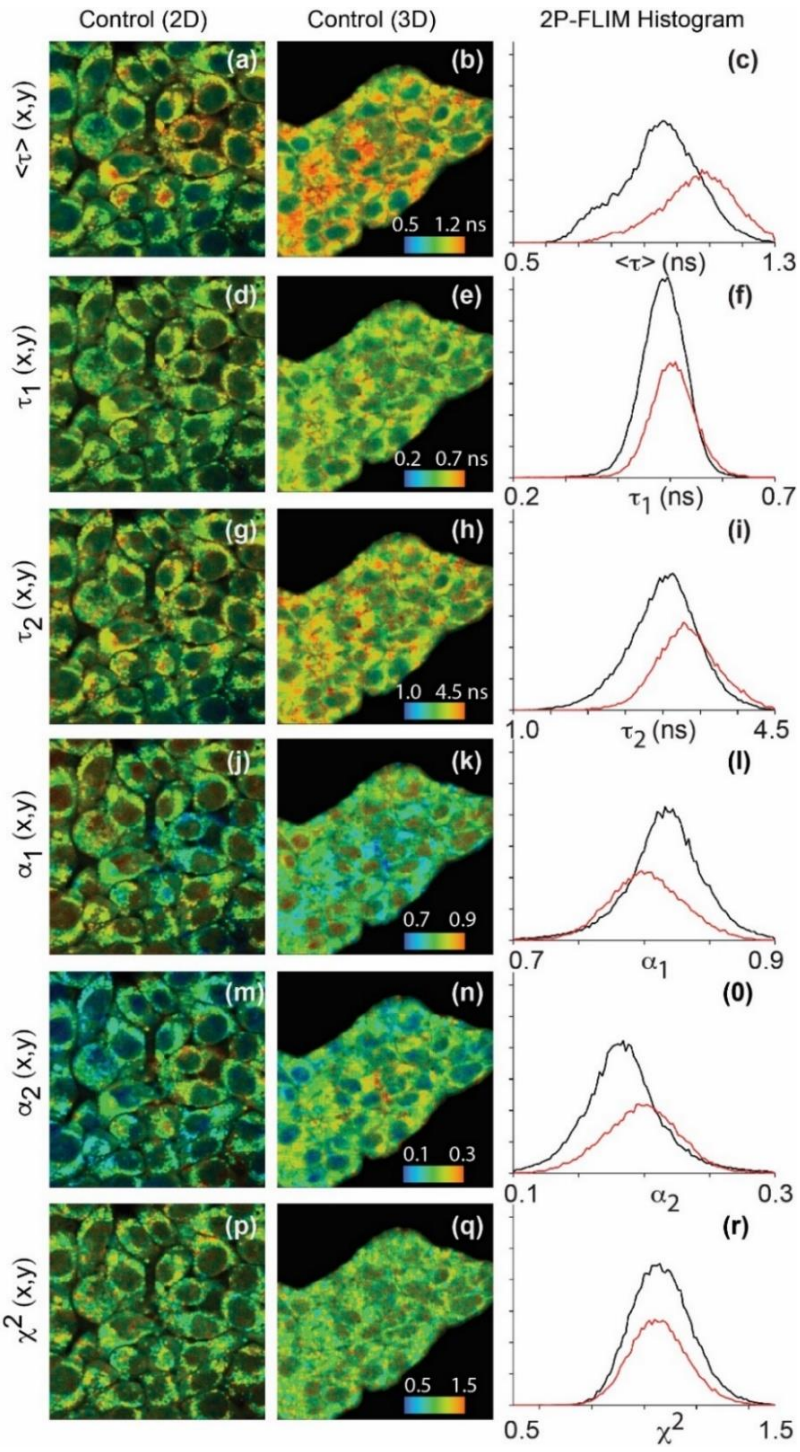

Figure 3.2: Summary of 2P-FLIM analyses for NADH parameters from 4T1 cultures grown as a 2D monolayer (first column) and in 3D collagen matrix (second column). From each analysis, a histogram is extracted as a black line to represent 2D culture and 3D culture in red (last column). The y-axis for each histogram is the pixel frequency of the parameter, in a range of 0-32,000. The frequency is not normalized for the number of cells in each image. The scale bar represents a length of 20 μm.

3.2.2 Statistical comparisons between 2P-FLIM of intracellular NADH in untreated 2D and 3D cultures

Statistical analyses for each NADH parameter over many trials were carried out to compare the metabolic state of untreated metastatic breast cancer 4T1 grown as 2D monolayer and in 3D collagen matrix. Average values of these parameters along with their standard deviations were calculated using the *ANOVA* function of OriginPro 8.0 and reported in the below Table 3.1. These calculations were followed by statistical comparisons between parameters from different culture types (2D versus 3D) using Student's *t*-test or Welsch's *t*-test depending on sample population characteristics (Figure 3.3). Statistical analysis with $p < 0.05$ was used to determine significant differences between values from the two samples (or set of trials). The results of these statistical analyses are summarized and depicted in a bar graph shown as Figure 3.3.

Table 3.1: A summary of 2P-FLIM fitting parameters for NADH intracellular fluorescence within untreated 4T1 cultures grown in 2D monolayer and 3D collagen matrix.

4T1 Cultures	α_1 (%)	τ_1 (ns)	α_2 (%)	α_2 (ns)	q_1 (%)	q_2 (%)	$<\tau>$ (ns)
2D (n = 31)	82 ± 2	0.48 ± 0.03	18 ± 2	2.8 ± 0.5	43 ± 3	43 ± 3	0.92 ± 0.12
3D (n = 31)	81 ± 1	0.50 ± 0.02	19 ± 1	3.1 ± 0.3	40 ± 2	60 ± 2	1.00 ± 0.08

From Student's *t*-tests analysis, the average autofluorescence lifetime ($<\tau>$) of NADH in 3D cultures of untreated 4T1 is significantly different from that of 2D cultures ($p = 0.0024$). Significant difference is also observed in the fluorescence decay time of enzyme-bound fluorophores (τ_2) with $p = 0.0039$. Significant differences are also found in the emitted autofluorescence of the free species q_1 ($p = 0.0019$) and the emitted autofluorescence of the bound species q_2 ($p = 0.0018$). In contrast, analyses show that there is not a significant difference ($p > 0.05$) between the fluorescence lifetime of the fast species or free NADH

(τ_1) as well as the population fractions assigned to both free (α_1) and enzyme-bound species (τ_2). The number of trials (*n*) represents the total number of measurements, using replicate from numerous dishes, different cell populations from each dish, as well as different days of experiments.

As observed from the average lifetime-frequency histograms (Figure 3.1d, h and Figure 3.2c), the average autofluorescence lifetime of NADH in 3D culture of untreated 4T1 consistently exhibits a shift towards longer lifetime compared to that in 2D culture. This observation is further validated with the significant difference that is found from our *t*-tests, where the average lifetime of NADH in 3D culture is significantly longer than that in 2D monolayer. This is attributed to the significantly slower fluorescence decay of the enzyme-bound species (τ_2) in 3D collagen matrix, which consequently impacts the differences in signal levels from both culture types. While the majority of NADH autofluorescence resides in the cytosol (70-80%), some signal is observed within the nuclei (20-30%) from both 2D and 3D cultures. This is likely in correlation with our previous observations about the difference in NADH concentrations between these two regions from our 2P-intensity images.

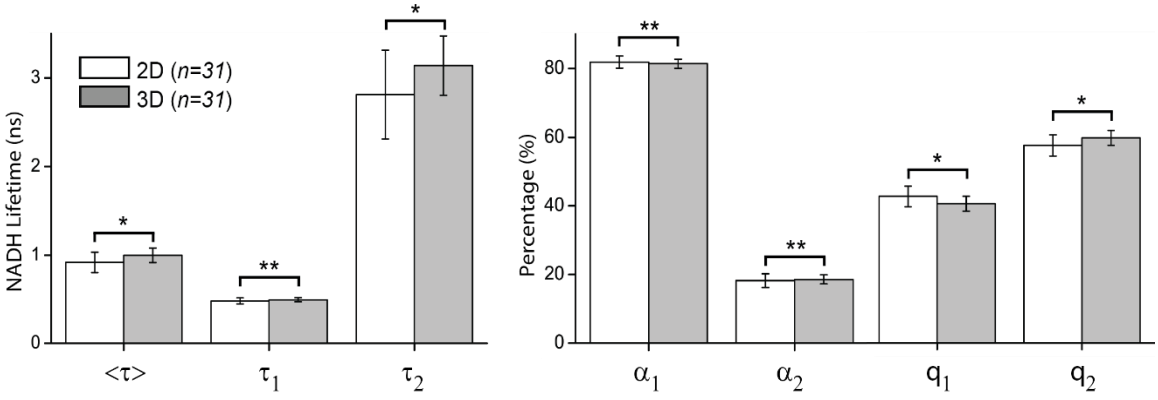

Figure 3.3: Summary of statistical analyses and comparisons (2D versus 3D) between NADH parameters obtained from 2P-FLIM of untreated 4T1 cultures. The left panel shows statistical analyses of the average NADH fluorescence lifetime (<τ>), the autofluorescence lifetime of free species (τ_1) and bound species (τ_2) from both culture types. The remaining analyses of the population fractions of free (α_1) and enzyme-bound NADH (α_2), as well as the autofluorescence signal from the corresponding species (q_1 and q_2) are reported on the right panel. Statistical difference between two samples indicated by a *p*-value < 0.05 is presented here as one asterisk (*), while two asterisks (**) represents no statistical difference (*p*-value > 0.05).

Previous single cell study on human breast tissues using a pixel-to-pixel analysis of 2P-FLIM images showed that the NADH autofluorescence signal from the cytosol is dominated by signal from the mitochondria (~86%), while a minor contribution is made from the remaining cytoplasm (~14%) (45). Thus, our intracellular NADH fluorescence signal that is averaged over the whole cell can be used as an indicator of metabolic states.

Environmentally induced differences in the metabolic state in cancer cells have been reported in triple negative metastatic human breast cancer cell lines (MDA-MB-231 and MDA-MB-468) when they are grown on collagen monolayers with varying density (59). It appears that these cells adapt a glycolytic shift when grown on denser collagen layers (3 mg/mL instead of 1.2 mg/mL), and this effect is accentuated in invasive cancer cells compared to a non-tumor cell control. Their inhibition study showed evidences of upregulated integrin signaling as a part of cellular mechanosensing pathway that directs these metabolic shifts in response to the extracellular matrix density. The metastatic cell lines grown on both collagen densities in that study also exhibited a significant oxidative shift compared to those on a glass surface, similar to our findings between 2D monolayer and 3D collagen matrix cultures.

Cannon et al. have investigated 2D monolayer and 3D xenograft of BT474 and HR6 cultures and reported an average NADH fluorescence lifetime that is significantly higher in 2D monolayer compared to 3D organoids, opposite from our observation (60). However, the 3D cultures in their study were obtained from a tumor xenograft and not an *in vitro* 3D collagen matrix. This is important to note as metabolic differences can also be expected between different types of three-dimensional culture models. The average fluorescence lifetime distributions reported by them, nonetheless, are similar to our current study, where 2D culture produces a wider, bimodal distribution of NADH average lifetime and 3D culture has a more narrow, single-exponential distribution.

3.2.3 Environmental effects on cellular metabolic response to drug treatments

The effects of extracellular matrix on cellular responses to drug treatments are important especially to therapeutic drug development and preliminary stages of drug screening. To examine the metabolic responses of different cultures (2D and 3D) of 4T1 cells, we compared the 2P-FLIM of intracellular NADH in 4T1 cells cultures as a function of MD1 and TPPBr treatment using the average fluorescence lifetime per pixel (Figure 3.4).

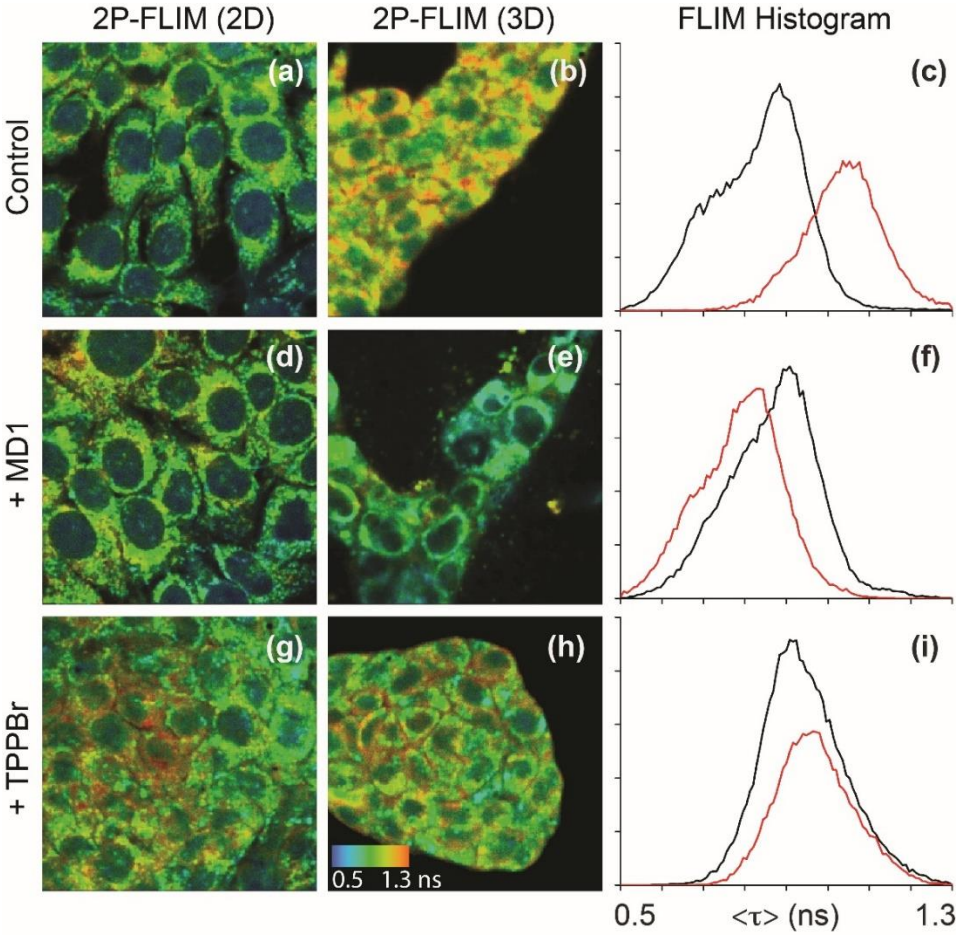

Figure 3.4: Comparative studies of environmental effects on 4T1 cellular responses to two anticancer drugs, MD1 (an MCT1 and MCT4 inhibitor) and TPPBr (an OXPHOS inhibitor). Representative of 2P-FLIM images showing NADH average autofluorescence lifetime for each culture type (2D: black histogram curve; 3D: red histogram curve) before (a, b) and after treatments (d-h) are shown here. The scale bar represents 20 μm, and the lifetime range used for color coding is between 0.5-1.3 ns. Once again, the overlaying average lifetime-frequency histograms of 2D and 3D cultures under the same treatment show visible differences between the two, before and after treatments (c, f, i). The frequency in these histograms is not normalized with respect to the number of cells in each culture.

The corresponding frequency histogram for each 2P-FLIM image is also shown for MD1 (Figure 3.4f) and TPPBr (Figure 3.4i) treatments as well as the control (Figure 3.4c). The detailed fitting parameters of each pixel are also summarized in Table 3.2.

Table 3.2: Summary of 2P-FLIM parameters from 2D monolayer and 3D collagen matrix cultures of 4T1, before and after treatments of two metabolic drugs MD1 and TPPBr.

4T1 Cultures	α_1 (%)	τ_1 (ns)	α_2 (%)	α_2 (ns)	q_1 (%)	q_2 (%)	$<\tau>$ (ns)
2D: MD1 (n = 15)	80 ± 2	0.50 ± 0.02	20 ± 2	3.0 ± 0.2	39 ± 3	61 ± 3	1.00 ± 0.12
3D: MD1 (n = 15)	80 ± 4	0.44 ± 0.02	21 ± 2	2.5 ± 0.1	40 ± 2	60 ± 2	0.88 ± 0.07
2D: TPPBr (n = 18)	81 ± 2	0.52 ± 0.03	19 ± 1	3.1 ± 0.2	42 ± 3	58 ± 3	1.02 ± 0.10
3D: TPPBr (n = 23)	83 ± 2	0.50 ± 0.01	17 ± 2	3.1 ± 0.1	43 ± 3	57 ± 3	0.96 ± 0.05

These results indicate that cellular responses to drug treatments significantly differ between 2D and 3D culture. In addition, the metabolic state of these drug-treated cultures (Figure 3.4f and 4.3i) seems different from that in the control counterpart (Figure 3.4c).

Before treatment (control), the average lifetime of intracellular NADH in 3D culture of 4T1 is significantly longer than that of its 2D counterpart (Figure 3.4c). The lifetime distribution for 2D culture is bimodal as compared with the single distribution for the 3D culture. Upon MD1-treatment (Fig 3.4c, f), the overall metabolic changes in the 4T1 cells differ from the control counterpart in a manner that is dependent of the culture. For example, the average NADH fluorescence lifetime distribution shifts towards a shorter lifetime in 3D culture as compared with the 2D culture, which is attributed to a significant glycolytic shift in the cellular energy metabolism in the collagen matrix. Our fitting

parameters (Table 3.2) indicate that the average fluorescence lifetime of NADH decreases from 1.00 ns (± 0.08) in control 3D culture to 0.88 ns (± 0.07) upon MD1 treatment. The corresponding change in the average lifetime of NADH is 0.92 ± 0.12 ns in 2D control culture as compared with 1.00 ± 0.12 ns for the MD1 treated counterpart.

As for the TPPBr treated cells, the average fluorescence lifetime of NADH of 4T1 cells in 3D cultures decreases from 1.00 ± 0.08 ns to 0.96 ± 0.05 ns, but increases from 0.92 ± 0.12 ns to 1.02 ± 0.10 ns in 2D cultures. It is worth noting that the frequency-lifetime histograms in MD1 cultures exhibit bimodal distributions as compared with the single distribution in TPPBr treated cultures (Figure 3.4i). Interestingly, the 3D culture treated with the OXPHOS inhibitor TPPBr also exhibit a minor glycolytic shift (Fig 3.4i) as judged from the average NADH lifetime distribution. In contrast, the lifetime distribution from 2D culture appears to shift slightly towards the oxidative direction as a result of TPPBr treatment. Further statistical analyses are carried out to assess the significance of any observed difference in cellular response to drug treatment in both 2D and 3D cultures (see below).

3.2.4 Statistical comparisons between 2P-FLIM of intracellular NADH in drug-treated 2D and 3D cultures

We hypothesize that the collagen-matrix in the tumor-like 3D model promotes 4T1 cells to be more energetic and thus induces higher sensitivity to metabolic drug treatments as compared with the 2D culture. To test this hypothesis, we carried out statistical analyses using Student's *t*-test in order to assess the significance of any observed differences between metabolic responses to drug treatments (MD1 and TPPBr) as a function of the 4T1 cell cultures (Figures 3.5 and 3.6). Below, we outline these statistical analyses as a means to compare the fitting parameters of all 2P-FLIM trials on 2D and 3D cultures as a function of the drug treatments. The number of trials (*n*) represents the total number of measurements, using replicate from numerous dishes, different cell populations from each dish, as well as different days of experiments.

(A) MD1 treatment of 4T1 cells in 2D and 3D cultures:

Overall, we observed significant differences between the average fluorescence lifetime $<\tau>$ ($p = 0.0035$), free NADH lifetime τ_1 ($p = 1.4 \times 10^{-7}$), and enzyme-bound NADH lifetime τ_2 ($p = 6.7 \times 10^{-8}$) measured for the MD1-treated 4T1 cells in 2D and 3D cultures. The remaining fitting parameters including population fractions of the free (α_1) and enzyme-bound species (α_2), as well as the fluorescence signals contributed by each species q_1 (free) and q_2 (enzyme-bound) are not significantly different ($p > 0.05$).

Comparing the effects of MD1 treatments between the two culture types, 4T1 grown as a 2D monolayer underwent a significant increase in the average NADH fluorescence lifetime ($p = 0.038$), which is in contrast of the significant decrease in the same parameter in the cells grown within the 3D collagen matrix ($p = 2.7 \times 10^{-5}$). The lifetime of free NADH (τ_1) did not change significantly after MD1 treatment in 2D culture ($p = 0.19$), but decreased significantly in 3D ($p = 2.0 \times 10^{-9}$). The lifetime of enzyme-bound NADH in both cultures changed by a significant amount, but in opposite directions. In 2D culture, for example, the average value for τ_2 increased slightly ($p = 0.047$) while decreasing by a much larger amount in 3D culture ($p = 7.1 \times 10^{-11}$). The fraction of free NADH population (α_1) decreased significantly in cells of 2D culture ($p = 0.0094$), and also decreased slightly but not by a significant amount in 3D culture ($p = 0.17$). The fraction of bound NADH population increased significantly for both 2D and 3D cultures ($p = 0.026$ for 2D and $p = 6.3 \times 10^{-5}$ for 3D). The fluorescence signal contributed by the free population (q_1) decreased significantly for cells from the 2D cultures ($p = 0.0039$), but not by a significant amount for 3D ($p = 0.34$). Similarly, the same parameter for the bound population (q_2) increased significantly in 2D monolayer ($p = 0.0035$), and did not change significantly for the 3D collagen matrix population ($p = 0.32$).

MD1 is a metabolic drug that targets the monocarboxylate transporters MCT1 and MCT4, which transport glycolytic products (lactate) between cancer cells to enhance the rate of ATP synthesis (47). Impaired lactate transporting pathway is expected to reduce glycolytic rate in glycolysis preferring cells, and oxidative phosphorylation in cells that rely on

imported lactate for ATP synthesis. Therefore, depending on the metabolic preference of the cells being treated, drug responses from individual cells can be different.

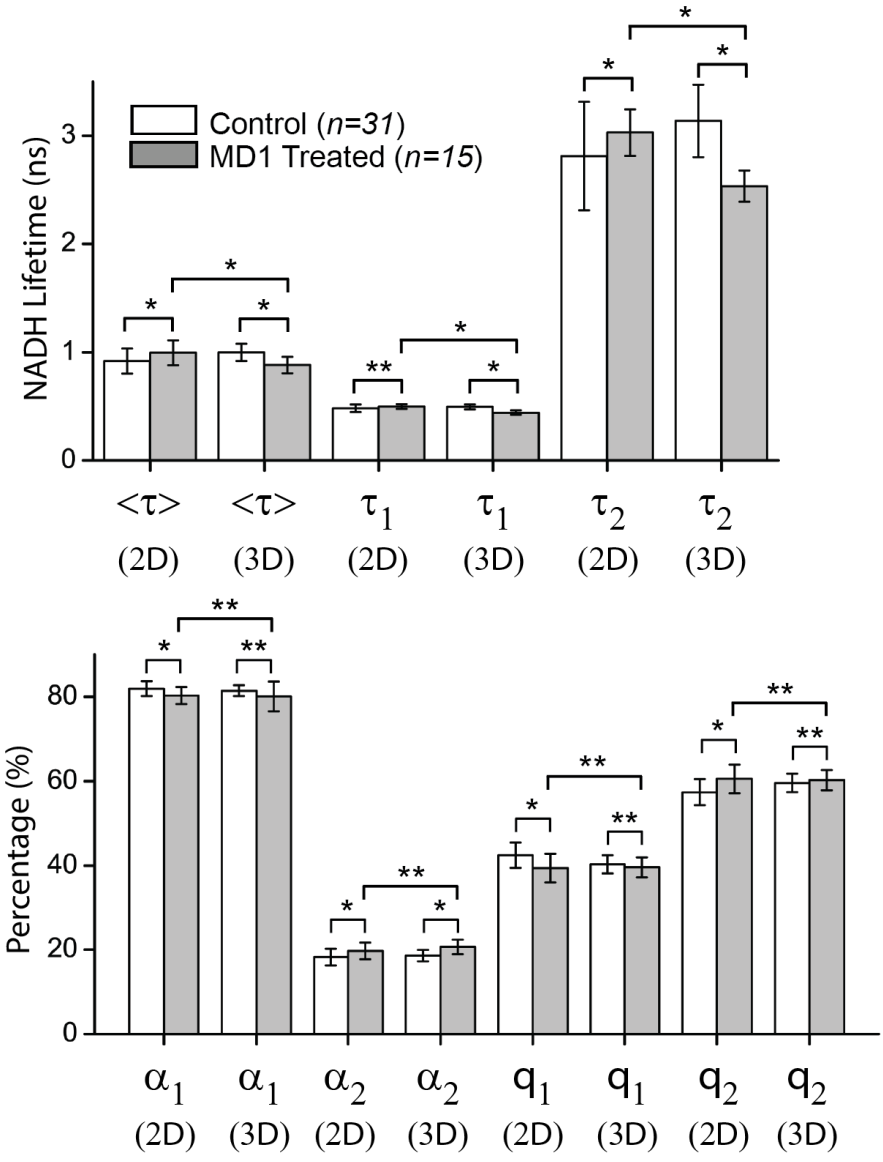

Figure 3.5: Statistical analyses of intracellular NADH parameters from both 2D and 3D cultures as a result of MD1 treatment. The top panel shows statistical comparisons of the average lifetime (<τ>), free NADH lifetime (τ_1), and bound NADH lifetime (τ_2) between the two culture types. The bottom panel describes the same comparisons between the free and bound NADH population fractions (α_1 and α_2) together with the fluorescence signal from each species, respectively (q_1 and q_2). Statistical difference between two samples is indicated by a *p*-value < 0.05 and presented here with one asterisk (*), while two asterisks (**) represents no statistical difference (*p*-value > 0.05).

From the perspective of colonies that are made from a population of cells, the overall expected impacts of MD1 are reduction in both glycolytic and oxidative activities (47). From our results, the NADH average fluorescence lifetime distribution of 3D culture had an apparent shift to shorter lifetime (more glycolytic), while in 2D, it changed slightly towards the longer lifetime direction (oxidative phosphorylation activities) (Figure 3.4c, f).

Changes to 2D culture were attributed to a reduction in the free NADH population, and increases in both the autofluorescence lifetime and population fraction of the enzyme-bound NADH. Meanwhile, the oxidative shift in 3D culture was directed by the reduction in fluorescence lifetimes of both free and bound NADH, together with an increase in the enzyme-bound NADH population fraction. Opposite metabolic responses were observed for 4T1 in 2D monolayer and the *in vivo* like 3D collagen matrix. Overall, the 3D culture seems to be more responsive to MD1 treatment than its 2D counterpart.

(B) TPPBr treatment of 4T1 cells in 2D and 3D cultures:

Similar statistical analyses were carried out to the 2D and 3D cultures treated with the second metabolic drug (namely, TPPBr). Significant differences were observed between the average fluorescence lifetime ($<\tau>$) of NADH within both treated culture types (p = 0.031). The fluorescence lifetime of the free coenzyme (τ_1) was significantly different between 2D and 3D cultures (p = 0.015), while the fluorescence lifetime (τ_2) of the enzyme-bound NADH was not significantly different (p = 0.83) in 2D and 3D cultures. Both the free and bound NADH population fractions (α_1 and α_2) were statistically different between 2D monolayer and 3D collagen matrix (p = 0.027 for α_1 and P = 0.027 for α_2). However, the autofluorescence signal contributed from free NADH (q_1) and enzyme bound NADH (q_2) had no significant differences between 2D or 3D cultures.

Looking at differences between the control and TPPBr-treated 4T1 cells in both cultures, the metabolic responses were also significantly different. While the average lifetime of NADH in 2D culture significantly increased with drug treatment (p = 0.0046), this parameter decreased significantly for cells in 3D culture (p = 0.031).

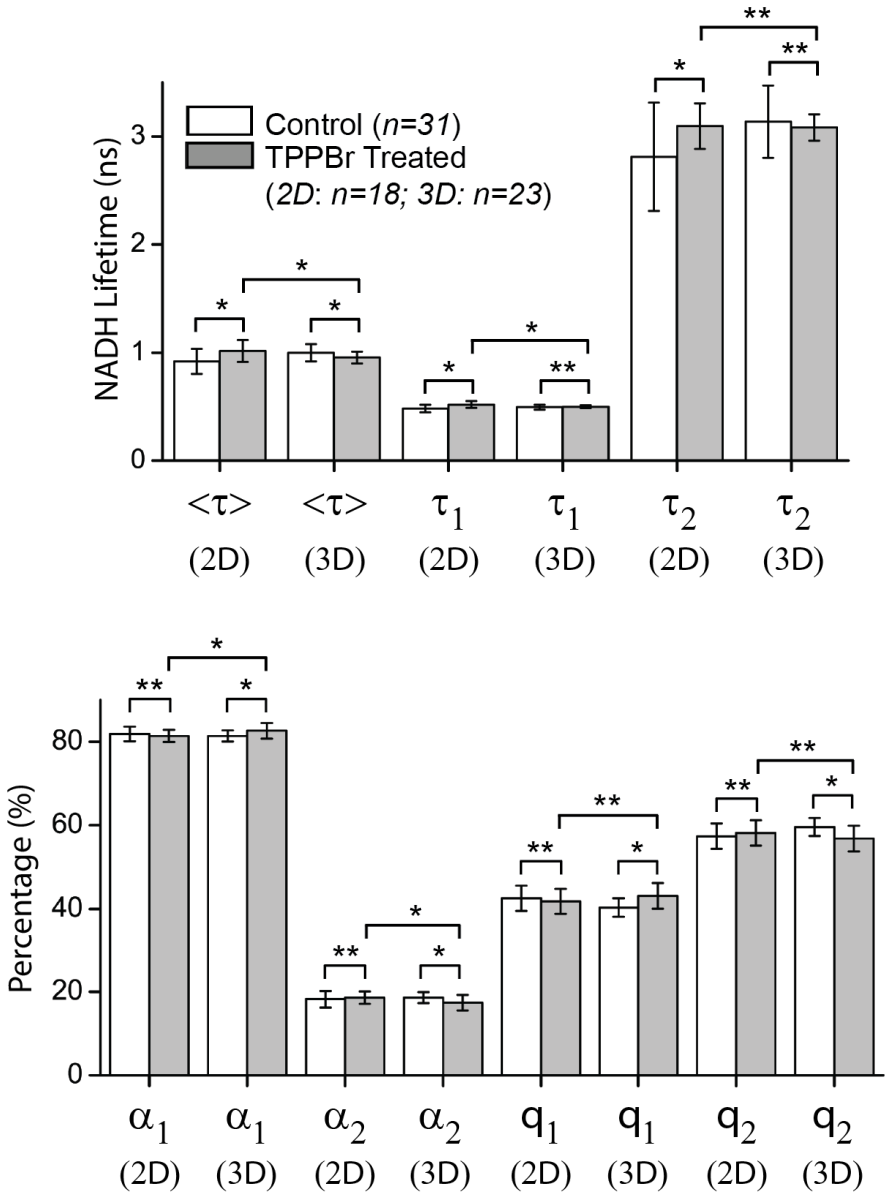

Figure 3.6: Statistical analyses of intracellular NADH parameters from both 2D and 3D cultures when treated with TPPBr. The top panel shows statistical comparisons of the average lifetime (<τ>), free NADH lifetime (τ_1), and bound NADH lifetime (τ_2) between the two culture types. The bottom panel describes the same comparisons between the free and bound NADH population fractions (α_1 and α_2) together with the fluorescence signal from each species, respectively (q_1 and q_2). Statistical difference between two samples is indicated by a *p*-value < 0.05 and presented here with one asterisk (*), while two asterisks (**) represents no statistical difference (*p*-value > 0.05).

Cells in 2D monolayer underwent a significant increase in both the fluorescence lifetime of free NADH (τ_1, $p = 0.00054$) and the fluorescence lifetime of enzyme bound NADH (τ_2, $p = 0.0080$). By comparison, there was no statistical difference between before and after treatment in both parameters from cells grown in 3D collagen matrix ($p = 0.56$ for τ_1, $p = 0.42$ for τ_2). The population fraction of each species (free – α_1, or enzyme-bound – α_2), related to their individual concentrations, are shown to have no statistical difference with the treatment of TPPBr for 2D cells ($p = 0.33$ and 0.50, respectively). In cells within collagen matrix, the fraction of the free species (α_1) increased significantly ($p = 0.0059$) while the fraction of enzyme bound NADH (α_2) decreased significantly ($p = 0.0075$).

As a result, there was no statistical difference in the fluorescence signal contributed by either species, free NADH (q_1) or enzyme bound (q_2) in 2D culture, with $p = 0.18$ and 0.16 respectively. On the contrary, the fluorescence signals for both NADH species in 3D culture were significantly different after treatment. Signal from free NADH increased ($p = 0.0003$) and decreased for enzyme bound NADH ($p = 0.0003$).

Overall, NADH parameters from our analyses showed signs of an enhanced glycolysis and a reduction in OXPHOS pathways in 4T1 cells that were grown in 3D collagen matrix, in agreement with the function of TPPBr as a mitochondrial OXPHOS inhibitor (49). The metabolic responses of monolayered cells to the same drug compound did not show any strong trend. The large increases in the average lifetime of NADH were contributed by increases in the fluorescence lifetimes of both free and enzyme-bound species, which can be due to a combination of changes in the local viscosity and pH that are known to affect the fluorophore's quantum yield (33). However, there were no significant changes in the remaining parameters, which might suggest that the metabolic state of 2D cells did not show a strong response to drug treatment. This could be Together with the observations from our MD1 treatment, it appears that 3D collagen matrix induces cellular metabolic activities to become more sensitive to chemical stimuli and potentially produce more accurate response to drug treatments than the conventional 2D monolayer. Similar conclusion was also made by Cannon and colleagues (60), where the magnitude of metabolic changes induced by treatments appeared to be lesser in 2D monolayer compared to their 3D organoids.

3.3 Conclusions

We conducted 2P-FLIM measurements and statistical analyses for intracellular NADH in 4T1 cancer cells in both 2D and 3D (tumor-like collagen matrix) cultures as a function of MD1 and TPPBr drug treatments. Metastatic breast cancer cells (4T1) in a 3D culture exhibit an oxidative shift, with a consistent mono-exponential average NADH lifetime distribution. In contrast, cells grown as a 2D monolayer are more glycolytic, with an average NADH lifetime distribution that is wider and often with bimodal frequency-lifetime histogram. Differences between the average NADH fluorescence lifetimes from both culture types are significant according to results from our statistical analyses. The significant difference that appears to be the main driving force behind this is the enzyme bound NADH autofluorescence lifetime.

Under the treatments of two different metabolic-targeting drugs (MD1 and TPPBr), 4T1 cells display responses that are quite inconsistent and almost opposite between the two culture types. From detailed statistical analyses of NADH parameters, our results suggest that the 3D collagen matrix plays a role in regulating cellular responses to MD1 and TPPBr drugs. Importantly, the observed trends upon drug treatments demonstrate the underlying action mechanisms for these novel drugs in manipulating cellular metabolic activities, which is enhanced in 3D culture as compared with the conventional 2D monolayer. Overall, our results indicate that the 3D collagen matrix seems to be a better environment to be used for drugs screening due to the higher sensitivity and more accurate responses that 3D cells provide compared to the conventional 2D monolayer.

2P-FLIM measurements of intrinsic NADH, though have unique spatial advantages, however, lack a high-temporal property. Enzyme-bound fluorophores often express a multi-exponential fluorescence decay, which can easily be mistaken for their free population that is already a bi-exponential decay (folded and stretched NADH conformations). The lifetimes of NADH, whether free or bound, are also sensitive to various environmental factors, including but not limited to pH, local viscosity, crowding, etc (33, 42). Due to these reasons, we extended our study using a method that can provide a high-temporal resolution to better our understanding of our intracellular fluorophores.

Chapter IV:

Monitoring metabolic activities of 4T1 in 2D and 3D cultures using the rotational dynamics of free and enzyme-bound NADH

4.1 Rationale

Two-photon FLIM approach for monitoring the metabolic activities in living cells using intrinsic NADH (Chapter 3) suffers from a few challenges. The temporal resolution of the recorded fluorescence decay in each pixel is usually low in 2P-FLIM in exchange for a high spatial resolution. Such low temporal resolution provides the benefit of avoiding cellular photodamage due to a longer exposure to femtosecond laser pulses at high repetition rate. More importantly, the fluorescence lifetime of a fluorophore, as the main variable in 2P-FLIM, is known to be sensitivity to environmental parameters such as pH, viscosity, and oxygen in a manner that depends on the molecular structure of the fluorophore (33, 42). In addition, the fluorescence lifetime of a given fluorophore is also sensitive to charge transfer and conformational changes (42). When more than one of these factors is present within the sample, the interpretation of 2P-FLIM becomes challenging. For example, the time-resolved fluorescence of NADH in a buffer decays as a biexponential (44, 45) with the fast decay time constant that is attributed to the folded conformation, where the fluorescent nicotinamide ring is closer to the adenine base and thus induces quenching. The slow decay component of NADH is assigned to the stretched conformation where the nicotinamide ring is apart from the adenine base. It is worth mentioning that when NADH is bound to an enzyme, the stretched conformation dominates, leading to an increase in the overall fluorescence lifetime.

To overcome these challenges, we used two-photon time-resolved fluorescence polarization anisotropy to quantify the rotational dynamics of the free and enzyme-bound conformations of intrinsic NADH. The rotational time is in direct relation with the hydrodynamic volume (or the size) of free NADH and is orders of magnitude smaller than that of the bound counterpart (33). In addition, the rotational time measured using time-resolved anisotropy is proportional with the viscosity of the surrounding environment (42, 45).

Here, we use two-photon time-resolved anisotropy of intrinsic NADH of 4T1 cells in 2D monolayer and 3D collagen matrix. These measurements complement the 2P-FLIM studies (Chapter 3) by directly providing the population fractions of the free and enzyme-bound NADH, contributing to a more accurate assessment of differences in cellular metabolic activities. Additionally, we applied time-resolved fluorescence anisotropy to investigate differences in metabolic responses of 4T1 cells in 2D and 3D cultures to MD1 (47) and TPPBr (49) treatments.

In these measurements, the two-photon autofluorescence of cellular NADH was excited using 730-nm laser pulses at lower repetition rate (4.22 MHz) to allow enough time for the molecule to relax to its ground electronic state (i.e., the same initial conditions at each excitation pulse). The autofluorescence was then polarization-analyzed and both the time-resolved parallel and perpendicular polarizations were detected simultaneously with a set of 450/100 nm and 690SP filters (Chapter 2). In these experiments, femtosecond laser pulses were used to scan over a number of cells and the parallel and perpendicular fluorescence photons were stored in 1024 time-bins to achieve high temporal resolution. As a result, we the laser pulses were not focused on a given pixel for an extended time and photodamage was avoided. However, a consequent disadvantage to this approach is the lack of high spatial resolution because we are averaging over a number of cells within the field of view. Statistical analyses of time-resolved anisotropy measurements were carried out using ANOVA and *t*-tests (Chapter 2 and Appendix I) to distinguish significant differences in the observed rotational dynamic parameters in 2D and 3D as well as a function of drug treatments.

4.2 Results and discussion

4.2.1 Simulations of associated anisotropy decay profile of two NADH populations at equilibrium

It is known that intracellular NADH exists as both free and enzyme-bound conformations (33, 44, 45). The population fractions of the intrinsic NADH have been used to define the corresponding metabolic state of living cells or tissues (33, 36, 50, 60). Experimental

evidences from the use of fluorescence-based techniques that support these two arguments is based on both time-resolved fluorescence microscopy imaging (45, 60, 61), as described in Chapter 2 and 3, and time-resolved anisotropy (44) measurements. It has also been established (Chapter 3) that the fluorescence lifetime of free NADH is distinct from its enzyme-bound counterpart (33, 55). In addition, the size (or hydrodynamic volume) of free NADH is very small compared with the enzyme-bound counterpart; depending on the type of enzyme involved in a given metabolic pathway.

With this in mind, we simulated the projected time-resolved associated anisotropy (equation 9, Chapter 2) of a mixture of free and enzyme-bound NADH that exist at equilibrium. The term "associated" is used to describe the rotational dynamics of two species of fluorophores with different fluorescence lifetime (or fluorescence quantum yield) and hydrodynamic volume (42). In these simulations, we used relevant time constants and amplitude fractions of both the fluorescence and anisotropy decays of NADH (44, 45). These parameters were fixed at constant values for a given simulation curve while changing one parameter at a time in a step-wise manner. The objective here is to use simulations curves of time-resolved associated anisotropy to guide our data interpretation of intracellular NADH in 4T1 cell cultures.

Figure 4.1 shows the simulation curves of time-resolved associated anisotropy of NADH where the amplitude fractions, the fluorescence lifetime and rotational times of free and enzyme-bound coenzyme varied, one at time, as a means to understand their individual effects on the time-resolved anisotropy profile. All the simulation parameters used in Figure 4.1 are summarized in Appendix II. In these simulations, the maximum initial anisotropy (r_0) on the y-axis is 0.4 as compared with the theoretical value of 0.572 for two-photon anisotropy measurements. Our reasoning for using 0.45 for the maximum initial anisotropy in these simulations is to expand the curves to emphasize the changes in profile.

Figure 4.1A shows the effect of the amplitude fractions associated with the fluorescence decays of free (α_1) and enzyme-bound (α_2) NADH, where $\alpha_1 + \alpha_2 = 1$, on the time-resolved associated anisotropy curves. The arrows in this panel indicate the direction of increasing the amplitude fraction (α_i). As the population amplitude (α_1) of free NADH increases, the enzyme-bound population fraction (α_2) decreases and vice versa. Within our

simulation range, the highest value for α_1 (0.9) results in the bottom curve with the steepest decay, which takes the longest time to rise back up due to the lowest amount of present enzyme bound NADH, or α_2 (0.1). As α_2 gradually decreases and α_2 increases, the minima (0-2 ns) moves up quite evenly with the amplitude of change. As α_1 reaches a minimum (0.1), the total population of NADH shifts from being bimodal to having mostly one single population of fluorophore, enzyme bound ($\alpha_2 = 0.9$). With continued increase of α_2, the anisotropy profile will ultimately undergo a switch from associated anisotropy to a mono-exponential decay once all available NADH molecules become enzyme-bound (Figure 4.1A). On the other hand, as the amplitude fraction of free NADH increases to reach 1.0, we would only see a single-exponential anisotropy decay with fast rotational time (curve not shown). These changes in the population fractions of free and enzyme-bound NADH are likely to be associated with changes in the metabolic or redox state of live cells due to either disease conditions, local environmental changes, or drug treatments.

Figure 4.1B and Figure 4.1C show the effect of the fluorescence lifetime of free NADH (τ_1), and enzyme-bound NADH (τ_2) as described in equation 9 (see chapter 2). Figure 4.1B shows that as the fluorescence lifetime (τ_1) of free NADH increases, there is a general down-shift of the anisotropy decay curve where the transition between the fast and slow anisotropy decay components becomes larger. It is interesting to note that as the fluorescence lifetime of free NADH approaches that of the enzyme-bound counterpart, the anisotropy decay becomes a biexponential due to the difference in the hydrodynamic volumes of both species in the mixture.

The complementary Figure 4.1C shows the effects of the fluorescence lifetime (τ_2) of enzyme bound NADH on the time-resolved associated anisotropy (equation 9, Chapter 2). An increase in τ_2 leads to a shift up of the transition period between the fast- and slow-rotational decay components, or the free and enzyme-bound NADH, respectively. As the value of τ_2 increases, the change between the resulting curves reduces exponentially, even with the same amount of τ_2 increment. This trend can be observed from top three curves (τ_2 increases by 1.0 ns) as well as the bottom three curves that still follow the associated anisotropy decay trend (τ_2 increases by 0.2 ns). When the value of τ_2 decreases and approaches that of τ_1, interestingly, the associated anisotropy curve also transforms into

what looks like an exponential anisotropy decay. Interestingly, the shape of the curve around the slow-rotational decay component is the same as Figure 4.1B, suggesting that the shape of the curve is the same whenever τ_1 is equal to τ_2 (at both 0.45 ns and 1.2 ns) as long as the remaining parameters are shared between two curves.

These changes in the fluorescence lifetime of the free (τ_1) and enzyme-bound (τ_2) NADH are likely to be associated with changes in cellular microenvironments in living cells surrounding NADH as well as the type of enzyme involved in the redox reaction that binds to this coenzyme. It is also conceivable that changes in the metabolic (or redox state) of live cells, due to either disease conditions, environmental effects, or drug treatments, could have similar effects on these fast and slow fluorescence lifetime components. For example, the fluorescence lifetime, associated with the fluorescence quantum yield of each species, has been shown to express larger enhancement upon binding when the temperature is lower (33, 42). Enzyme complexes that are ternary have been reported to have a longer bound NADH fluorescence lifetime compared to that of a binary counterpart. Changes in local environmental viscosity are likely to induce changes in refractive index, which are also known to impact the fluorescence lifetime of both free and enzyme-bound NADH. However, the influence of viscosity is generally less pronounced than that of enzyme binding (33).

Next, we tested the effects of the amplitude fractions of the anisotropy decay of free (β_1) and enzyme-bound (β_2) NADH (equation 9, Chapter 2) and the results are shown in Figures 4.1E and 4.1F. As the β_1- value increases, the initial anisotropy of the fast-rotational component of the free NADH increases (Figures 4.1E); with no effect on the corresponding rotational time or the corresponding amplitude of the enzyme-bound NADH. Meanwhile, the initial anisotropy (β_2) of the slow component associated with the enzyme-bound NADH affects predominantly the amplitude of the slow decay component of the anisotropy curve; shifting it up with each increment of the parameter (Figures 4.1E). In addition, the transition between the fast and slow decays seems to be steeper with higher value of β_2. For the curve with the lowest value of β_2 (0.05), the decay does not exhibit a strong associated anisotropy trend, but resembles that of a mono- or biexponential decay instead.

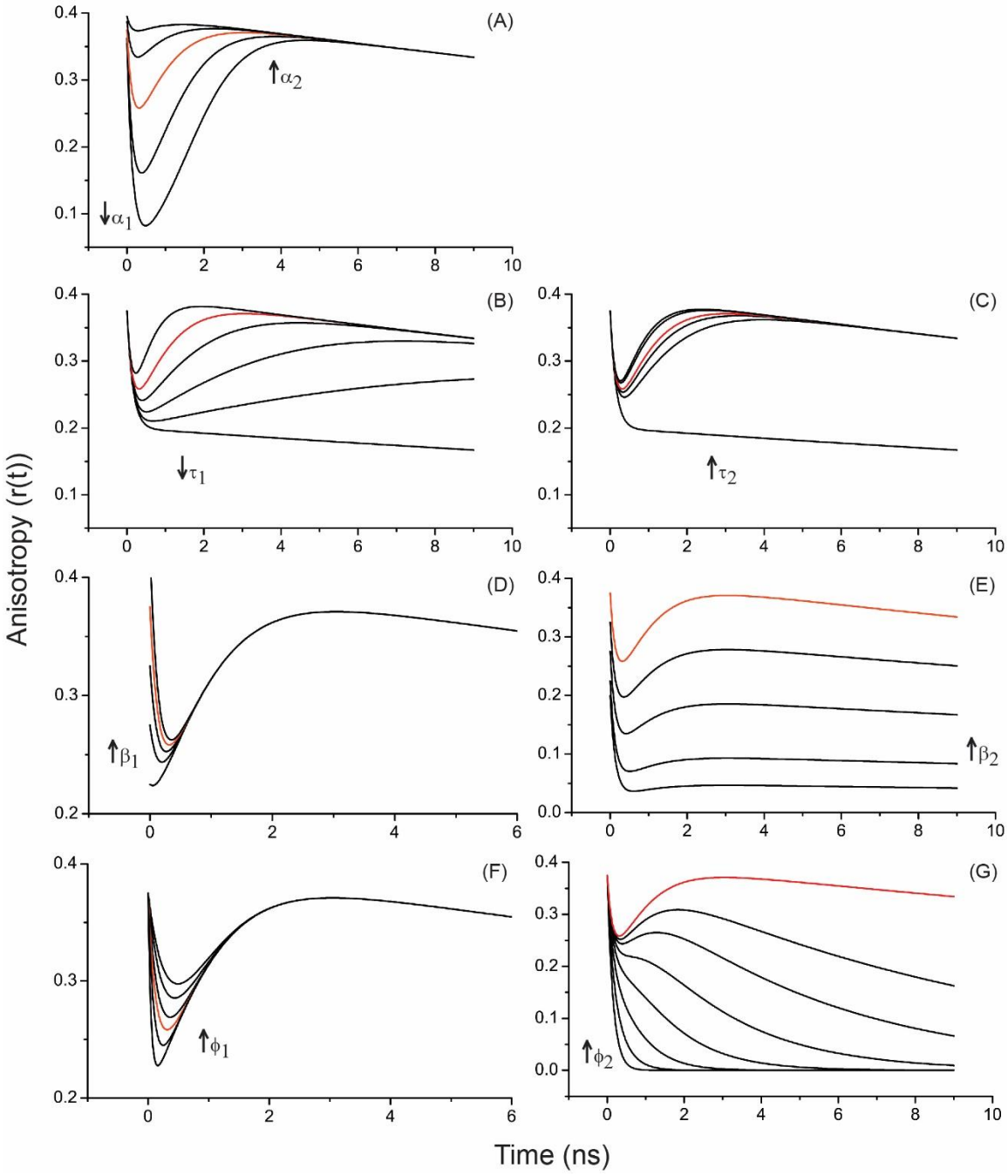

Figure 4.1: Simulations of associated anisotropy decay for a mixture of free and enzyme bound NADH. Impacts of individual parameters (increasing in the direction of arrows) on the overall decay were investigated, including (A) the population amplitudes of free (α_1) and enzyme bound NADH or α_2, (B) lifetime of free (τ_1) and (C) bound fluorophore (τ_2), (D) initial anisotropy of the free co-enzyme (β_1) and (E) its bound counterpart (β_2), (F) the rotational time of free NADH (φ_1) and (G) enzyme bound NADH (φ_2). The red colored curve present associated anisotropy decay with a set of parameters that are shared between these simulations.

Finally, we simulated the effects of the rotational time (ϕ_1) of free NADH and bound NADH (ϕ_2) on the time-resolved associated anisotropy profile, while the other remaining simulation parameters are kept constants (Figure 4.1F and Figure 4.1G). Changes of the fast-rotational time (ϕ_1) also results in up and down shifts of the fast-rotational decay component of free NADH, but it does not affect the rotational time of the enzyme-bound counterpart. The ϕ_1-based shifts in the anisotropy curves (Figure 4.1F) are not the same as those observed with changes in the amplitude fractions (α_1 & α_2); but they are complementary in determining the anisotropy decay profile (Chapter 2, equation 9).

Meanwhile, it is shown from our simulations that the rotational time of the enzyme bound species (ϕ_2) influences the second slow decay. When it is large and above the time range of our measurement (50 ns), the completion of the decay cannot be seen (top curve). As this slow rotational time decreases to be within 0-10 ns, we start to see a slow decay that comes to a completion. The associated anisotropy profile also diminishes and disappears with φ_2 value that is near and less than 1 ns, while the curves adopt an exponential decay shape. These changes in the rotational time constant (ϕ_i) of both free and enzyme bound NADH are likely to be associated with environmental restriction (e.g., viscosity) on its rotational mobility.

It is worth mentioning that the deviation in the overall initial anisotropy ($r_0 = \beta_1 + \beta_2$) from the theoretical value (0.572) in two-photon anisotropy measurements are attributed to ultrafast processes (e.g., energy transfer) that is beyond the temporal resolution uses in time-resolved anisotropy. Taken together, these simulations will guide our interpretation of experimental data on time-resolved associated anisotropy of intrinsic NADH in 4T1 cultures (2D and 3D) together with their responses to metabolic drug (MD1 and TPPBr) treatments as outlined in this chapter.

4.2.2 Anisotropy measurements of intracellular NADH from 4T1 cultures indicate two species at equilibrium with distinct fluorescence lifetimes and hydrodynamic volumes

According to the Stokes-Einstein model, the rotational diffusion time of a molecule depends on its hydrodynamic volume (or size) and the viscosity of the surrounding environment. Time-resolved anisotropy of NADH in a buffer exhibits a biexponential anisotropy decay at room temperature, which is attributed to two different structural conformations, folded and stretched (33, 42). The folded conformation is much more compact, thus decays at a rapid rate (< 0.5 ns), while the stretched conformation rotates on a relatively slower time scale due to the larger volume of solvent molecules being displaced.

When fully bound to lactate dehydrogenase (LDH) and mitochondrial malate dehydrogenase (mMDH), for example, NADH adapts the stretched conformation with an increased fluorescence lifetime (or quantum yield) and rotational time, which is due to the larger hydrodynamic volume. When fully bound to an enzyme, the time-resolved anisotropy of NADH in solution decays as a single exponential, indicating the restrictive effect that binding site(s) have on its rotational diffusion (44, 45). Interestingly, time-resolved anisotropy of a mixture of free and enzyme-bound NADH at equilibrium exhibits associated anisotropy profile due to the difference in fluorescence lifetime and the hydrodynamic volume of each species (44, 45).

In contrast with solution studies, however, intracellular NADH exists as free and enzyme-bound conformations, in heterogeneous microenvironments, based on a number of associated redox biochemical reactions at equilibrium (32). Such equilibrium between two species of cellular NADH exhibits time-resolved associated anisotropy due to the distinct fluorescence lifetime and hydrodynamic volume of each species as revealed by our simulations in section 4.2.1 (Figure 4.1). The observed associated anisotropy on intrinsic NADH seems consistent across different cell lines and tissues such as transverse hippocampal slices from rat brains (44), human breast normal cell line Hs578Bst, and cancer cell line Hs578T (45).

As a result, we carried out time-resolved 2P-autofluorescence polarization anisotropy of intrinsic NADH in 4T1 cells from 2D and 3D cultures. These measurements provide a direct assessment of the free and enzyme-bound NADH populations in the heterogeneous microenvironment in living cells while exploiting the inherent difference in the molecular weight of free and enzyme-bound NADH.

Figure 4.2 shows a representative time-resolved associated anisotropy of intracellular NADH in 4T1 cells in 2D culture (Figure 4.2D). The localized intracellular fluorescence of NADH populations within monolayer cells (Figure 4.1A) can be seen using 2P-FLIM measurement (Figure 4.2B). However, instead of collecting the average fluorescence decay of intracellular NADH from each pixel, the laser pulses (4.2 MHz, 120 fs) are scanned over a cell population similar to what shown in the DIC image, and the depolarized autofluorescence of intrinsic NADH is then separated into parallel and perpendicular fluorescence decays (Figure 4.2C) with respect to the polarization of the excitation laser pulses. The averaged time-resolved anisotropy decay over all the cells in the field of view (Figure 4.2D) is then calculated using these parallel and perpendicular polarizations. The observed associated anisotropy decay provides a direct evidence of the existence of two species of intrinsic NADH in untreated 4T1 cell in 2D culture.

The fitting parameters of this representation time-resolved associated anisotropy (Figure 4.2D) are shown in Table 4.1 and described by equation 9 (Chapter 2). According to our fitting parameters, the fast fluorescence lifetime and the corresponding amplitude fraction are assigned to the free NADH, where $\tau_1 = 0.53$ ns and $\alpha_1 = 0.54$ (equation 9, Chapter 2). The observed fast fluorescence lifetime is also associated with the fast-rotational time (ϕ_1) of the free NADH, where $\phi_1 = 0.19$ ns with an initial anisotropy fraction of $\beta_1 = 0.44$. In contrast, the enzyme-bound NADH has a relatively longer fluorescence lifetime ($\tau_2 = 1.29$ ns, $\alpha_2 = 0.46$), which is also associated with the slow rotating component ($\phi_2 = \infty$ ns, $\beta_2 = 0.41$) of the associated anisotropy (equation 9, Chapter 2).

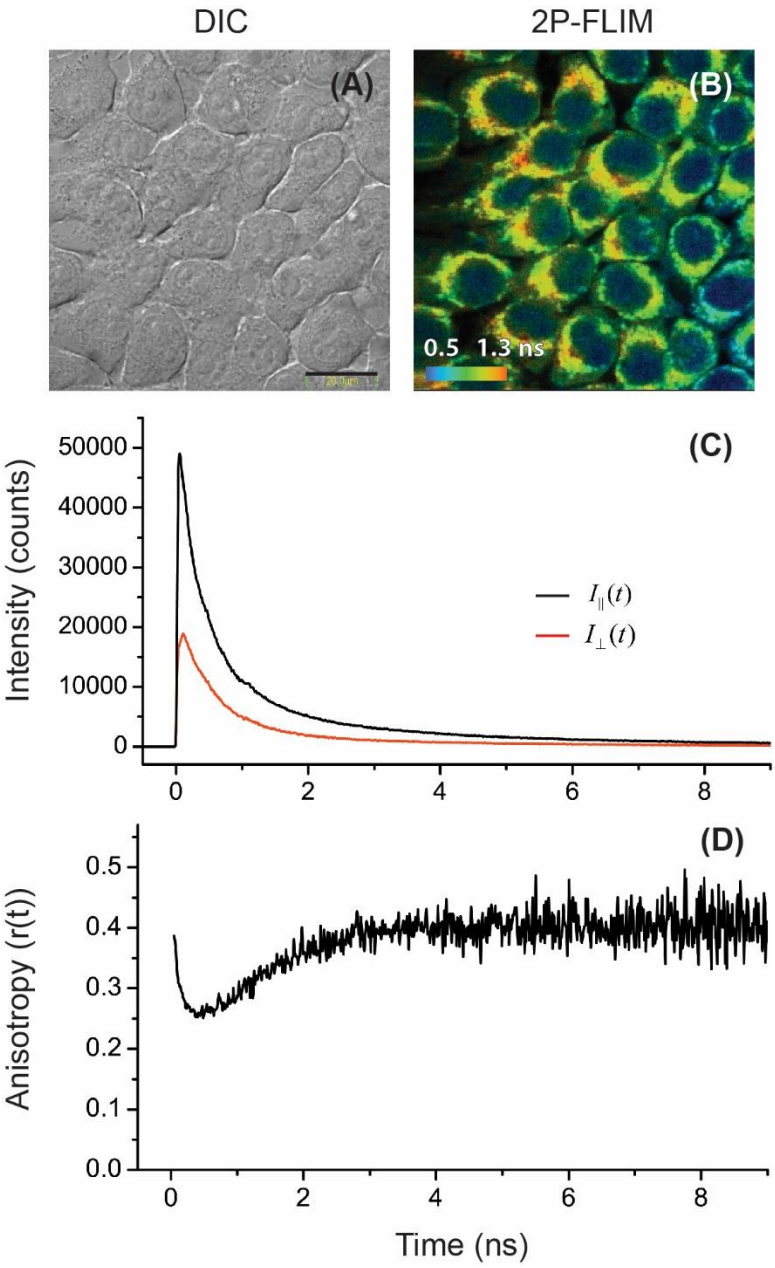

Figure 4.2: Representative (A) DIC image, (B) analyzed 2P-FLIM image for the average NADH fluorescence lifetime (C) parallel and perpendicular components of intracellular NADH fluorescence intensity, and (D) resulting anisotropy curve of untreated 4T1 cells from 2D monolayer culture. The parallel intensity signal is higher than that of the corrected perpendicular intensity signal, as expected. The associated anisotropy decay curve of intracellular NADH is consistent with previously published studies. The time range for 2P-FLIM analysis is presented by the color legend, from 0.5-1.3 ns. The scale bar on the DIC image represents a length of 20 μm.

Table 4.1: Fitting parameters for a representative associated anisotropy decay (Figure 4.2D) of 4T1 cells in 2D monolayer.

α_1	τ_1 (ns)	β_1	ϕ_1 (ns)	α_2	τ_2 (ns)	β_2	ϕ_2 (ns)
0.54	0.53	0.44	0.19	0.46	1.29	0.41	708

Based on these fitting parameters, the population fraction (α_i) and the fluorescence lifetime (α_i) were used to calculate the fractional amplitudes of each species in the mixture of intracellular NADH (see Chapter 2, equation 10). We determined from our calculations that 33 % of the mixture includes free NADH (*F*) as compared with 67 % for the enzyme-bound counterpart (*B*).

To take these analyses a step further, we treated the cells in a given culture as a "*black box*", where the specifics of the myriad of metabolic pathways, heterogeneous environments, and enzymes involved with cellular NADH are not known to us based in these types of experiments. In this black box model, we can only claim to know that there are two populations of NADH that are at equilibrium: one free and the other is enzyme bound, which is supported by our time-resolved associated anisotropy results. The same results provide us with the means to quantify the population fraction of free (*F*) and enzyme-bound (*B*) species in a given culture, where:

$$F \underset{}{\overset{K}{\rightleftharpoons}} B \tag{1}$$

where the corresponding overall equilibrium constant (*K*) is given by:

$$K = \frac{B}{F} \tag{2}$$

As a reminder, these two species on NADH differ in both the fluorescence lifetime (or quantum yield) and the hydrodynamic volume (or size), which yield the observed features of time-resolved anisotropy. In addition, we "associate" the fast fluorescence decay component and the fast-rotational component with the free NADH species as compared

with the slow components being associated with the enzyme-bound species. Based on the time-resolved associated anisotropy model, the overall fractions of the free and enzyme-bound populations are given by (Chapter 2):

$$F = \frac{\alpha_1 \tau_1}{\alpha_1 \tau_1 + \alpha_2 \tau_2} \tag{3}$$

and,

$$B = \frac{\alpha_2 \tau_2}{\alpha_1 \tau_1 + \alpha_2 \tau_2} \tag{4}$$

The corresponding Gibbs free energy changes ($\Delta G'$) associated with the metabolic shifts from each culture type were also calculated at room temperature (300 K), where:

$$\Delta G' = -RT \ln(K_{eq}) \tag{5}$$

where the gas constant (R) is 8.314 $Jmol^{-1}K^{-1}$.

With the assumption that the two species of intrinsic NADH (free and enzyme bound) exist at equilibrium, our rough calculations suggest an approximate equilibrium constant (K_{eq}) of 4T1 cells of about 2.0, where the amount of bound coenzyme is double that of the free counterpart. From this value of K_{eq}, the resulting Gibbs free energy change that is associated with this culture is approximately -1.7 kJ/mol.

We would like to emphasize that these calculations represent an average over the NADH in the cell population in a given field of view. This means that the time-resolved associated anisotropy approach lacks the spatial resolution inherent in 2P-FLIM, but with the advantage of high temporal resolution. Such compromise concerning the spatial resolution in time resolved anisotropy enable us to avoid photo-damage that may occur if we would focus the laser on a location in the live cell during the acquisition time. Importantly, these measurements and calculations concerning the enzyme-bound NADH are not enzyme specific.

Similar time-resolved associated anisotropy measurements and calculations on intrinsic NADH were carried out for numerous populations of 4T1 within a given Petri dish (2D or 3D), and repeated with different dishes as well as different days of experiment. We then carried out statistical analysis of these trials to determine the physical parameters that are significantly different in 2D and 3D cultures using Student's t-test and ANOVA platform in OriginPro (Chapter 2 and Appendix I). Our findings are outlined in the following section (4.2.3).

4.2.3 Statistical analysis of NADH anisotropy measurements on 2D and 3D cultures of 4T1 cells (untreated)

We carried out time-resolved associated anisotropy measurements of NADH in 4T1 cells in both 2D and 3D cultures as a means to elucidate environment-induced metabolic changes. Replicate measurements were carried out on different cell populations in a given Petri dish, with dishes from different days of cell cultures and different experiments (total number of measurements, n = 30-40) to assess our experimental data reproducibility. We then conducted statistical analyses on fitting parameters of NADH anisotropy in 2D monolayer and 3D collagen matrix cultures of 4T1 cells using Student's *t*-tests. The average values for the fitting parameters of each culture are summarized in Table 4.2.

Table 4.2: Average and standard deviation values for fitting parameters from associated anisotropy of intracellular NADH in untreated cultures of 4T1 (2D and 3D).

4T1 Cultures	α_1	τ_1 (ns)	β_1	ϕ_1 (ns)	α_2	τ_2 (ns)	β_2	ϕ_2* (ns)
2D (n = 31)	0.55 ± 0.03	0.46 ± 0.02	0.40 ± 0.02	0.19 ± 0.02	0.45 ± 0.03	0.96 ± 0.11	0.41 ± 0.02	∞
3D (n = 40)	0.47 ± 0.05	0.46 ± 0.04	0.39 ± 0.03	0.19 ± 0.04	0.53 ± 0.05	1.04 ± 0.15	0.37 ± 0.02	∞

* The rotational time of the enzyme-bound species is too slow compared with the excited-state lifetime (~ 100-10^{20} ns) and therefore its corresponding slow anisotropy component does not decay significantly during the detection window of 0–12.5 ns.

From our statistical analysis, 4T1 cultures grown as 2D monolayer have an average fractional amplitude (α_1) of 0.55 ± 0.03 (or 55 ± 3 %) for the fast-rotational component. The corresponding fluorescence lifetime of this species (τ_1) is about 0.46 ± 0.02 ns, with an initial anisotropy (β_1) of 0.40 ± 0.02 and rotational time (ϕ_1) of 0.19 ± 0.02 ns. In contrast, the second component (enzyme bound NADH) in 2D culture of 4T1 has a longer lifetime and much slower rotational time. The fluorescence lifetime of this species (τ_2) is 0.96 ± 0.11 ns, and its population amplitude (α_2) is on average at 0.45 ± 0.03 or 45 ± 3 %. The rotational parameter for this bound population includes the initial anisotropy (β_2) of 0.41 ± 0.02 and a rotational time (ϕ_2) that is $\sim\infty$ ns.

For 3D collagen cultures of 4T1, the average anisotropy parameters collected are slightly different (Table 4.2). Similarly, two different rotating components, one fast (free coenzyme) and one slow (bound coenzyme) were observed. For the free NADH population, the amplitude fraction in 3D culture (α_1) is around 0.47 ± 0.05 (or 47 ± 5 %). The fluorescence lifetime of this species is similar to its 2D counterpart, at about 0.46 ± 0.04 ns. The rotational parameters of the free coenzyme population include an initial anisotropy (β_1) of 0.39 ± 0.03 and a rotational time (ϕ_1) of 0.19 ± 0.04 ns. For the bound NADH population in 3D culture, the complex has, on average, a fluorescence lifetime (τ_2) at 1.04 ± 0.15 ns and a fractional amplitude (α_2) at 0.55 ± 0.05 or 55 ± 5 %. The initial anisotropy for this bound species (β_2) is around 0.57 ± 0.02 while the rotational time (ϕ_2) is also $\sim\infty$ ns.

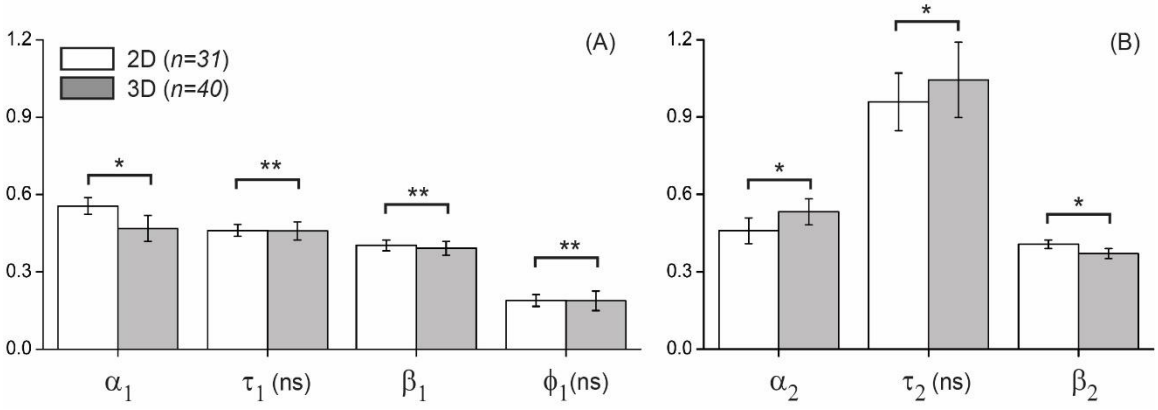

Figure 4.3: The statistical analyses of NADH anisotropy parameters of intracellular NADH of drug-untreated 4T1 in 2D monolayer and 3D collagen matrix cultures. The bar graphs present the average values for anisotropy parameters from each culture type, with standard deviation as error bars. The number of trials (*n*) on 2D cultures is 31 as compared with 40 trials on 3D cultures. Significant differences between two populations are represented here with one asterisk (*) from *p*-value < 0.05, while no significant difference is concluded with $p > 0.05$, and noted with two asterisks (**).

Figure 4.3 shows that the amplitude fraction (α_1) of free NADH as well as the amplitude fraction (α_2), the fluorescence lifetime (τ_2), the initial anisotropy (β_2) of the enzyme-bound NADH are significantly different ($p < 0.05$) in 2D as compared with 3D cultures of 4T1 cells (untreated). In addition, the time-resolved associated anisotropy results indicate that the fluorescence lifetime (τ_1), initial anisotropy (β_1), and the rotational time (ϕ_1) of free NADH are statistically the same in 2D and 3D cultures (i.e., no statistical difference). Interestingly, the estimated amplitude fractions of free (α_1) and enzyme-bound (α_2) NADH exhibit opposite trends in 2D and 3D culture. For example, the amplitude fraction of free NADH in 2D culture is larger than that in 3D culture of 4T1 cells. In contrast, the amplitude fraction of enzyme-bound NADH in 2D culture is less than that in 3D culture of 4T1 cells (Figure 4.3). This could be attributed to shifting the metabolic activities in 3D collagen matrix where more of the cellular NADH is bound to enzymes. Such a metabolic shift may also explain the observed enhancement of the enzyme-bound NADH in 3D collagen matrix (Figure 4.3B).

In Figure 4.3, the amplitude fraction of the fast rotating NADH species (free coenzyme, α_1) is found to be significantly ($p = 6.4 \times 10^{-13}$) shorter in 3D collagen matrix compared to that of 2D monolayer (Figure 4.3A). In contrast, the amplitude fraction of the slow rotating species (enzyme bound, α_1) is significantly ($p = 6.4 \times 10^{-13}$) higher in cells from 3D collagen matrix compared to that of 2D monolayer (Figure 4.3B). The fluorescence lifetime of enzyme bound NADH is also significantly higher from untreated 3D culture of 4T1 ($p = 0.0091$) compared to that of 2D culture (Figure 4.3B). However, the initial anisotropy of the bound species (β_2) is significantly ($p = 5.4 \times 10^{-12}$) lower in 3D culture compared to 2D culture of 4T1 cells.

Since the fluorescence lifetime (τ_1) and rotational time (ϕ_1) of free NADH are sensitive to surrounding environments, these results suggest that the local microenvironment of this small coenzyme is basically the same in 2D and 3D cultures. It is worth mentioning that the rotational time (ϕ_2) of enzyme-bound NADH is not statistically different in 2D and 3D cultures of 4T1 cells. This is expected since the rotational time of the intrinsic enzyme-bound NADH is too long (past the 0–12.5 ns observation window) compared with the excited-state fluorescence lifetime during which we monitor these rotational dynamics. Those enzyme-bound NADH may also be restricted by local microenvironments in living cells. It is known that as the rotational time of a large molecule becomes greater than 10 times the fluorescence lifetime, the uncertainty of the time-resolved anisotropy decreases (42). For the same reason, these time-resolved anisotropy measurements of intrinsic NADH is incapable of differentiating between the different types of cellular enzyme involved in different metabolic pathways in living cells.

Using these approximations and our statistical analysis of the time-resolved associated anisotropy measurements, we calculated the overall population fractions of free and enzyme-bound NADH, the corresponding equilibrium constant, and the Gibbs free energy ($\Delta G'$) for both 2D and 3D cultures of 4T1 cells as summarized in Table 4.3.

Table 4.3: Average fractions of free NADH (*F*) and enzyme bound NADH (*B*) and the corresponding values for NADH binding equilibrium constant (K_{eq}) together with the Gibbs free energy as calculated from anisotropy parameters of untreated 4T1 cells from both culture types. The average values and standard deviations were calculated over the number of trials (*n*) for each culture.

4T1 Cell Cultures (Untreated)	*F* (%)	*B* (%)	K_{eq}	$\Delta G'$ (kJ/mol)
2D Monolayer (n = 31)	38 ± 3	62 ± 3	1.7 ± 0.2	-1.3 ± 0.3
3D Collagen Matrix (n = 40)	28 ± 4	72 ± 4	2.7 ± 0.7	-2.4 ± 0.6

Approximately, the fraction of free coenzyme from untreated cells in 2D culture takes up about 38% while the remaining 62% represents the fraction of bound coenzyme from the same culture type. In untreated 4T1 cells from 3D culture, the free NADH fraction is found to be 28%, and the remaining 72% is attributed to that of the bound species. These estimates yield an equilibrium constant value of 1.7 for 4T1 cells from 2D culture as compared with 2.7 for cells in 3D collagen matrix. Our statistical comparisons using *t*-tests show that the fraction of fluorescence from free coenzyme (*F*) in untreated 2D culture is significantly higher than that of 3D culture ($p = 1.8 \times 10^{-17}$). The fraction of enzyme bound NADH (*B*), however, is significantly higher in 3D cultures comparing to that of the 2D counterpart ($p = 1.8 \times 10^{-17}$). Between untreated 2D and 3D cultures, both the calculated equilibrium constant of NADH binding and approximate change in Gibbs free energy from the redox ratio are also significantly different ($p = 2.9 \times 10^{-3}$ and 1.1×10^{-10}, respectively).

The $\Delta G'$ values for both culture types are negative, suggesting potential underlying redox biochemical processes involving coenzyme NADH that are generally spontaneous and thermodynamically favorable. It is also interesting to note that the magnitude of Gibbs free energy is higher in 3D culture compared to that in 2D, which might suggest a higher level of metabolic activities within 4T1 cells when grown in 3D collagen matrix.

These approximations suggest that the overall intracellular metabolic activities in untreated 2D culture of 4T1 involve a higher fraction of free NADH with a preference towards glycolytic pathways. On the other hand, the metabolic activities of 4T1 cells in 3D culture lean towards a more oxidative direction, as indicated by the significantly higher population of the bound NADH fraction. This is in a general agreement with our previous conclusions using 2P-FLIM measurements (Chapter 3). The significantly higher value of the longer fluorescence lifetime (of the bound species) in 3D culture in comparison to 2D culture is also worth noting, because the same observation was made from 2P-FLIM measurements (Chapter 3). Interestingly, significant differences in the parameters α_1 and α_2 between two culture types were not observed previously in our 2P-FLIM results, but are apparent in our anisotropy data. More detailed comparisons between the two techniques using calculated free and bound NADH fractions (*F* & *B*) will be discussed in further details in Chapter 5.

4.2.4 Statistical analysis of the associated anisotropy of NADH in 4T1 cultures as a function of TPPBr treatment

To examine the environment-dependent metabolic response of 4T1 cells to pharmaceutical drug treatments, we carried out complementary time-resolved fluorescence anisotropy measurements as a function on TPPBr and MD1 treatment in both 2D and 3D cultures. In this section, we will focus on the time-resolved associated anisotropy of NADH in 2D and 3D cultures of 4T1 as a function of TPPBr (49) treatment (Chapter 2) in this section. Note that these measurements were carried out on the same day of 2D and 3D cultures and two-photon time-resolved anisotropy measurements of TPPBr-treated and control (untreated) cells in different Petri dishes.

The time-resolved anisotropy of intrinsic NADH of 4T1 cells, in both 2D and 3D cultures, exhibit an associated anisotropy features similar to what is shown in Figure 4.2D when the cells are treated with TPPBr (as described in Chapter 2). The total number of measurements on TPPBr-treated and control cells (*n*) were collected using replicate from numerous dishes, different cell populations from each dish, as well as different days of experiments. These experimental data were statistically analyzed as a function of TPPBr treatments as

compared with the control cells (untreated). The fitting parameters of the observed associated anisotropy decays for both 2D and 3D cultures, treated with TPPBr, are summarized in Table 4.4. The fitting parameters of the control 4T1 cell 2D and 3D cultures (untreated) are summarized in Table 4.3 above.

Table 4.4: The fitting parameters of time-resolved associated anisotropy of intracellular NADH of 4T1 cultures (2D and 3D), treated with TPPBr. The standard deviation of the stated average value of each fitting parameter was calculated based on the number of trials.

4T1 Cultures (TPPBr Treated)	α_1	τ_1 (ns)	β_1	ϕ_1 (ns)	α_2	τ_2 (ns)	β_2	ϕ_2* (ns)
2D (n = 18)	0.52 ± 0.03	0.49 ± 0.05	0.42 ± 0.03	0.20 ± 0.02	0.48 ± 0.03	1.02 ± 0.18	0.41 ± 0.01	∞
3D (n = 22)	0.46 ± 0.05	0.48 ± 0.04	0.40 ± 0.03	0.21 ± 0.04	0.54 ± 0.05	1.04 ± 0.14	0.38 ± 0.01	∞

* The rotational time of the enzyme-bound species is too slow compared with the excited-state lifetime (~ 100-10^{20} ns) and therefore its corresponding slow anisotropy component does not decay significantly during the detection window of 0–12.5 ns.

For 4T1 cells in 3D collagen matrix, changes in anisotropy parameters were also observed upon TPPBr treatment as compared with control counterpart. The population amplitude of free coenzyme (α_1) is 0.46 ± 0.05 on average, and its fluorescence lifetime is about 0.48 ± 0.04 ns. The initial anisotropy of this fast-rotating species (β_1) is around 0.40 ± 0.03 with a corresponding rotational time (ϕ_1) of 0.21 ± 0.04 ns. Meanwhile, the fractional amplitude of the enzyme-bound NADH (slow decay component, α_2) is slightly higher at 0.54 ± 0.05. The average fluorescence lifetime of this species (τ_2) is unchanged (1.04 ± 0.14 ns) compared to untreated 3D culture. Both the initial anisotropy of enzyme bound NADH (β_2) and the slow rotational time (ϕ_2) are quite similar to untreated culture, with values of 0.38 ± 0.01 and ~∞ ns, respectively. To assess whether the observed differences among these fitting parameters are significant in 2D and 3D upon TPPBr treatment, we carried out statistical analyses using *t*-tests and compared our results with the control cultures. These

statistical analyses are shown in Figure 4.4 for both the free (Figure 4.4A) and enzyme-bound (Figure 4.4B) NADH.

Between treated 2D and 3D cultures of 4T1 (Figure 4.4), a few statistical differences were concluded among the anisotropy fitting parameters for both the free and enzyme-bound NADH. For example, the fractional amplitude of the free NADH (α_1) of 4T1 cells is significantly different ($p = 0.0025$) upon TPPBr treatment in 2D culture as compared with the control (untreated) counterpart. Our statistical analyses also indicate significant differences ($p < 0.05$) in the fast fluorescence lifetime (τ_1) between 2D and 3D cultures upon TPPBr treatments as compared with the control. The fast-rotational time (ϕ_1) of free NADH in 3D culture, treated with TPPBr, is also significantly different from the control, which suggest drug-induced changes in the restrictive nature of the local microenvironment of free NADH in 3D culture. The initial anisotropy of the fast component (β_1) is also significantly higher in cells from 2D monolayer compared to 3D collagen matrix with $p = 0.015$. There was no statistical difference between the two remaining parameters that belong to the fast component, the fluorescence lifetime (τ_1) and the rotational time (ϕ_1) due to values of $p > 0.05$. For the bound coenzyme (slow decay species), significant differences were found in the population fractions (α_2) between 2D and 3D cultures ($p = 7.2 \times 10^{-5}$) as well as their initial anisotropy (β_2) with $p = 1.1 \times 10^{-12}$. For the remaining parameter, the bound species fluorescence lifetime (τ_2), no significant difference was concluded from our statistical analysis ($p > 0.05$).

In 4T1 cells from 2D monolayer, the treatment of TPPBr induced a significant reduction in the free coenzyme's fractional amplitude (α_1) with $p = 0.0025$. In contrast, both the lifetime of this species (τ_1) and its associated initial anisotropy (β_1) increased by a significant amount ($p = 0.0047$ and $p = 0.003$, respectively). No statistical difference was found when comparing the rotational time of free NADH in 2D cells before and after drug treatment ($p = 0.25$). In addition, a significant difference was found from the fractional amplitude of the bound NADH population (α_2) with TPPBr treatment ($p = 0.0025$).

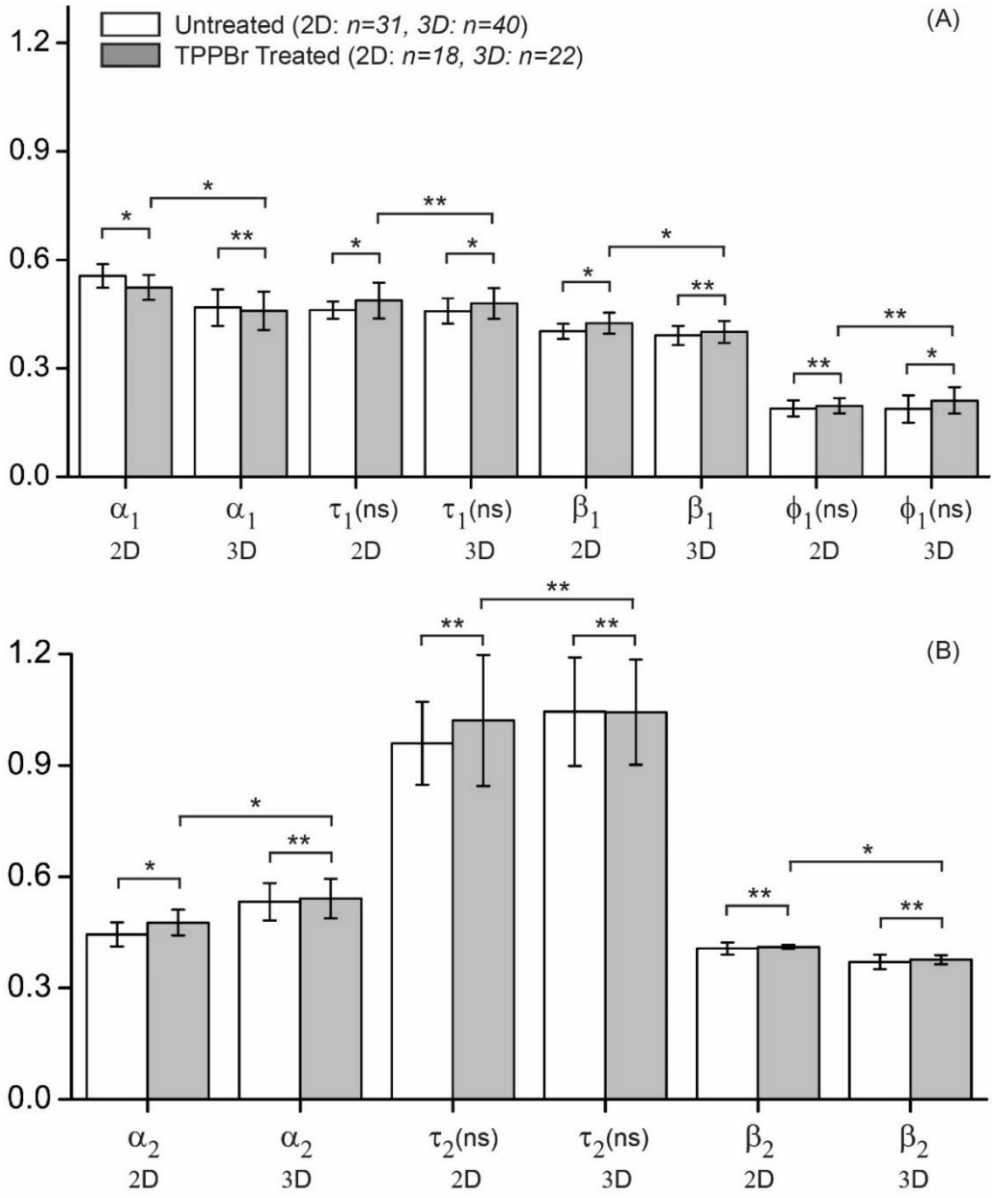

Figure 4.4: Statistical analyses of NADH anisotropy parameters from 4T1 cultures (2D monolayer and 3D collagen matrix) before and after TPPBr treatment. Parameters describing the fast decay component (free NADH) are shown in the upper panel (A) and the lower panel (B) contains parameters from the slow component (enzyme bound NADH). The bar graphs present the average values for anisotropy parameters from each culture type, with (grey) and without treatment (white), and their standard deviations are shown here as error bars. Significant differences between two populations (with p-value < 0.05) are represented with one asterisk (*), while no significant difference is concluded with p > 0.05, and noted by two asterisks (**).

The remaining parameters that represent the long fluorescence lifetime (τ_2) and the initial anisotropy of the enzyme bound species (β_2) had no statistical difference between their values before and after TPPBr treatment ($p > 0.05$).

The effects of TPPBr treatment on 4T1 cells in 3D collagen matrix are quite different from that of 2D monolayer. Between the parameters that describe the fast-rotating species, significant differences were observed in the fluorescence lifetime (τ_1) and the rotational time (ϕ_1) with values $p = 0.041$ and 0.024, respectively. However, no statistical difference was found for the fractional amplitude (α_1) or the initial anisotropy (β_1) of 3D culture as a result of TPPBr treatment ($p > 0.05$). Surprisingly, anisotropy parameters that are assigned to the slow decay component (enzyme-bound NADH) of cells in 3D collagen matrix were not significantly different after TPPBr treatment compared to the control cells from the same culture type ($p > 0.05$).

Considering the working mechanism of TPPBr as an oxidative phosphorylation inhibitor (49), it is expected that the metabolic activities within these cells would shift towards the glycolytic pathway to compensate for the dysfunctional mitochondria and therefore the oxidative phosphorylation pathway. However, this observation is not supported by our anisotropy parameters for 2D culture. Opposite trends were observed with a significant decrease in free NADH fractional amplitude (α_1) while the fraction of enzyme bound species (α_2) increased significantly. These parameters from 3D culture showed signs of changes towards similar direction, but the differences were not statistically significant.

An interesting change as a result of TPPBr treatment was observed for the rotational time of free NADH in cells from 3D collagen matrix. The significant increase in rotational time here indicates changes to the local environment surrounding free NADH species that are becoming more restrictive in cells from 3D culture, quite distinct from those of 2D monolayer (no statistical difference in the rotational time). The exact causes that induce such a difference are not certain, though we speculate that they might be related to the cell-matrix interactions, where integrin signaling is involved in the growth of these cells, alongside with collagen matrix remodeling. Such mechanosensing pathway has been

shown to induce cellular metabolic shifts, as well as actin polymerization that can increase the level of crowding within cellular environments (59, 62-64).

Further analyses for fractions of free (*F*) and enzyme-bound (*B*) NADH in 2D and 3D cultures were conducted to investigate the metabolic response of 4T1 cells to TPPBr treatment (Table 4.5). The TPPBr-dependent population fractions of free and enzyme-bound NADH of 4T1 cells in 2D and 3D cultures were calculated using equation 10 (Chapter 2). The 4T1 cells in 2D monolayer culture exhibit a statistical difference of the free NADH fraction (*F*) from 38% to 35% upon TPPBr treatment. At the same time, the fraction of enzyme-bound (*B*) in the 2D culture has increased from 62% to 65% ($p = 1.8 \times 10^{-17}$) upon the drug treatment. On the other hand, the fractions of free and bound NADH in 4T1 cells from 3D collagen matrix remain unchanged at 28% and exhibit no significant difference ($p = 0.89$) upon TPPBr treatment. The effects of TPPBr treatment has on the equilibrium constant (K_{eq}) of NADH binding action in both 2D and 3D cultures are quite significant, which attest to the environmental regulation of the cellular metabolic response to TPPBr. While cells in 2D monolayer experience a significant increase in the value of K_{eq}, from 1.7 to 1.9 ($p = 0.0058$), a small decrease but non-significant (from 2.7 to 2.6) is observed from cells in 3D collagen matrix ($p = 0.83$).

Table 4.5: The estimated population fractions of free (*F*) and enzyme-bound (*B*) NADH as measured for 4T1 in 2D and 3D cultures upon TPPBr treatment using time-resolved associated anisotropy. The stated standard deviations of each fraction were calculated based on the number of trials. These fractions of equilibrated populations were used to calculate the equilibrium constant (K_{eq}) and the corresponding Gibbs free energy changes ($\Delta G'$) for each culture under drug treatment.

4T1 Cultures (TPPBr Treatment)	*F* (%)	*B* (%)	K_{eq}	$\Delta G'$ (kJ/mol)
2D Monolayer ($n = 18$)	35 ± 4	65 ± 4	1.9 ± 0.3	–1.6 ± 0.4 kJ/mol
3D Collagen Matrix ($n = 22$)	28 ± 4	72 ± 4	2.6 ± 0.6	–2.3 ± 0.5 kJ/mol

The results are shown in Table 4.5 for both 2D and 3D cultures of 4T1 cells upon TPPBr treatment. The estimated overall Gibbs free energy changes (i.e., nonspecific to a given metabolic pathway of redox biochemical reaction) upon drug treatment indicates that the underlying, coupled metabolic pathways involving NADH are simultaneous in both 2D and 3D. The results also show that the equilibrium constant and the Gibbs free energy changes in 3D culture suggest a more effective response of 4T1 to TPPBr treatment in the collagen matrix. This observation can be attributed to a slower translational diffusion of TPPBr in the pores of the collagen matrix and therefore more residence time by the 4T1 cellular plasma membrane, which would enhance the uptake of the drug. Such larger uptake of the drug in 3D might explain the observed enhancement of the metabolic activities (i.e., K_{eq} and $\Delta G'$) as monitored using time-resolved associated anisotropy.

4.2.5 Statistical analysis of the associated anisotropy of NADH in 4T1 cultures as a function of MD1 treatment

To examine the environment-dependent metabolic response of 4T1 cells to MD1 (14), we carried out time-resolved fluorescence anisotropy measurements as a function on MD1 treatment in both 2D and 3D cultures. These measurements were carried out on the same day of cell cultures and two-photon time-resolved anisotropy measurements of MD1-treated and control (untreated) cells in different petri dishes.

The time-resolved associated anisotropy of MD1-treated cells in 2D monolayer is generally similar in features to those previously observed from untreated cultures (section 4.2.2) and TPPBr treated (section 4.2.3) cultures. Figure 4.5 shows representative time-resolved anisotropy of 4T1 cells in 2D (Figure 4.5A) and 3D (Figure 4.5B) cultures as a function of MD1 treatments, where the average fitting parameters are summarized in Table 4.5.

The time-resolved associated anisotropy features were observed in both MD1-treated (red curve) and control (untreated, black curve) 4T1 cells in 2D culture (Figure 4.5A), which indicate the presence of two distinct populations of free and enzyme-bound NADH at equilibrium. The fast decay component is assigned to the free NADH as compared with the slow decay component for the enzyme-bound coenzyme. The fractional amplitude of

the fast component (α_1) is on average 0.44, with an average fluorescence lifetime (τ_1) of 0.49 ± 0.04 ns. The corresponding rotational parameters of this component include an initial anisotropy (β_1) of 0.46 ± 0.03 and a rotational time (ϕ_1) of 0.17 ± 0.02 ns. Meanwhile, the slow component or enzyme bound NADH has an average population fraction (α_2) of 0.56 ± 0.03 and a fluorescence lifetime (τ_2) of 1.01 ± 0.16 ns. The initial anisotropy (β_2) of the enzyme-bound NADH is 0.41 ± 0.01 with a long rotational lifetime (ϕ_2) that is too large compared with our monitoring time that is between 0-12.5 ns.

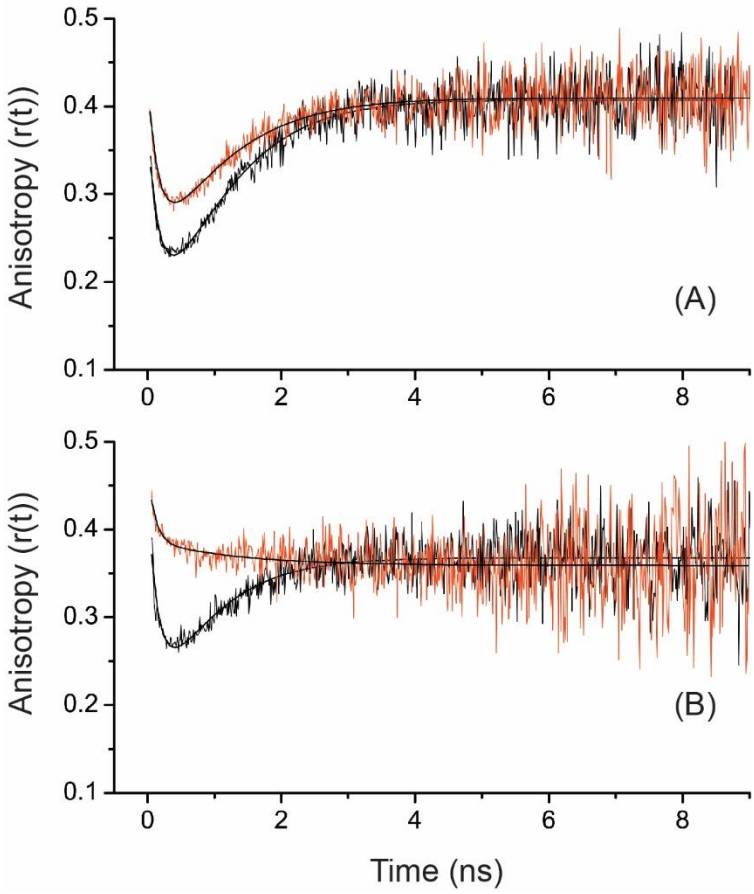

Figure 4.5: Representative time-resolved two-photon fluorescence anisotropy of intrinsic NADH in 4T1 cells in 2D and 3D cultures as a function of MD1 treatment. (A) For 2D culture, time-resolved associated anisotropy of cellular was observed in control (untreated, black curve) and MD1-treated (red curve) 4T1 cells. (B) In 3D collagen matrix, however, the observed anisotropy of cellular NADH in MD1-treated 4T1 cells decays predominantly as a double exponential (red curve) as compared with the associated anisotropy decays for the control (untreated, black curve). These representative anisotropy decays were measured on the same day of cell culture.

In order to test whether the observed difference in the fitting parameters of the time-resolved anisotropy of NADH in 4T1 cells in 2D culture is significant, we carried out statistical analysis using Student's *t*-test and the results are summarized in Figure 4.6. Our results show that all the fitting parameters (α_1, τ_1, β_1, ϕ_1, and α_2) of the time-resolved anisotropy of intrinsic NADH in control (untreated) 2D culture of 4T1 cells are significantly different from those cells treated with MD1 drug; except the rotational components (ϕ_2 and β_2) and fluorescence lifetime (τ_2) of the enzyme-bound NADH (Figure 4.6). It is also interesting to notice the amplitude fraction (α_1) of free NADH in MD1-treated 4T1 cells in 2D culture is smaller than that of the control (untreated) cells in the same culture. In contrast, the amplitude fraction (α_2) of enzyme-bound NADH in MD1-treated in 2D culture of 4T1 cells is larger than that of the control (untreated) cells.

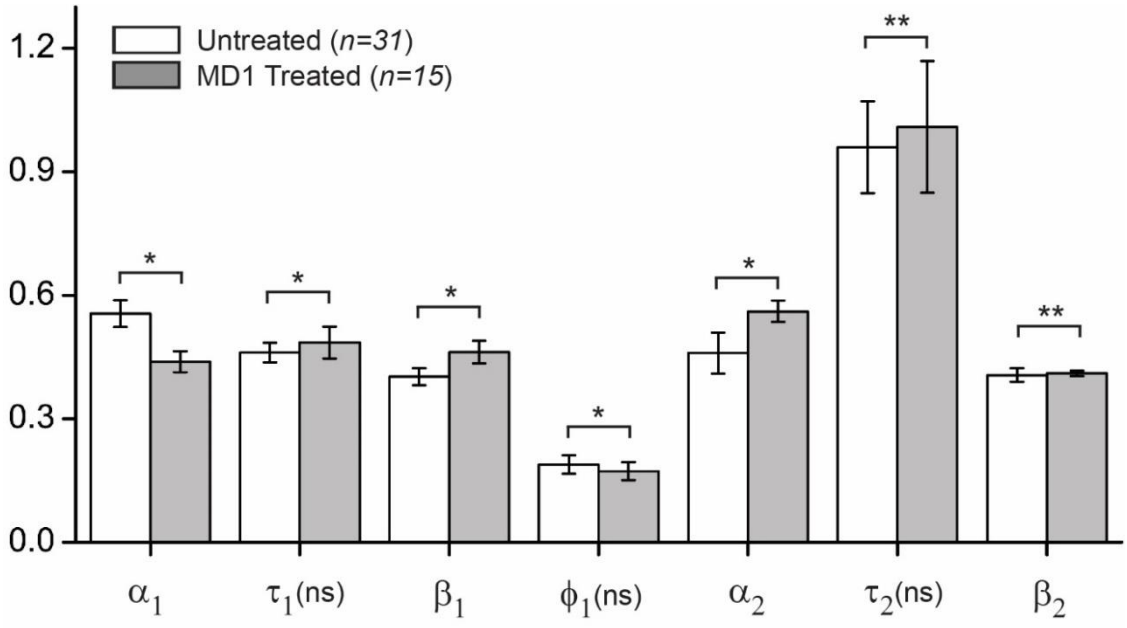

Figure 4.6: Statistical analyses of NADH anisotropy parameters from 4T1 cultures in 2D monolayer before and after MD1 treatment. The bar graphs present the average values for anisotropy parameters from each culture type, with (grey) and without treatment (white), and their standard deviations are shown here as error bars. Significant differences between two populations (with *p*-value < 0.05) are represented with one asterisk (*), while no significant difference is concluded with $p > 0.05$, and noted by two asterisks (**).

Between untreated 2D culture and MD1 treated 2D culture, significant differences were observed from parameters that describe both the free (fast component) and enzyme bound species (slow component) of intrinsic NADH. The fractional amplitude of free coenzyme (α_1) is found to be significantly lowered in 2D culture as a result of MD1 treatment ($p = 1.3 \times 10^{-15}$). However, the fluorescence lifetime of the same species (τ_1) increases significantly following drug treatment ($p = 0.036$). A significant increase is also observed in the initial anisotropy (β_1) of this fast component, with $p = 2.3 \times 10^{-10}$. In contrast, its corresponding rotational time (ϕ_1) decreases by a significant amount ($p = 0.028$). For the bound coenzyme population (slow rotating species), its fractional amplitude (α_2) increases significantly as a result of MD1 treatment ($p = 1.3 \times 10^{-15}$). The remaining two parameters that belong to this species, its fluorescence lifetime (τ_2) and its initial anisotropy (β_2) did not change by a significant amount ($p = 0.22$ and 0.26, respectively).

Table 4.6: The fitting parameters of time-resolved anisotropy of intracellular NADH in 4T1 cells in 2D monolayer and 3D collagen matrix cultures treated with MD1. The average values and standard deviation of each parameter (shown) were calculated based on the number of trials of each type of measurements. The corresponding fitting parameters of the time-resolved anisotropy of NADH in control (untreated) 4T1 cells in 2D and 3D cultures are summarized in Table 4.2 (Section 4.2.3).

4T1 Cell **2D** Culture	α_1	τ_1 (ns)	β_1	ϕ_1 (ns)	α_2	τ_2 (ns)	β_2	ϕ_2* (ns)
MD1-Treated (n = 15)	0.44 ± 0.03	0.49 ± 0.04	0.46 ± 0.03	0.17 ± 0.02	0.56 ± 0.03	1.01 ± 0.16	0.41 ± 0.01	∞
4T1 Cell **3D** Culture	--	--	β_1	φ_1 (ns)	β_2	φ_2 (ns)	β_3	φ_3 (ns)
MD1-Treated (n = 19)	--	--	0.20 ± 0.16	0.05 ± 0.04	0.07 ± 0.03	1.95 ± 2.06	0.34 ± 0.04	∞

* The rotational time of the enzyme-bound species is too slow compared with the excited-state lifetime (~ 100-10^{20} ns) and therefore its corresponding slow anisotropy component does not decay significantly during the detection window of 0–12.5 ns.

In contrast with 2D culture, the corresponding time-resolved anisotropy of cellular NADH in 3D culture of MD1-treated cells decays predominantly as double-exponential decay. However, a minor third decays component (β_2 and ϕ_2) enhanced the fitting χ^2 and residual as indicative of the goodness of the fitting model (Table 4.5). This trend was observed consistently throughout all MD1-treated 3D cultures from which time-resolved anisotropy were measured. The triple exponential decay of the observed time-resolved anisotropy was fitted using equation 6 (Chapter 2). The observed trend for the MD1-treated cells in 3D culture was consistent among the stated number of trials (Table 4.5)

The dominant fast and slow components in the observed triexponential decay of MD1-treated 4T1 cells in 3D culture are attributed to two predominant populations of free and enzyme-bound NADH at equilibrium. The free NADH population exhibits the most rapid rotational time with an average initial anisotropy (β_1) of 0.19 ± 0.16 and a rotational time (ϕ_1) of 0.05 ± 0.04 ns. The enzyme-bound NADH exhibits the slowest rotational time ($\phi_3 \sim \infty$ ns) due to its size, and perhaps a restrictive local environment, with an initial anisotropy value (β_3) of 0.34 ± 0.04. We argue that fast- and slow-rotational component of the associated and double-exponential anisotropy decays are basically assigned to the same two predominant species on intracellular NADH (i.e., free and enzyme-bound). It is worth mentioning that, a minor (β_2 = 0.07, which is ~11% of the maximum initial anisotropy) third decay component enhanced the fitting χ^2 and residual. Such minor component is attributed to a third population that is distinct from both the free and enzyme-bound NADH based on the rotational time (β_2 = 1.95 ± 2.06 ns).

Due to the observed differences in time-resolved anisotropy of NADH of 4T1 cells in 3D culture, it is quite difficult to directly compare the responses between the two treated culture types (2D and 3D) using their anisotropy parameters. Nevertheless, we relied on simulations as an attempt to understand the underlying origin for the observed changes in the time-resolved anisotropy of intracellular NADH in 3D culture of 4T1 cells as a function of MD1 treatment. A major difference between associated anisotropy and double exponential anisotropy of free and enzyme-bound NADH in a mixture is the large difference in the significant differences in both the fluorescence lifetime and the hydrodynamic volume (or rotational time) of both species (33, 42).

It has also been observed from our previous simulations (Figure 4.1C) that when the difference between the two fluorescence lifetimes (τ_1 and τ_2) is slowly reduced with increasing value of τ_1, or decreasing value of τ_2, the time-resolved anisotropy of NADH species in the mixture slowly changes from associated to exponential anisotropy decays. Similarly, decrease in the parameter β_2 also leads to this change in anisotropy decay (Figure 4.1F). The value of the rotational time ϕ_2, when decreased to a similar magnitude to what of ϕ_1, can also induce a change from associated anisotropy to a tri- or bi-exponential decay (Figure 4.1G).

The appearances of our simulation curves can be compared to the sample decays from Figure 4.5B to infer the potential parameter changes that lead to such exponential decay observed from MD1 treated cells in 3D culture. The possible parameter changes that could be responsible for this overall decay shift are increasing τ_1 (or decreasing τ_2), decreasing β_2, as well as decreasing ϕ_2. It is interesting to note that in the case of decreasing β_2, the starting point of the decay curve drops to a lower value, together with the bottom of the curve (at approximately 0.05 when $\beta_2 = 0.05$) as it flattens out. Meanwhile, when ϕ_2 is decreased alone, the starting point remains the same, but the bottom of the curve also drops (near r(t) = 0) as it shifts to an exponential decay. In the actual anisotropy decay from treated 4T1 cells in 3D, not only the bottom of the curve is higher (around 0.35), but the starting point of the decay is also relatively high. Due to these reasons, it is not likely that parameter β_2 is responsible for the exponential shift. Parameter ϕ_2, on the other hand, might be responsible for introducing the second exponential component, but the differences are not solely due to its change.

In addition, when the value of τ_1 approaches that of τ_2 and vice versa, the associated anisotropy decay also gradually shifts towards an exponential-decay trend, while the bottom of the curve still lays relatively high (around 0.2). However, the shift also carries with it an increase in the magnitude of the fast decay (between 0-0.5 ns), which is not observed in our experimental result (Figure 4.5B). This decay is quite short from our anisotropy measurement compared to what displayed in Figure 4.1C, suggesting that there might be another factor that plays a role in decreasing this initial anisotropy decay. From

our simulation data, the parameter that is most likely responsible for this would be the fractional amplitude of the free species, or α_1. To confirm this, an additional simulation was carried out for the case when the two fluorescence lifetimes are equivalent ($\tau_1 = \tau_2$), while α_1 changes (Figure 4.7).

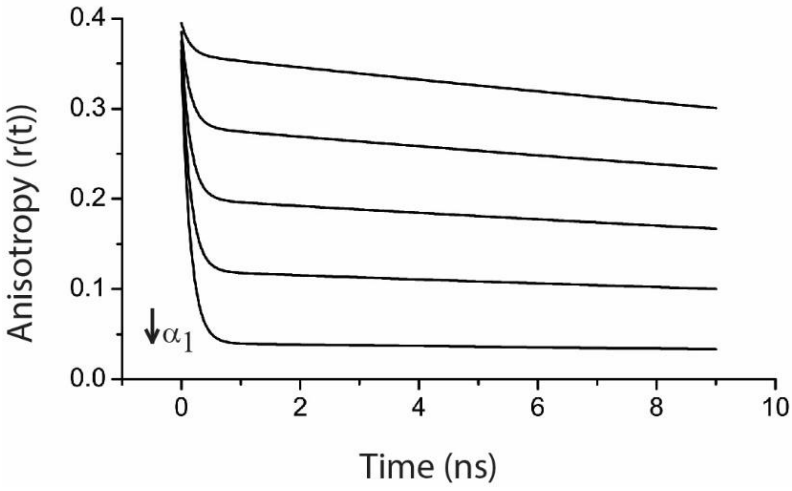

Figure 4.7: Simulation of time-resolved anisotropy of NADH species in a mixture when the fluorescence lifetimes of both species (τ_1 and τ_2) are close in values. As the amplitude fraction (α_1) increases, the amplitude fraction of the enzyme-bound NADH decreases, which results in the shown changes in the overall shape of the anisotropy decay.

In summary, by comparing our simulation curves to observed experimental time-resolved anisotropy of NADH mixture in 3D culture of MD1-treated 4T1 cells, there are a few possible parameters that could be responsible for the shift from associated anisotropy decay to triexponential decay as observed in MD1 treated cells from 3D culture. Large changes to either value of τ_1 or τ_2 are believed to contribute to the overall shape shift of the anisotropy decay. The second rotational component being added is likely a result of changes to the rotational time of the enzyme bound species. Lastly, decrease in the value of α_1 decreases the initial anisotropy decay and potentially contributes to the resulting shape of the curve that we observed. With the treatment of MD1, the fraction of free NADH in cells from 2D monolayer

Calculations were also carried out to find the population fractions of free NADH (*F*) and enzyme bound NADH (*B*) in treated cells from both culture types (2D and 3D). Since the fitting parameters for the triexponential anisotropy decay of cells in 3D collagen matrix are different from the associated anisotropy decay that has been discussed up until now, a different set of equations were used to calculate the free (*F*) and bound (*F*) fractions of NADH from this culture. The initial anisotropy reported as β_i in our fitting equation consists of the overall initial anisotropy (r_0) multiplied by the fraction of the species being described. Therefore, the ratio of each initial anisotropy to the total sum of all initial anisotropy values from the fitting equation can reflect the fraction of the species. Based on the rotational time of the three species, it is likely that the first or fastest rotating species describes the population of free coenzyme while the slowest rotating species shows the behavior of bound NADH within 4T1 cellular environment.

Table 4.7: Average fractions of free NADH (*F*) and enzyme bound NADH (*B*) with their standard deviations as calculated from anisotropy parameters of MD1 treated 4T1 from both culture types. The values for K_{eq} and $\Delta G'$ are also calculated and reported together with its standard deviation.

4T1 Cell Cultures	*F* (%)	*B* (%)	K_{eq}	$\Delta G'$ (kJ/mol)
2D – MD1 (*n* = 15)	28 ± 2	72 ± 2	2.6 ± 0.2	-2.4 ± 0.2
3D – MD1 (*n* = 12)	30 ± 14	59 ± 14	2.6 ± 1.5	-1.9 ± 1.7

From our calculations, 4T1 cells in 2D monolayer seem to have a mixture of intracellular NADH that is made up of approximately 28% of free coenzyme (*F*) and 72% of enzyme bound species (*F*). In contrast, the population fractions of free and bound fluorophore in 3D culture are 30% and 59%, respectively. It is important to note that these two fractions do not sum up to 100% due to the existence of the second species, which is not attributed to either free or bound population of NADH. Statistical comparisons were made to compare the value of each fraction between the two culture types, as well as cells before and after

treatment in each culture. With the treatment of MD1, the fraction of free NADH from 4T1 cells in 2D monolayer decreased significantly ($p = 1.8 \times 10^{-19}$). The fraction of bound NADH from this culture, in return, increased significantly with the treatment of MD1 ($p = 1.8 \times 10^{-19}$). In contrast, the fraction of free NADH from cells in 3D collagen matrix did not change by a significant amount after MD1 treatment ($p = 0.68$) while the bound population fraction (B) decreased significantly ($p = 0.0011$). Between treated 2D and 3D cultures, no statistical difference was found in the free NADH fraction (F, $p = 0.53$) but the bound fraction from treated 3D culture was significantly less than that of treated 2D culture ($p = 0.00065$).

Further calculations using free and bound fractions (Equation 4.1, Section 4.2.2) found an estimated equilibrium constant for NADH enzyme binding across our sample of about 2.6 ± 0.2 for 2D monolayer and 2.6 ± 1.5 for 3D collagen matrix. These values are not statistically different between the two treated culture types. However, our statistical analyses show that, upon MD1 treatment, the equilibrium constant of 4T1 cells in 2D culture increased significantly (from 1.7 to 2.6, $p = 1.1 \times 10^{-10}$). Meanwhile, this value did not change by significant amount for cells from 3D culture ($p = 0.83$). The resulting changes in Gibbs free energy for 2D and 3D culture were found to be -2.4 ± 0.2 kJ/mol and -1.9 ± 1.7 kJ/mol, respectively. Even though they are not statistically different between treated cultures ($p = 0.20$), the change in Gibbs free energy of 4T1 cells in 2D culture after MD1 treatment undergoes a significant decrease (-1.3 kJ/mol to -2.6 kJ/mol, $p = 1.4 \times 10^{-16}$) while increasing in 3D culture but not statistically significant (-2.4 to -1.9 kJ/mol, $p = 0.25$).

As an MCTs inhibitor, MD1 is expected to inhibit both glycolysis and oxidative phosphorylation, resulting in a mixed response from our cell cultures. From our 2P-FLIM results, cells from 2D monolayer appear to undergo a slight oxidative shift as a result of MD1 treatment, while cells from 3D collagen matrix express an opposite metabolic shift towards glycolysis. This seem to be in an agreement with our experimental anisotropy data, where a shift towards more enzyme bound NADH is found from 2D cells (increase in K_{eq}). In contrast, the value for K_{eq} from our 3D culture did not change significantly, which might indicate the mixed responses expected from the effect of MD1. The significantly lowered

in Gibbs free energy from 2D culture of 4T1 is quite unexpected, but it might also be suggestive that cells in 2D culture is not capable of adjusting to the impact of drug treatment quite as well as 3D culture (mostly unchanged for both drugs). These observations overall are in well agreement with our previous conclusion regarding the more dynamic response of 3D cultures upon drug treatments in contrast to the conventional 2D monolayer.

4.3 Conclusions

To complement our findings from 2P-FLIM, we carried out time-resolved fluorescence polarization anisotropy measurements for intracellular NADH in 2D monolayer and *in vivo*-like 3D collagen matrix cultures of 4T1 cells as a control. This technique exploits the inherent rotational dynamics differences in both the fluorescence lifetime (quantum yield) and hydrodynamic radius (size) of free and enzyme-bound NADH. Overall, our anisotropy measurements show that metastatic breast cancer cell line 4T1 in 2D culture is generally more glycolytic than their 3D counterpart. This is supported by statistical differences between anisotropy decay parameters from free and bound coenzyme populations between the two cultures, together with the calculated fractions of free NADH and enzyme bound NADH. Assuming a black-box model for the cells where two populations of free and enzyme-bound NADH exist at equilibrium, we estimated an overall equilibrium constant and Gibbs free energy of 1.7 ± 0.2, and -1.3 ± 0.3 kJ/mol in 2D culture of control 4T1, respectively, as compared with 2.7 ± 0.7, and -2.4 ± 0.6 kJ/mol in 3D collagen culture.

We also used time-resolved anisotropy approach to examine the environmental regulation of the cellular response and changes in the metabolic activities upon MD1 and TPPBr treatments. The 4T1 cells cultured in 2D monolayer and 3D collagen matrix display quite contrasting metabolic responses to TPPBr and MD1 treatments. Our statistical analyses of anisotropy fitting parameters as well as the corresponding population fractions, equilibrium constant, and the changes in Gibbs free energy suggest that the changes in the metabolic activities of 4T1 cells in 3D culture is more responsive to drug treatment than the conventional 2D counterpart. This conclusion is based on the sensitivity of the estimated

overall equilibrium constant and the changes in the Gibbs free energy in 4T1 cells to drug treatments as a function of 2D and 3D cultures.

In contrast to 2P-FLIM (Chapter 3), time-resolved 2P-fluorescence polarization anisotropy measurements provide real-time rotational dynamics of free and enzyme-bound NADH with high temporal resolution. These rotational motions are in direct relation to environmental factors surrounding the fluorophores, including macromolecular crowding and viscosity. Because of this, changes in fluorescent characteristics of fluorophores due to metabolic-directed changes in their local environments can be studied.

However, this approach under two-photon excitation is based on ensemble averaging over a few cells in the field of view as a means to avoid cell photodamage if the femtosecond laser pulses were to be parked on a given cell to acquire an anisotropy decay. Therefore, this approach lacks the high spatial resolution required for intracellular (pixel-to-pixel) and intercellular (cell-to-cell) as in 2P-FLIM. Interestingly, however, the observed metabolic response of 4T1 to environments (2D versus 3D cultures) and drug (that 3D cultureMD1 and TPPBr) treatments using time-resolved anisotropy approach are very similar to those reported in Chapter 3 using 2P-FLIM.

With the recent advances of time-correlated single photon counting modules, associated electronics, photomultiplier tubes with high quantum efficiency, it is feasible to acquire time-resolved anisotropy decay per pixel using two-channel detection of the parallel and perpendicular fluorescence.

Detailed comparisons between the two techniques are of interest towards the most convenient diagnostic tool for monitoring metabolic changes in living cells under environmental, chemical, and diseased conditions. This will be further discussed in the following chapter 5.

Chapter V:

Overall conclusions and future directions

We have investigated the cellular metabolic activities of a metastatic murine breast cancer cell line (4T1) grown in two different culture types, a conventional 2D monolayer and 3D collagen matrix, using intrinsic NADH autofluorescence as a natural biomarker. In doing so, we used two complementary, quantitative, and noninvasive techniques on living cells: 2P-FLIM and 2P-time resolved fluorescence polarization anisotropy. The laser-scanning 2P-FLIM approach exploits the sensitivity of the excited-state fluorescence lifetime of NADH to enzyme binding and provides high spatial resolution, but with relatively low temporal, signal-to-noise fluorescence decay per pixel. In contrast, the laser-scanning time-resolved 2P-anisotropy approach uses the difference rotational dynamics of free and enzyme-bound NADH due to their distinct molecular weights. However, the time-resolved anisotropy approach provides an ensemble average information on a number of living cells in the field of microscopic view at high temporal resolution and high signal-to-noise ratio of the observed anisotropy decays.

Our overall results indicate that 4T1 cells in the control 3D culture (untreated) appear to have a metabolic state that is more oxidative while the same cell line grown as 2D monolayer is more glycolytic. This is supported by our analyses of NADH fluorescence lifetime distributions from both culture types, as well as statistical analyses of fittings parameters from both 2P-FLIM and fluorescence anisotropy. These shifts are driven by, not only the fluorescence lifetime of enzyme bound population of NADH as suggested by 2P-FLIM, but also the population fractions of free and enzyme bound species based on our anisotropy measurements.

With the treatment of two different metabolic disrupting drugs, MD1 and TPPBr, differences in metabolic responses between the two culture types are also observed using our complementary approaches. The metabolic shifts of the two cultures (2D monolayer and 3D collagen matrix) after each drug treatment are significantly different, and indeed quite opposite of each other. For example, the observed changes in the metabolic activities

of 4T1 cells in 3D collagen matrix seems to trigger a metabolic response that is consistent with the hypothesized working mechanism of these metabolic drugs; in contrast with the 2D monolayer culture. These results overall may suggest that 3D collagen matrix, compared to the conventional 2D monolayer, is a better and more effective tissue- and tumor-like models for drugs screening due to a higher sensitivity in cellular responses that are likely environmentally induced.

In addition, our proposed black-box model of the living 4T1 cells enables us to calculate approximate values of equilibrium constant (K_{eq}) and the change in Gibbs free energy ($\Delta G'$) towards interesting insights into the underlying metabolic activities associated with NADH as a biomarker. For example, the equilibrium constant values are generally higher in 3D cell culture compared to the 2D counterpart, especially with untreated cultures, providing another supporting evidence that the metabolic state of 4T1 cells in 3D collagen matrix is likely more oxidative. Furthermore, the change in Gibbs free energy is found to be generally higher in magnitude in 3D cell culture compared to 2D, which may indicate the higher metabolic activities within cells that are grown in 3D collagen matrix. This value, for 2D cell cultures as a result of drug treatments, undergo larger fluctuations compared to that of 3D cell cultures. This observation may also suggest that the metabolic state of cells in 2D monolayer culture does not adjust to these treatments as quickly or as well as cells in 3D collagen matrix culture.

The two fluorescence techniques employed in these studies have their distinct advantages and disadvantages, but yet provide us with complementary results supporting our overall conclusions concerning the cellular metabolic states of 4T1 cells in 2D and 3D cultures. For example, we compare the calculated intracellular NADH binding equilibrium constants and the change in Gibbs free energy obtained from the 2P-FLIM (Chapter 3) and time-resolved 2P-anisotropy (Chapter 4) as summarized in Table 5.1 below.

Table 5.1: Summary of equilibrium constant values and changes in Gibbs free energy from each culture type and treatment, as calculated from the fractions of free and enzyme bound NADH using 2P-FLIM and time-resolved fluorescence anisotropy. The average and standard deviation for each value is calculated over numbers of trials (previously reported in Chapter 3 and 4).

4T1 Cultures	2P-FLIM		Anisotropy	
	K_{eq}	$\Delta G'$ (kJ/mol)	K_{eq}	$\Delta G'$ (kJ/mol)
2D: Untreated	1.4 ± 0.2	– 0.8 ± 0.3	1.7 ± 0.2	– 1.3 ± 0.3
3D: Untreated	1.5 ± 0.1	– 1.0 ± 0.2	2.7 ± 0.7	– 2.4 ± 0.6
2D: TPPBr Treated	1.4 ± 0.2	– 0.8 ± 0.3	1.9 ± 0.3	– 1.6 ± 0.4
3D: TPPBr Treated	1.3 ± 0.2	– 0.7 ± 0.3	2.6 ± 0.6	– 2.3 ± 0.5
2D: MD1 Treated	1.6 ± 0.2	– 1.1 ± 0.4	2.6 ± 0.2	– 2.4 ± 0.2
3D: MD1 Treated	1.5 ± 0.2	– 1.0 ± 0.2	2.6 ± 1.5	– 1.9 ± 1.7

From 2P-FLIM results, the equilibrium constants for different 4T1 cultures with different treatments slightly varied, but stayed within a small range (1.3 – 1.6). The differences between these values, though are small, they still reflect the trends that we previously observed from comparing 2P-FLIM parameters side by side (Chapter 3). For example, between untreated 2D and 3D cultures of 4T1, the equilibrium constant is significantly different (p = 0.0029) with a higher value from 3D culture compared to that of 2D (higher bound NADH fraction). Similarly, TPPBr treated 3D culture has a significantly lowered value of K_{eq} compared to 2D culture (p = 0.00041) which indicates an apparent shift towards glycolysis due to the impact of the OXPHOS inhibiting drug. The last statistical difference is observed between MD1 treated 2D culture of 4T1 and untreated 2D culture, where K_{eq} increases with the treatment of MD1 (p = 0.0029). The same significant

differences are also concluded for values of Gibbs free energy change calculated from 2P-FLIM parameters.

In contrast, time-resolved 2P-anisotropy measurements yield pronounced difference in metabolic states as reflected by estimated equilibrium constant values between untreated 2D and 3D cultures of 4T1 are of a much larger magnitude (1.7 and 2.7, respectively, $p = 1.1 \times 10^{-10}$). The same statistical differences that are observed from 2P-FLIM are also reported from anisotropy results, but with values that are much more distinct. For example, 2D culture of MD1-treated 4T1 cells has an equilibrium constant ranging from 1.7 to 2.6, while value of $\Delta G'$ decreases from – 1.3 kJ/mol to – 2.4 kJ/mol, and both are statistically different ($p = 1.1 \times 10^{-18}$ and 1.1×10^{-16}, respectively). In comparison, these differences are rather subtle from 2P-FLIM results, with an increase in K_{eq} value of 0.2 (1.4 to 1.6, $p = 0.0029$) and also a small decrease in $\Delta G'$ by 0.3 kJ/mol (– 0.8 to – 1.1 kJ/mol, $p = 0.0035$).

Figure 5.1 shows side by side comparisons of the equilibrium constant and the change in the Gibbs free energy of the cell ensample as estimated using 2P-FLIM and time-resolved anisotropy. The results indicate significant differences in almost all calculated values of K_{eq} and $\Delta G'$ using these complementary techniques. One exception from this is the change in Gibbs free energy from MD1 treated 3D culture of 4T1 ($p = 0.056$). Differences between values calculated from 2P-FLIM parameters (white bars) are subtle in contrast with that from anisotropy (grey bars), which yield a larger dynamic range and pronounced difference in the estimate thermodynamic quantities. However, the most important thing to note, is that our conclusions regarding cellular metabolic behaviors as observed from 2P-FLIM are supported and further supplemented by findings from fluorescence anisotropy.

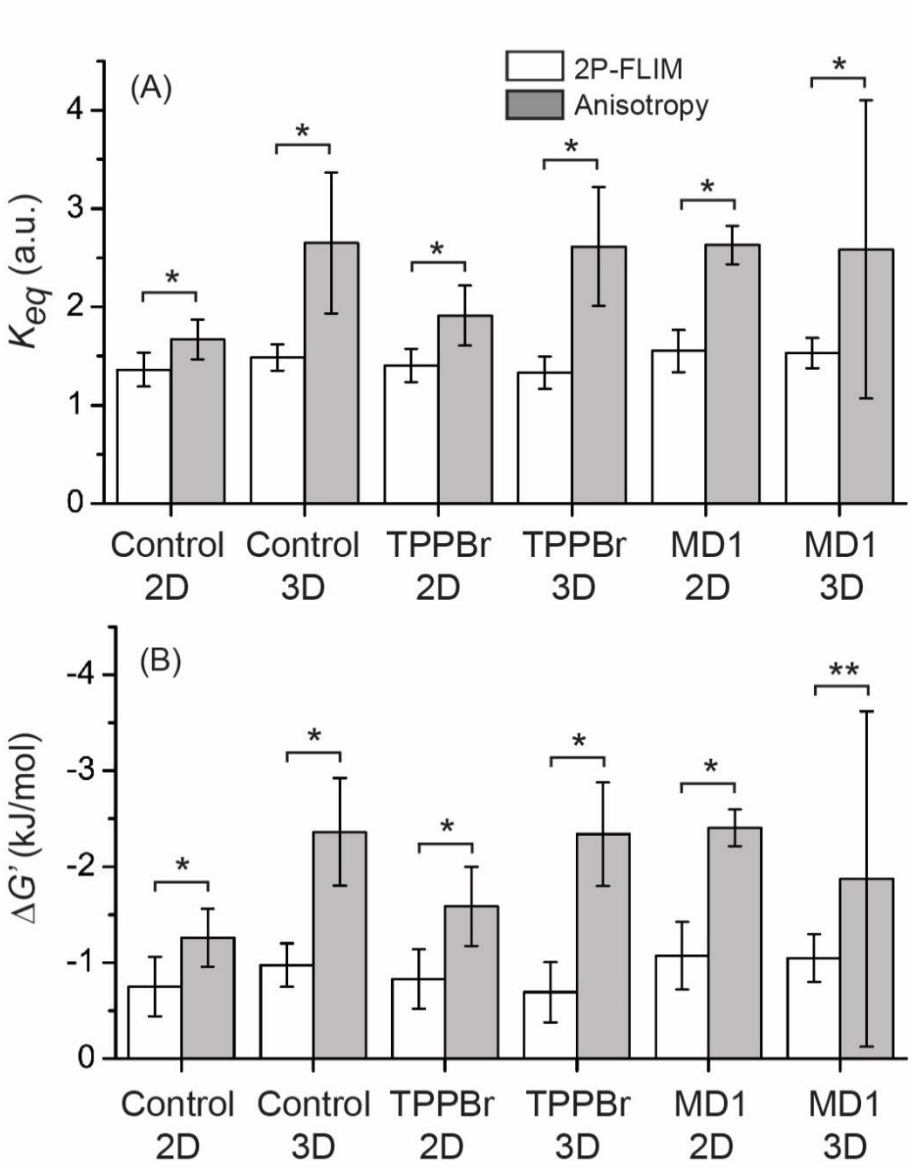

Figure 5.1: Statistical comparisons between results collected using the two techniques, 2P-FLIM (white) and time-resolved fluorescence anisotropy (grey) to study metabolic states of 4T1 cultures. Values of (A) NADH binding equilibrium constants over cell populations and (B) calculated changes in Gibbs free energy are used for these comparisons. The average values are presented here as bars, with their standard deviations as error bars. Significant difference ($p < 0.05$) is shown with one asterisk (*), while $p > 0.05$ indicating no significant difference is noted with two asterisks (**).

Moving forward, we plan to use these same experimental approaches to exploit another intracellular coenzyme, namely flavin adenine dinucleotide (FAD), as another intrinsic metabolic biomarker. This will be useful for monitoring the oxidative phosphorylation and the redox biochemical reactions of 4T1 cells in 2D and 3D cultures as a function of drug treatment. The same experimental settings can be applied to study a nonmetastatic breast cancer cell line (67NR) to observe their metabolic behaviors in comparison to that of the metastatic 4T1. In addition, we are planning to examine co-cultures of different cell sub-clones (+/- stromal cells) to examine potential metabolic couplings within heterogeneous tumors. Another topic that is within our interests involves investigation of stromal changes and their impact on tumor cell metabolic plasticity. Through this experiment, we hope to be able to draw connections between matrix properties, for example, matrix stiffening in relation to diabetes, to cellular metabolic activities.

Bibliography

1. Greenlee, R. T., T. Murray, S. Bolden, and P. A. Wingo. 2000. Cancer statistics, 2000. CA: A Cancer Journal for Clinicians 50:7-33.
2. Siegel, R. L., K. D. Miller, and A. Jemal. 2019. Cancer statistics, 2019. CA: A Cancer Journal for Clinicians 69:7-34.
3. Dexter, D. L., H. M. Kowalski, B. A. Blazar, Z. Fligiel, R. Vogel, and G. H. Heppner. 1978. Heterogeneity of Tumor Cells from a Single Mouse Mammary Tumor. Cancer Research 38:3174-3181.
4. Singh, A. K., R. K. Arya, S. Maheshwari, A. Singh, S. Meena, P. Pandey, O. Dormond, and D. Datta. 2015. Tumor heterogeneity and cancer stem cell paradigm: Updates in concept, controversies and clinical relevance. International Journal of Cancer 136:1991-2000.
5. Dagogo-Jack, I., and A. T. Shaw. 2017. Tumour heterogeneity and resistance to cancer therapies. Nature Reviews Clinical Oncology 15:81. Review Article.
6. Simões, R. V., I. S. Serganova, N. Kruchevsky, A. Leftin, A. A. Shestov, H. T. Thaler, G. Sukenick, J. W. Locasale, R. G. Blasberg, J. A. Koutcher, and E. Ackerstaff. 2015. Metabolic Plasticity of Metastatic Breast Cancer Cells: Adaptation to Changes in the Microenvironment. Neoplasia 7(8):671-684. Research Paper.
7. Tilghman, R. W., E. M. Blais, C. R. Cowan, N. E. Sherman, P. R. Grigera, E. D. Jeffery, J. W. Fox, B. R. Blackman, D. J. Tschumperlin, J. A. Papin, and J. T. Parsons. 2012. Matrix Rigidity Regulates Cancer Cell Growth by Modulating Cellular Metabolism and Protein Synthesis. Plos One 7:e37231.
8. Jia, D., J. H. Park, K. H. Jung, H. Levine, and B. A. Kaipparettu. 2018. Elucidating the Metabolic Plasticity of Cancer: Mitochondrial Reprogramming and Hybrid Metabolic States. Cells 7:21.
9. Meacham, C. E., and S. J. Morrison. 2013. Tumour heterogeneity and cancer cell plasticity. Nature 501:328-337.
10. Warburg, O. 1956. On the Origin of Cancer Cells. Science 123:5.
11. Vincent, A. S., T. T. Phan, A. Mukhopadhyay, H. Y. Lim, B. Halliwell, and K. P. Wong. 2008. Human Skin Keloid Fibroblasts Display Bioenergetics of Cancer Cells. Journal of Investigative Dermatology 128:702-709.
12. Vazquez-Martin, A., B. Corominas-Faja, S. Cufi, L. Vellon, C. Oliveras-Ferraros, O. J. Menendez, J. Joven, R. Lupu, and J. A. Menendez. 2013. The mitochondrial H(+)-ATP synthase and the lipogenic switch: new core components of metabolic reprogramming in induced pluripotent stem (iPS) cells. Cell Cycle 12:207-218.
13. Pavlides, S., D. Whitaker-Menezes, R. Castello-Cros, N. Flomenberg, A. K. Witkiewicz, P. G. Frank, M. C. Casimiro, C. Wang, P. Fortina, S. Addya, R. G. Pestell, U. E. Martinez-Outschoorn, F. Sotgia, and M. P. Lisanti. 2009. The Reverse Warburg Effect: Aerobic Glycolysis in Cancer Associated Fibroblasts and the Tumor Stroma. Cell Cycle 8:18.
14. Sonveaux, P., T. Copetti, C. J. De Saedeleer, F. d. r. Ve´gran, J. Verrax, K. M. Kennedy, E. J. Moon, S. Dhup, P. Danhier, F. o. Fre´rart, B. Gallez, A. Ribeiro, C. Michiels, M. W. Dewhirst, and O. Feron. 2012. Targeting the Lactate

Transporter MCT1 in Endothelial Cells Inhibits Lactate-Induced HIF-1 Activation and Tumor Angiogenesis. Plos One 7:1-13.
15. Vegran, F., R. Boidot, C. Michiels, P. Sonveaux, and O. Feron. 2011. Lactate Influx through the Endothelial Cell Monocarboxylate Transporter MCT1 Supports an NF-kB/IL-8 Pathway that Drives Tumor Angiogenesis. Cancer Res 71:2550-2560.
16. Heppner, G. H., and B. E. Miller. 1983. Tumor heterogeneity: biological implications and therapeutic consequences. Cancer and Metastasis Reviews 2:5-23.
17. Miller, B. E., F. R. Miller, D. J. Wilburn, and G. H. Heppner. 1987. Analysis of tumour cell composition in tumours composed of paired mixtures of mammary tumour cell lines. British Journal of Cancer 56:561-569.
18. Fidler, I. J., and I. R. Hart. 1982. Biological Diversity in Metastatic Neoplasms: Origins and Implications. Science 217:998-1003.
19. Conklin, M. W., and P. J. Keely. 2012. Why the stroma matters in breast cancer: insights into breast cancer patient outcomes through the examination of stromal biomarkers. Cell Adh Migr 6:249-260.
20. Riching, K. M., B. L. Cox, M. R. Salick, C. Pehlke, A. S. Riching, S. M. Ponik, B. R. Bass, W. C. Crone, Y. Jiang, A. M. Weaver, K. W. Eliceiri, and P. J. Keely. 2014. 3D collagen alignment limits protrusions to enhance breast cancer cell persistence. Biophysical journal 107:2546-2558.
21. Cross, V. L., Y. Zheng, N. Won Choi, S. S. Verbridge, B. A. Sutermaster, L. J. Bonassar, C. Fischbach, and A. D. Stroock. 2010. Dense type I collagen matrices that support cellular remodeling and microfabrication for studies of tumor angiogenesis and vasculogenesis in vitro. Biomaterials 31:8596-8607.
22. Morris, B. A., B. Burkel, S. M. Ponik, J. Fan, J. S. Condeelis, J. A. Aguire-Ghiso, J. Castracane, J. M. Denu, and P. J. Keely. 2016. Collagen Matrix Density Drives the Metabolic Shift in Breast Cancer Cells. EBioMedicine 13:146-156. Research paper.
23. Carey, S. P., K. E. Martin, and C. A. Reinhart-King. 2017. Three-dimensional collagen matrix induces a mechanosensitive invasive epithelial phenotype. Scientific Reports 7. Article.
24. Birgersdotter, A., R. Sandberg, and I. Ernberg. 2005. Gene expression perturbation in vitro—A growing case for three-dimensional (3D) culture systems. Seminars in Cancer Biology 15:405-412.
25. Charoen, K. M., B. Fallica, Y. L. Colson, M. H. Zaman, and M. W. Grinstaff. 2014. Embedded multicellular spheroids as a biomimetic 3D cancer model for evaluating drug and drug-device combinations. Biomaterials 35:2264-2271.
26. Huang, Y.-J., and S.-h. Hsu. 2014. Acquisition of epithelial–mesenchymal transition and cancer stem-like phenotypes within chitosan-hyaluronan membrane-derived 3D tumor spheroids. Biomaterials 35:10070-10079.
27. Jang, M., I. Koh, S. J. Lee, J.-H. Cheong, and P. Kim. 2017. Droplet-based microtumor model to assess cell-ECM interactions and drug resistance of gastric cancer cells. Scientific reports 7:41541.

28. Sung, K. E., X. Su, E. Berthier, C. Pehlke, A. Friedl, and D. J. Beebe. 2013. Understanding the impact of 2D and 3D fibroblast cultures on in vitro breast cancer models. PloS one 8:e76373-e76373.
29. Reynolds, D. S., K. M. Tevis, W. A. Blessing, Y. L. Colson, M. H. Zaman, and M. W. Grinstaff. 2017. Breast Cancer Spheroids Reveal a Differential Cancer Stem Cell Response to Chemotherapeutic Treatment. Scientific Reports 7:10382.
30. Miller, B. E., D. McInerney, D. Jackson, and F. R. Miller. 1986. Metabolic Cooperation between Mouse Mammary Tumor Subpopulations in Three-Dimensional Collagen Gel Cultures. Cancer Research 46:89-93.
31. Flynn, D., J. Yang, and S. Nandi. 1982. Growth and Differentiation of Primary Cultures of Mouse Mammary Epithelium Embedded in Collagen Gel. Differentiation 22:191-194.
32. Berg, J. M., J. L. Tymoczko, J. L. Gatto, Jr, and L. Stryer. 2015. Biochemistry. W. H. Freeman.
33. Ghukasyan, V. V., and A. A. Heikal. 2014. Natural Biomarkers for Cellular Metabolism: Biology, Techniques, and Applications. CRC Press.
34. San-Millán, I., and G. A. Brooks. 2016. Reexamining cancer metabolism: lactate production for carcinogenesis could be the purpose and explanation of the Warburg Effect. Carcinogenesis 38:119-133.
35. Hirschhaeuser, F., U. G. A. Sattler, and W. Mueller-Klieser. 2011. Lactate: A Metabolic Key Player in Cancer. Cancer Research 71:6921.
36. Heikal, A. A. 2010. Intracellular coenzymes as natural biomarkers for metabolic activities and mitochondrial anomalies. Biomarkers in Medicine 4:241-263. Review.
37. Chance, B. 2004. Mitochondrial NADH Redox State, Monitoring Discovery and Deployment in Tissue. Methods in Enzymology. Academic Press, pp. 361-370.
38. Chance, B., P. Cohen, F. Jobsis, and B. Schoener. 1962. Intracellular Oxidation-Reduction States in Vivo. Science 137:499-508.
39. Chance, B., V. Legallais, and B. Schoener. 1962. Metabolically Linked Changes in Fluorescence Emission Spectra of Cortex of Rat Brain, Kidney and Adrenal Gland. Nature 195:1073-1075.
40. Barlow, C. H., and B. Chance. 1976. Ischemic Areas in Perfused Rat Hearts: Measurement by NADH Fluorescence Photography. Science 193:909-910.
41. Chance, B. 1991. Optical Method. Annual Review of Biophysics and Biophysical Chemistry 20:1-30.
42. Lakowicz, J. R. 2006. Principles of fluorescence spectroscopy. Springer, New York.
43. Xu, C., and W. W. Webb. 1996. Measurement of two-photon excitation cross sections of molecular fluorophores with data from 690 to 1050 nm. J. Opt. Soc. Am. B 13:481-491.
44. Vishwasrao, H. D., A. A. Heikal, K. A. Kasischke, and W. W. Webb. 2005. Conformational dependence of intracellular NADH on metabolic revealed by associated fluorescence anisotropy. The Journal of Biological Chemistry 280:25119-25126.

45. Yu, Q., and A. A. Heikal. 2009. Two-photon autofluorescence dynamics imaging reveals sensitivity of intracellular NADH concentration and conformation to cell physiology at the single-cell level. J. Photochem. Photobiol. B 95:46-57.
46. Huang, S., A. A. Heikal, and W. W. Webb. 2002. Two-photon fluorescence spectroscopy and microscopy of NAD(P)H and flavoprotein. Biophys. J. 82:2811-2825.
47. Gurrapu, S., S. K. Jonnalagadda, M. A. Alam, G. L. Nelson, M. G. Sneve, L. R. Drewes, and V. R. Mereddy. 2015. Monocarboxylate Transporter 1 Inhibitors as Potential Anticancer Agents. ACS Medicinal Chemistry Letters 6:558-561. Letter.
48. Ronayne, C. T., L. N. Solano, G. L. Nelson, E. A. Lueth, S. L. Hubbard, T. J. Schumacher, Z. S. Gardner, S. K. Jonnalagadda, S. Gurrapu, J. Holy, and V. R. Mereddy. 2017. Synthesis and biological evaluation of 2-alkoxycarbonylallyl esters as potential anticancer agents. Bioorganic & Medicinal Chemistry Letters 27:776–780.
49. Zielonka, J., J. Joseph, A. Sikora, M. Hardy, O. Ouari, J. Vasquez-Vivar, G. Cheng, M. Lopez, and B. Kalyanaraman. 2017. Mitochondria-Targeted Triphenylphosphonium-Based Compounds: Syntheses, Mechanisms of Action, and Therapeutic and Diagnostic Applications. ACS Chem. Rev. 117:10043−10120.
50. Heikal, A. A. 2010. A multiparametric imaging of cellular coenzymes for monitoring metabollic and mitochondrial activities. Reviews in Fluorescence:223-243. Review.
51. Ariola, F. S., D. J. Mudaliar, R. P. Walvick, and A. A. Heikal. 2006. Dynamics imaging of lipid phases and lipid-marker interactions in model biomembranes. Phys. Chem. Chem. Phys. 8:4517-4529.
52. Currie, M., H. Leopold, J. Schwarz, A. J. Boersma, E. D. Sheets, and A. A. Heikal. 2017. Fluorescence Dynamics of a FRET Probe Designed for Crowding Studies. The Journal of Physical Chemistry B 121:5688-5698.
53. Yu, Q., M. Proia, and A. A. Heikal. 2008. Integrated biophotonics approach for noninvasive and multiscale studies of biomolecular and cellular biophysics. J. Biomed. Optics 13:041315.
54. Lee, H. B., A. Cong, H. Leopold, M. Currie, A. J. Boersma, E. D. Sheets, and A. A. Heikal. 2018. Rotational and translational diffusion of size-dependent fluorescent probes in homogeneous and heterogeneous environments. Physical Chemistry Chemical Physics.
55. Cong, A., R. M. L. Pimenta, H. B. Lee, V. Mereddy, J. Holy, and A. A. Heikal. 2019. Two-photon fluorescence lifetime imaging of intrinsic NADH in three-dimensional tumor models. Cytometry Part A 95:80-92.
56. Liu, Y., F. S. Ariola, H.-R. Kim, Q. Yu, R. Walvick, and A. Heikal. 2006. Two-photon excited-state and conformation dynamics of NADH binding with dehydrogenases. Femtochemistry VII. A. W. Castleman and M. L. Kimble, editors. Elsevier, Amsterdam, pp. 396-401.
57. Wallrabe, H., Z. Svindrych, S. R. Alam, K. H. Siller, T. Wang, D. Kashatus, S. Hu, and A. Periasamy. 2018. Segmented cell analyses to measure redox states of autofluorescent NAD(P)H, FAD & Trp in cancer cells by FLIM. Scientific Reports 8:1-11.

58. Alhallak, K., L. G. Rebello, T. J. Muldoon, K. P. Quinn, and N. Rajaram. 2016. Optical redox ratio identifies metastatic potential-dependent changes in breast cancer cell metabolism. Biomed. Opt. Express 7:4364-4374. Research paper.
59. Mah, E. J., A. E. Y. T. Lefebvre, G. E. McGahey, A. F. Yee, and M. A. Digman. 2018. Collagen density modulates triple-negative breast cancer cell metabolism through adhesion-mediated contractility. Scientific Reports 8.
60. Cannon, T. M., A. T. Shah, and M. C. Skala. 2017. Autofluorescence imaging captures heterogeneous drug response differences between 2D and 3D breast cancer cultures. Biomed. Opt. Express 8:1911-1925.
61. Skala, M. C., K. M. Riching, A. Gendron-Fitzpatrick, J. Eickhoff, K. W. Eliceiri, J. G. White, and N. Ramanujam. 2007. In vivo multiphoton microscopy of NADH and FAD redox states, fluorescence lifetimes, and cellular morphology in precancerous epithelia. PNAS 104:19494-19499.
62. Fischer, R. S., K. A. Myers, M. L. Gardel, and C. M. Waterman. 2012. Stiffness-controlled three-dimensional extracellular matrices for high-resolution imaging of cell behavior. Nature protocols 7:10.1038/nprot.2012.1127.
63. Mah, E. J., G. E. McGahey, A. F. Yee, and M. A. Digman. 2018. Collagen stiffness modulates MDA-MB231 cell metabolism through adhesion-mediated contractility. bioRxiv.
64. Sousa, B., J. Pereira, and J. Paredes. 2019. The Crosstalk Between Cell Adhesion and Cancer Metabolism. 20(8):1933.

Appendix I: Statistical analysis using Origin

1. Transfer the data needed to Origin, make sure they are labeled appropriately

Comparing more than two groups of data using One-way ANOVA:

2. Highlight the columns of interest
3. Go to Statistics → ANOVA → Select "One-way ANOVA" to open dialogue
4. Change "Recalculate" to "Auto"
5. Change Input Data from "Indexed" to "Raw"
6. Hit OK, a new sheet should pop up next to the original data sheet, reporting the results

(Notes: This test is good for reporting statistical analysis (ie. the means and standard deviations) of many different groups of data at once and the overall difference among the groups, but it does not tell whether two specific groups within the selection are significantly different from each other. To do this, proceed to the next test.)

Comparing two groups of data using Two-Sample *t*-Test:

Before proceeding to the two-sample t-test, a two-sample test for variance should be carried out to determine the appropriate t-test to use.

7. Highlight the two columns containing the two groups of interest
8. Go to Statistics → Hypothesis Testing → Two-Sample Test for Variance to open dialogue
9. Again, change "Recalculate" to "Auto"
10. Change Input Data from "Indexed" to "Raw"
11. Hit OK to carry out the test and see the results reported
12. Two possible outcomes of this test:
    - The two populations variance is NOT significantly different
    - The two populations variance is significantly different

Having calculated this result, a Two-Sample t-Test can be carried out by repeating steps 7-11 with the exception:

13. Instead of choosing Two-Sample Test for Variance under Hypothesis Testing, select the Two-Sample *t*-Test and open the dialogue
14. This test calculates the p-values using two different *t*-tests, one assumes equal variance between the two populations and the other assumes NOT equal variance between the two populations
15. If the result from step 12 states that the two populations variance is NOT significantly different, use the *p*-value resulted from "Equal Variance Assumed", and vice versa
16. If the p-value (Prob>[t]) is <0.05, the two populations are significantly different from each other. If the p-value is >0.05, the two populations are NOT significantly different from each other. Report the appropriate conclusion and *p*-value.

Appendix II: Associated anisotropy simulations

Table A.1: List of values that were used to create simulation profiles for the associated anisotropy of a mixture of free and enzyme bound NADH, shown in the order as the resulting decay curve appears on Figure 4.1 (top to bottom).

(A) Varying α_1 and α_2

α_1	τ_1 (ns)	α_2	τ_2 (ns)	β_1	φ_1 (ns)	β_2	φ_2 (ns)
0.1	0.45	0.1	1.2	0.35	0.15	0.4	50
0.25	0.45	0.25	1.2	0.35	0.15	0.4	50
0.5	0.45	0.5	1.2	0.35	0.15	0.4	50
0.75	0.45	0.75	1.2	0.35	0.15	0.4	50
0.9	0.45	0.9	1.2	0.35	0.15	0.4	50

(B) Varying τ_1

α_1	τ_1 (ns)	α_2	τ_2 (ns)	β_1	φ_1 (ns)	β_2	φ_2 (ns)
0.5	0.3	0.5	1.2	0.35	0.15	0.4	50
0.5	0.45	0.5	1.2	0.35	0.15	0.4	50
0.5	0.6	0.5	1.2	0.35	0.15	0.4	50
0.5	0.8	0.5	1.2	0.35	0.15	0.4	50
0.5	1.0	0.5	1.2	0.35	0.15	0.4	50
0.5	1.2	0.5	1.2	0.35	0.15	0.4	50

(C) Varying τ_2

α_1	τ_1 (ns)	α_2	τ_2 (ns)	β_1	φ_1 (ns)	β_2	φ_2 (ns)
0.5	0.45	0.5	3.2	0.35	0.15	0.4	50
0.5	0.45	0.5	2.2	0.35	0.15	0.4	50
0.5	0.45	0.5	1.2	0.35	0.15	0.4	50
0.5	0.45	0.5	1.0	0.35	0.15	0.4	50
0.5	0.45	0.5	0.8	0.35	0.15	0.4	50
0.5	0.45	0.5	0.45	0.35	0.15	0.4	50

(D) Varying β_1

α_1	τ_1 (ns)	α_2	τ_2 (ns)	β_1	φ_1 (ns)	β_2	φ_2 (ns)
0.5	0.45	0.5	1.2	0.45	0.15	0.4	50
0.5	0.45	0.5	1.2	0.35	0.15	0.4	50
0.5	0.45	0.5	1.2	0.25	0.15	0.4	50
0.5	0.45	0.5	1.2	0.15	0.15	0.4	50
0.5	0.45	0.5	1.2	0.05	0.15	0.4	50

(E) Varying β_2

α_1	τ_1 (ns)	α_2	τ_2 (ns)	β_1	φ_1 (ns)	β_2	φ_2 (ns)
0.5	0.45	0.5	1.2	0.35	0.15	0.4	50
0.5	0.45	0.5	1.2	0.35	0.15	0.3	50
0.5	0.45	0.5	1.2	0.35	0.15	0.2	50
0.5	0.45	0.5	1.2	0.35	0.15	0.1	50
0.5	0.45	0.5	1.2	0.35	0.15	0.05	50

(F) Varying φ_1

α_1	τ_1 (ns)	α_2	τ_2 (ns)	β_1	φ_1 (ns)	β_2	φ_2 (ns)
0.5	0.45	0.5	1.2	0.35	0.4	0.4	50
0.5	0.45	0.5	1.2	0.35	0.3	0.4	50
0.5	0.45	0.5	1.2	0.35	0.2	0.4	50
0.5	0.45	0.5	1.2	0.35	0.15	0.4	50
0.5	0.45	0.5	1.2	0.35	0.1	0.4	50
0.5	0.45	0.5	1.2	0.35	0.05	0.4	50

(G) Varying φ_2

α_1	τ_1 (ns)	α_2	τ_2 (ns)	β_1	φ_1 (ns)	β_2	φ_2 (ns)
0.5	0.45	0.5	1.2	0.35	0.15	0.4	50
0.5	0.45	0.5	1.2	0.35	0.15	0.4	10
0.5	0.45	0.5	1.2	0.35	0.15	0.4	5
0.5	0.45	0.5	1.2	0.35	0.15	0.4	2.4
0.5	0.45	0.5	1.2	0.35	0.15	0.4	1.2
0.5	0.45	0.5	1.2	0.35	0.15	0.4	0.6
0.5	0.45	0.5	1.2	0.35	0.15	0.4	0.3
0.5	0.45	0.5	1.2	0.35	0.15	0.4	0.15

(H) Varying α_1, keeping $\tau_1 = \tau_2$

α_1	τ_1 (ns)	α_2	τ_2 (ns)	β_1	φ_1 (ns)	β_2	φ_2 (ns)
0.1	1.2	0.9	1.2	0.35	0.15	0.4	50
0.3	1.2	0.7	1.2	0.35	0.15	0.4	50
0.5	1.2	0.5	1.2	0.35	0.15	0.4	50
0.7	1.2	0.3	1.2	0.35	0.15	0.4	50
0.9	1.2	0.1	1.2	0.35	0.15	0.4	50